"Just watch me."
The Rt. Hon. Pierre Elliott Trudeau
Prime Minister of Canada (1968-79, 1980-84)

University of Alberta

Radial Transport of Electrons in the Radiation Belts Under the Effect of Ultra Low Frequency Waves

by

Scott W. O'Donnell

A thesis submitted to the Faculty of Graduate Studies and Research
in partial fulfillment of the requirements for the degree of

Master of Science

Department of Physics

Fall 2013
Edmonton, Alberta

To my maternal grandparents,
Mary and William O'Donnell.
Thank you for everything you have done for me.
I love you.

Abstract

For over 50 years, the study of Earth's radiation belts has been a major focus of the space physics community. Of great interest is the variability of energy in the belts, which is poorly understood and subject to intense investigation. We seek to explain how impulses from the Sun interact with Earth's geomagnetic field to generate ultra low frequency (ULF) waves that energize electrons in the outer belt.

Using the ideal magnetohydrodynamic assumption ULF wave model of [Degeling et al., 2011], we will examine how shear Alfvén waves are excited by ULF compressional waves generated from a current driver on the magnetopause boundary. By taking the model outputs, we trace electron motion in the equatorial magnetosphere and examine how they are transported radially in the radiation belts. This procedure allows us to calculate the first and second L moments to assess transport for electrons in the fields of ULF waves.

Acknowledgements

As sort of a prefatory note, I would like to mention that my acknowledgements might be a little longer than the norm you see in other theses. With that said, I also believe in giving credit where credit is due and that by not doing so, I am doing a disservice to the people who have helped me along the path. If I have forgotten someone, I apologize in advance - the omission was not intentional.

After almost three years in graduate studies, which included long nights of running and editing code, writing presentations, and grading the same thing over-and-over as part of being a teaching assistant (TA), there are people you must give credit to for helping to keep you on the path of mental sanity. When your M.Sc. is in physics, this task becomes ten-fold more difficult.

The first two people I must thank are the two individuals who encouraged me to follow the golden road of physics. I must give due credit to Jennifer Amos, my Physics 112 (grade 11 level) instructor, who served as my first real introduction to the beauty of physics. Her course was the beginning of my long and adventurous journey in physics and thus encouraged me to take Physics 122 (grade 12 level) under the direction of Fred Estabrooks, who was very supportive of me taking physics at the post-secondary level. I owe Ms. Amos and Mr. Estabrooks a debt of gratitude for helping me find my niche, otherwise, I'd probably be writing this thesis under the banner of the Department of Mathematics and Statistical Sciences.

The next pair of people I must thank also encouraged me in the scientific path. Peggy Kirkpatrick taught me mathematics in eleventh grade and helped to develop and hone my interest in the subject (which has proven to be quite beneficial). She has been a source of great encouragement and advice since I began as an undergraduate in September 2006 and I am grateful for someone like her in my life. The last legacy thank you goes to Ken McDowell, who taught me Biology 112 and 120. His passion for science and his dedication to teaching effused into the classroom, which has served as my inspiration for wanting to become an educator one day. Furthermore, during my first year of university, Mr. McDowell served as great counsel for advice and always told me not to "sweat the small stuff," which proved to be an excellent suggestion and made my freshman year less stressful. I owe Mrs. Kirkpatrick and Mr. McDowell for putting me on the

right path and providing superb words of wisdom to me as a freshman - it paid off!

Now that I finished thanking people from my high school era, I need to thank some people from the university era.

First, I would like to thank all the students who were under my guidance during my two years as a TA. I realize I was quite strict with marking and at times, I probably made your life miserable, but I did it with the noble goal in mind of helping you to become better students. I would also thank the students who let me know personally that my efforts were not in vain. As well, I would also thank students who offered constructive criticism during my tenure as a TA. These people include, but are not limited to: R. Arnason, A. Catuneanu, E. DeMilliano, M. Fisher, L. Heagy, J. Hutchinson, B. Jugdutt, S. Nowicki, D. Purschke, A. Rezai, T. Robertson, T. Robinson, G. Vankosky, and A. Verma.

Second, I would like to thank all the members (past and present) of the space physics group in the Department of Physics. These people include, but not limited to: Mauricio Blanco, Alex Degeling, Konstantin Kabin, Laura Mazzino, David Miles, Kyle Murphy, Abiyu Nedie, Louis Ozeke, Clare Rae, Jonathan Rae, and Dmytro Sydorenko. I thank everyone in the group for making me feel very welcome. It is definitely somewhat of a tight-knit group, so it is always nice to feel like you belong. Also, I must also give extra credit to David Miles for helping me properly format the LaTeXtemplate in order to construct this thesis.

Third, I would like to thank Drs. Ian Mann, Richard Marchand, and Ying Tsui for taking time out of their busy research schedules to serve as part of my thesis examination committee.

Fourth, I must thank my supervisor, Dr. Robert Rankin, for taking me on as a graduate student and showing a lot of patience towards me, because there were some days I know I was a pain. Robert has provided much guidance on this project and helped to ensure its success. I am also grateful to Robert for allowing me, as an M.Sc. student, to present my work in the form of a poster at the AGU Chapman Conference *Dynamics of the Earth's Radiation Belts and Inner Magnetosphere* in St. John's, Newfoundland and Labrador.

Fifth, our Graduate Program Assistant in the Department of Physics, Sarah Derr, deserves recognition for all her hard work and tireless effort for graduate students. With her around, graduates students in the Department of Physics can rest a little easier at night.

Sixth, I would like to thank the Associate Chair of Graduate Studies in the Department of Physics, Dr. Sharon Morsink. Sharon has been nothing short of amazing. Her display of compassion towards graduate students is second-to-none. I would also thank her for her wise counsel during my time as a graduate student.

Last, I thank one of the space physics research associates, Dr. Alexander (Alex)

Degeling. Alex has been the go-to-guy for most of my questions about the physics involved in the research, about MATLAB, and the dying question of why Australians hate Foster's beer. Alex has also been patient with me and I know I have asked him some questions multiple times, but he managed to answer everything in a calm and helpful manner - something graduate students really appreciate! While working on this thesis, Alex has allowed me to use (and also extend) various models that he developed as a member of the Facility for Data Assimilation and Modeling (which is funded through the Canadian Space Agency). For that, I am forever in Alex's debt. I would gladly call Alex a mentor and foremost, a friend.

Of course, the last group of people that need to be thanked are probably, in my opinion, the most important, as they provided the most fundamental support a graduate student needs: emotional support, generally through constant encouragement and friendship.

There are many friends and colleagues both in and outside of the Department of Physics that I would like to render acknowledgement to. In no particular order, these people are as follows: N.S. Paul, J.R. Burns, C.M. Martin, A.I. Boangiu, A.P. Legg, N.P. Knutson, D.J. Grombacher, S.R. Hanchurak, D. Saltel, L. Mather, C. Budd, S. Underhill, K.M. Yurkiw, C.D. Sykes, C.G. Nielsen, S. Welwood, S. Allard, J. McGathan, S.A. Miller, T.R. Wood, J. Losby, M.E. Baker, A. Bahramian, K.A. Marlow, S.A.M. Bukhari, S. ur Rehman, A. Stevens, D.A.N. Foster, R. Lockwood, C. Quark, K.E. Carroll, C.L. DeLorme, N.E. Roberts, B. Anderson, D.W. DeLorme, J. Morrissy, D. McBean, E.M. Bellinger, H.M. Dani, and others I may have accidentally omitted. As stated in the prefatory note, if you were not included, it was by no means intentional.

There are some members of my family that I would also like to acknowledge for their love and support, not only throughout my graduate career, but my entire student career (and some, since the day I was brought onto this Earth). I offer my deepest of gratitudes to Laura Martin, my half-sister, and her parents, Fernand and Angela Martin, my father and step-mother; Michelle Richard, a very close friend of the family, who has always been like an aunt; Charlene Fraser, my aunt who has always been like a big sister; Harold Brodmann, my step-father; Constance Pyne, my mother; and last but not least, my maternal grandparents, Mary and William O'Donnell. Words simply cannot express my sentiments on how appreciative and grateful I am for your everlasting support, but nonetheless, I thank you all from the bottom of my heart.

A special acknowledgement goes to Daniel A. N. Foster and Simon A. Miller, both of whom were constantly at me to finish this thesis. Thank you, gentlemen, for your continuous reminders.

Contents

List of Tables

List of Figures

Chapter 1

Introduction

1.1 Historical Background

On January 23, 1958, Explorer 1, the first satellite by the United States, was launched. The scientific instrumentation was built by a team of scientists under the direction of James Van Allen from the University of Iowa. Part of the scientific instrumentation aboard Explorer 1 was a Geiger-Müller counter, which would be used to measure the flux of particles in space in order to detect cosmic rays. During the initial voyage of Explorer 1, it was noted that the Geiger counter would record 30 counts per second, then suddenly drop to zero at higher altitudes. The scientific team thought this to be peculiar as it was odd for there to suddenly be no particles detected. The mystery would soon be resolved (Green & Kivelson [2004]).

Explorer 3 was launched March 26, 1958 as a follow-up to the Explorer 1 mission. The mystery of the zero count rate detected by the Geiger counter from Explorer 1 was solved. It turned out that at higher altitudes during the Explorer 1 mission, the counter was being saturated with particles and, as a consequence, recorded the count rate to be zero. Explorer 1 and Explorer 3 had provided the first evidence for the existence of Earth's radiation belts, which were eventually named the Van Allen belts, in honour of James Van Allen's contribution to their discovery.

1.2 Magnetospheric Physics

In order to study the physics of space in a near-Earth environment, we need to examine some properties of Earth's magnetosphere, the solar wind, and the interaction between the two. This information will provide a firm basis into the science behind radiation belt physics in order to develop a deeper understanding of wave-particle interactions in the near-Earth region.

1.2.1 Solar Wind

The solar wind is a highly conducting plasma (ionized gas) flowing outward from the Sun at a velocity of roughly 450 km/s on average. It is the extension of the Sun's atmosphere into space; the outer boundary is at the heliopause where the pressure of the solar wind is balanced by interstellar winds. The solar wind is primarily composed of electrons and protons with a roughly five percent admixture of Helium ions (Baumjohann & Treumann [1997]). It is driven outward from the Sun due to a large pressure difference between the solar corona and the atmosphere outside of the Sun. Due to this imbalance in pressure, the solar wind is ejected radially outwards from the Sun (Kivelson & Russell [1995]). Some properties of the solar wind are listed in Table 1.1.

Table 1.1: Properties of the solar wind (from [Kivelson & Russell, 1995]).

Proton density	6.6 cm^{-3}
Electron density	7.1 cm^{-3}
Helium ion density	0.25 cm^{-3}
Velocity	450 km/s
Dynamic pressure	2.2 nPa
Proton temperature	1.2×10^5 K
Electron temperature	1.4×10^5 K
Interplanetary magnetic field (IMF)	5 nT

Embedded in the solar wind is the interplanetary magnetic field (IMF), which has a strength of roughly 5 nT. The IMF is frozen into the plasma according to the Alfvén frozen flux theorem, which states that the flux of the magnetic field through any closed contour moving with a fluid (in this case, the solar wind) remains constant and that the fluid (solar wind) elements that lie on a magnetic field line at one time will remain on the same field line at other times (Griffiths [1998]).

1.2.2 Magnetospheric Composition

In order to have a better understanding of the Sun-Earth environment, we need to investigate its composition and structure, as shown in Figure 1.1.

1.2.2.1 Bow Shock

As the solar wind approaches Earth, it encounters its magnetic field. The solar wind cannot simply penetrate Earth's magnetic field and as a consequence of

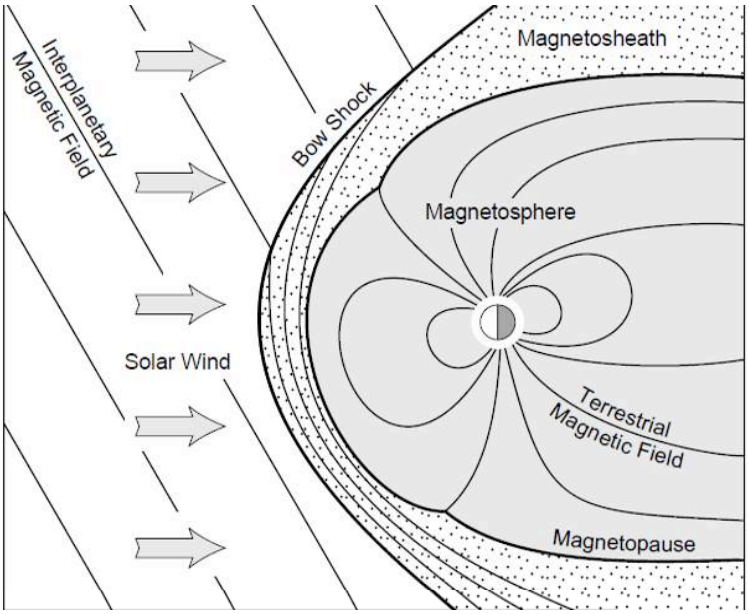

Figure 1.1: Solar wind interaction with Earth's magnetosphere (from [Baumjohann & Treumann, 1997]).

this, it is largely deflected around Earth. The point at which the solar wind slows down to a substantial fraction of its original velocity due the presence of Earth's magnetic field and converts much of the particles' kinetic energy into thermal energy is known as the bow shock. The bow shock serves to separate the interplanetary medium and the magnetosheath (Kivelson & Russell [1995]).

1.2.2.2 Magnetosheath

As the particles from the solar wind have their kinetic energy converted to thermal energy at the bow shock, this heats up the plasma behind the bow shock (the side closer to Earth) and it also gives rise to a subsonic plasma, as the solar wind velocity is slowed at the bow shock. This region of plasma behind the bow shock is known as the magnetosheath, which is the middle layer between the bow shock and the magnetosphere (Baumjohann & Treumann [1997]).

1.2.2.3 Magnetopause

The magnetopause is the boundary layer that separates the magnetosheath and the magnetosphere; it is a boundary between the solar wind and Earth's magnetic field, as well as the separation point between open and closed magnetic field lines. The location of the magnetopause is located where the dynamic pressure of the solar wind balances the pressure of Earth's magnetic field. Earth's magnetopause

is located roughly 10 R_E (Earth radius) from the center of Earth on the dayside in the equatorial plane (Baumjohann & Treumann [1997]).

1.2.2.4 Magnetosphere

The magnetosphere is the cavity that is formed by the interaction of the solar wind (and hence, the IMF) with Earth's magnetic field. On the dayside, when the solar wind interacts with the magnetic field, it becomes compressed due to the action of the solar wind flow. On the nightside, the magnetic field lines become stretched due to the IMF. When the southward IMF interacts with the northward magnetic field of Earth on the dayside, they merge creating an open field line with two footpoints fixed to Earth. These two open field lines stretch past Earth into the nightside and reconnect roughly 100 to 200 R_E away (Baumjohann & Treumann [1997]). Plasma circulates within the magnetosphere (as shown in Figure 1.2) in this configuration and energy is loaded into it. Eventually, this energy is dissipated through a process known as a substorm, which has associated with it a large deposition of energy into the ionosphere. A manifestation of this is the northern lights (in Canada), which show evidence of energetic charged particle interactions with the atmosphere. In a different configuration, when the IMF is northward, the magnetosphere is closed off from the solar wind in a teardrop shape. It is generally the case that the magnetospheric cavity is in a lower energy state in this situation.

1.2.3 Ring Current

The ring current around Earth is carried by particles that are trapped within Earth's magnetic field. Under the presence of gradient and curvature drifts (which will be introduced in Section 2.1 of this thesis), ions will traverse Earth in a clockwise manner (from the perspective of looking down on the North Pole) and electrons will travel in a counterclockwise direction. As the strength of the magnetic field increases as one gets closer to Earth (as B varies like r^{-3}), only high energy particles will be able to penetrate close to Earth. For this reason, the majority of particles that make up the ring current are high energy ions; hence, there is a new flow of particles that travel in a clockwise direction, which is what we define as the ring current (Kivelson & Russell [1995]).

1.2.4 Geomagnetic Storms

The first question that needs to be asked is, "What is a geomagnetic storm?" A geomagnetic storm is initiated in near-Earth space by a temporary disturbance of Earth's magnetosphere, which is measured by the change of the disturbance storm time (Dst) index. During times of heightened geomagnetic activity, there

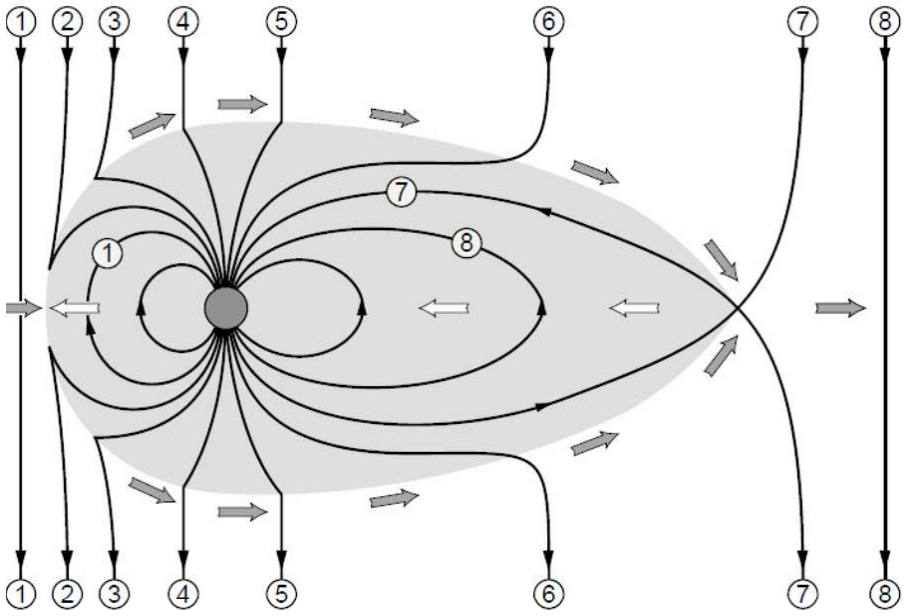

Figure 1.2: Illustration of the Dungey cycle, showing the process of field line merging and reconnection (from [Baumjohann & Treumann, 1997]).

is an increase in the re-connection rate of magnetic field lines both at the magnetopause and at the tail. As the plasma entrapped by the closed field lines moves towards Earth (explained further in Section 1.2.5), this increases the rate of convection, which in turn, increases the strength of the dawn-dusk electric field. As the particles contained in the plasma move closer to Earth, they form the ring current (as explained in the previous section), which causes a depression in Earth's magnetic field strength. This depression in the magnetic field strength is what is known as the Dst.

In the study of geomagnetic storms, we can examine two types: a coronal mass ejection (CME) driven storm and a corotating interaction region (CIR) driven storm. As the name implies, it is the storm driver that changes the characteristics of the storm (and 21 important differences between CME- and CIR-driven storms have been published by [Borovsky & Denton, 2006]). We want to briefly consider some of the characteristics of each storm.

1.2.4.1 Coronal Mass Ejection (CME) and Corotation Interaction Region (CIR) Driven Storms

The first question we ask is, "What is a CME?" A CME is a burst of solar wind plasma that emerges from the solar corona (Denton et al. [2006]). A CME

plasma consists mainly of ions and electrons. As the CME passes through the interplanetary medium, it will eventually interact with Earth's magnetosphere. As previously mentioned, when the solar wind reaches the dayside of the magnetosphere, the southward-directed IMF will open up Earth's field lines, which will then be reconnected on the nightside. As the field lines begin to relax after reconnection, the plasma trapped by the closed field line will be brought back towards Earth. Contained in this plasma is a large number of particles that contribute to the ring current, which aids in the depression of Earth's magnetic field (Kivelson & Russell [1995]).

The second question we ask is, "What is a corotation interaction region?" The answer is that it is a large-scale structure in the heliosphere, which we tend to find having a higher occurence during the declining phase of the solar cycle of the Sun. CIRs are a response to the interaction between fast and slow solar wind speeds and given their relation to fast solar wind speeds arising from the coronal holes, they tend to have a periodicity of roughly 27 days, which is the rotation period of the Sun (Denton et al. [2006]).

Table 1.2: Differences between CME- and CIR- driven storms (from Borovsky & Denton [2006] - this is not their complete table).

Phenomenon	CME-driven	CIR-driven
Solar energetic particles	sometimes	none
Sudden storm commencement	common	infrequent
Spacecraft surface charging	less severe	more severe
Ring current (Dst)	stronger	weaker
ULF pulsations	shorter duration	longer duration
Dipole distortion	very strong	strong
Fluxes of relativistic electrons	less severe	more severe
Formation of new radiation belts	sometimes	no

As seen in Table 1.2, which is taken from [Borovsky & Denton, 2006] (although this is not their complete table - for the full table, see their paper), we can compare phenomena between CME- and CIR-driven storms.

CME-driven storms tend to be associated with the sudden storm commencement phase of a storm, a stronger ring current (Dst), very strong distortion of the dipole magnetic field of Earth, and the potential to form a new (temporary) radiation belt in the magnetosphere. CIR-driven storms tend to be associated with severe charging of spacecraft around geosynchronous orbit, ULF pulsations of longer duration compared to CME-driven storms, and more severe fluxes of relativistic electrons in the outer radiation belts (Borovsky & Denton [2006]).

The analysis of geomagnetic storms provides an important insight into radiation belt physics. During a storm event, the radiation belts (especially the outer belt) become heavily populated with particles. This increase in particles contributes

to the ring current that occurs within the belts. By Ampère's law, the magnetic field it produces is directed southwards (as the current runs clockwise) and hence, opposite to Earth's magnetic field. The magnetic field due to the ring current serves to weaken the magnetic field of Earth, which is measured by the Dst index. Over the course of several days after the depression in Earth's magnetic field, particles will begin to be transported from the outer radiation belt, reducing the strength of the ring current and its magnetic field, returning the magnetic field of Earth to roughly pre-storm levels (Baumjohann & Treumann [1997]). Due to the variation of the magnetic field during the geomagnetic storm, after it has passed, we can have the case where the number of particles after the storm is much greater than pre-storm levels (enhancement) or much lower than pre-storm levels (drop-out).

Using the Bastille Day event from July 2000, we seek to explore the three main phases of a geomagnetic storm: sudden storm commencement, main phase, and recovery phase. Figure 1.3 shows the Dst index from the period of July 14 - 20, 2000, which we will use to describe the main phases of a geomagnetic storm in the next three subsections.

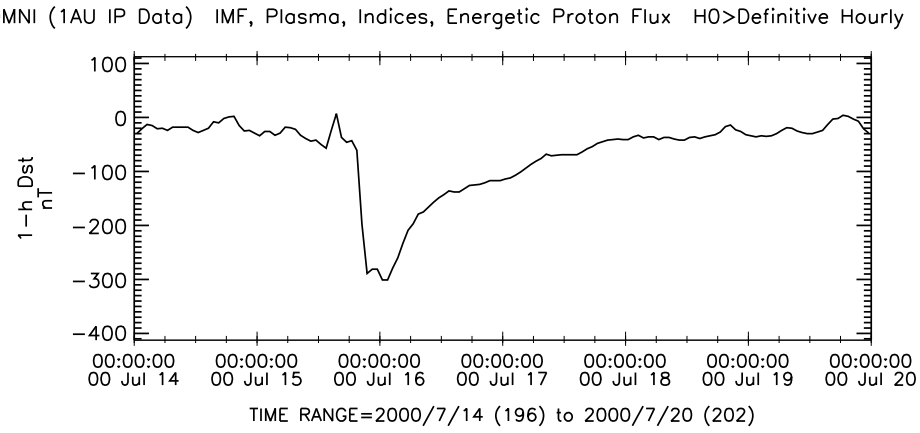

Figure 1.3: Dst index for the Bastille Day 2000 storm, July 14 - 20 (credit: J.H. King and N. Papitashvilli at ADNET, NASA GSFC, and CDAWeb).

1.2.4.2 Sudden Storm Commencement

The sudden storm commencement (SSC) is the first phase of a geomagnetic storm. During a period of increased solar wind dynamic pressure, the magnetosphere becomes compressed, which moves the magnetopause closer to Earth, which in

turn, causes an intensification of the magnetopause current. This increase in intensity of the current increases the strength of Earth's magnetic field on the order of tens of nanotesla (Elkington et al. [2003]). From Figure 1.3, this can be seen to occur between 1200 and 1800 on July 15.

1.2.4.3 Main Phase

The main phase of a geomagnetic storm begins when the Dst sees a rapid decrease due to the magnetic field induced by the ring current depressing the strength of Earth's magnetic field. Particles are primarily injected from the tail of the magnetosphere into the ring current by an increased dawn-dusk electric field. As more particles are brought into the ring current, the strength of its magnetic field increases, giving rise to and causing a negative Dst value, which signifies a larger depression in Earth's magnetic field (Kivelson & Russell [1995]). From Figure 1.3, the main phase begins roughly after 1800 on July 15 and ends after midnight on July 16. During a typical storm, the main phase generally lasts less than one day, usually between two to eight hours (Baumjohann & Treumann [1997]).

1.2.4.4 Recovery Phase

The recovery phase is characterized by the loss of particles in the radiation belt, which decreases the intensity of the ring current and its magnetic field and allows Earth's magnetic field to return to its pre-storm state. The particles undergo a loss process in the radiation belts, either by radial diffusion (the main topic of this thesis) or pitch-angle scattering. This process runs over the course of several days, as can be seen in Figure 1.3 - the recovery phase begins after midnight on July 16 and reaches pre-storm Dst in the afternoon of July 19, a period of just over three days. Typically, the recovery phases last between one to five days (Baumjohann & Treumann [1997]).

1.2.5 Convection and Corotation Electric Fields

1.2.5.1 Convection Electric Field

The convection electric field,

$$\mathbf{E} = -\mathbf{v} \times \mathbf{B} \tag{1.1}$$

can be obtained from the ideal magnetohydrodynamic (MHD) assumption (details in Section 2.1.2). During magnetic reconnection on the nightside, when the field lines relax and move towards Earth, the plasma enclosed by the field lines also travels Earthward. As this plasma moves through the northward magnetic

field of Earth, an electric field is generated that travels from the dawn side to the dusk side of Earth. This is the convection electric field, also referred to as the dawn-dusk electric field (Baumjohann & Treumann [1997]).

1.2.5.2 Corotation Electric Field

For completeness, we must also briefly examine the corotation electric field, which arises from Earth's rotation. The ionospheric plasma is only partially ionized and hence, the majority of collisions that occur are neutral-ion collisions and neutral-electron collisions. These collisions will force the plasma into corotation and by consequence, the field lines that are embedded within the plasma. The electric field generated by the rotation of the field lines is the corotation electric field and it is directed towards Earth. The corotation electric field dominates particle drift close to Earth, whereas further away, the convection electric field will dominate (Baumjohann & Treumann [1997]).

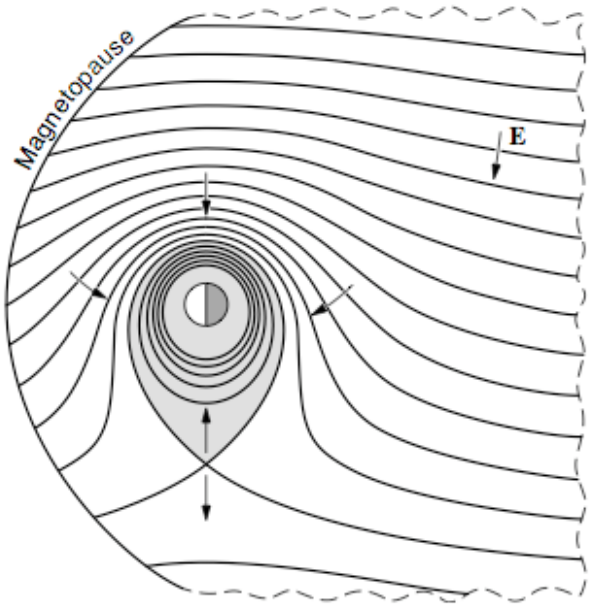

Figure 1.4: Equipotential contours in the magnetosphere (from [Baumjohann & Treumann, 1997]).

In the region where the corotation field dominates in comparison to the convection electric field, there are closed equipotential contours, which act as flow streamlines for the plasma. The flow in this region is closed in a loop, with the trapped plasma giving rise to the plasmapause (the shaded region of Figure 1.4). There is a bulge in the plasmapause that occurs at the point where the velocity from the corotation field and the velocity from the convection field balance; this is known as the stagnation point (or separatrix). It occurs at the point where the last closed equipotential contour crosses itself. The convection electric field helps to open up the closed flow contours, such that particles trapped in the plasmasphere become lost to the magnetopause, which produces a sharp decrease in particle density, known as the plasmapause (Baumjohann & Treumann [1997]).

1.2.6 Radiation Belts

The radiation belts (also known as the Van Allen belts) are toroid-shaped regions around Earth that consist of energetic ions and electrons that are trapped due to the magnetic field of Earth. Figure 1.5 shows the integral electron flux measured by the CRRES satellite from July 1990 to October 1991 (from [Hudson et al., 2008]), which demonstrates that the radiation belts are highly variable in terms of energy. Why that is the case is poorly understood and is currently a question of great importance in the space physics community.

High energy electrons produce radiation that is both harmful to space equipment (e.g. satellites, spacecraft) and astronauts. Having the ability to map electron flux in the radiation belts provides an idea of where to avoid sending equipment and/or personnel so as to avoid a loss of investment and life.

There are three regions to the Van Allen belts: inner belt, outer belt, and slot region, as can be seen in Figure 1.6, which also shows the Van Allen Probes (formerly known as the Radiation Belt Storm Probes). The Van Allen Probes are two satellites designed by the National Aeronautics and Space Administration (NASA) that are providing measurements to researchers needed to characterize and quantify the plasma processes that produce energetic ions and relativistic electrons. The overall purpose of the mission is to help us understand the influence of the Sun on the Earth and near-Earth environment.

1.2.6.1 Inner Region

The inner region of the Van Allen belts tends to extend from just over one to about three Earth radii. As the magnetic field of Earth is proportional to the inverse cube of the distance from the center of Earth, the magnetic field in this region is much stronger than further out in the region of the outer belt and thus, only high energy particles will be able to access this region (through conservation of the first adiabatic invariant, M - more on this in Section 2.2.1). In this region,

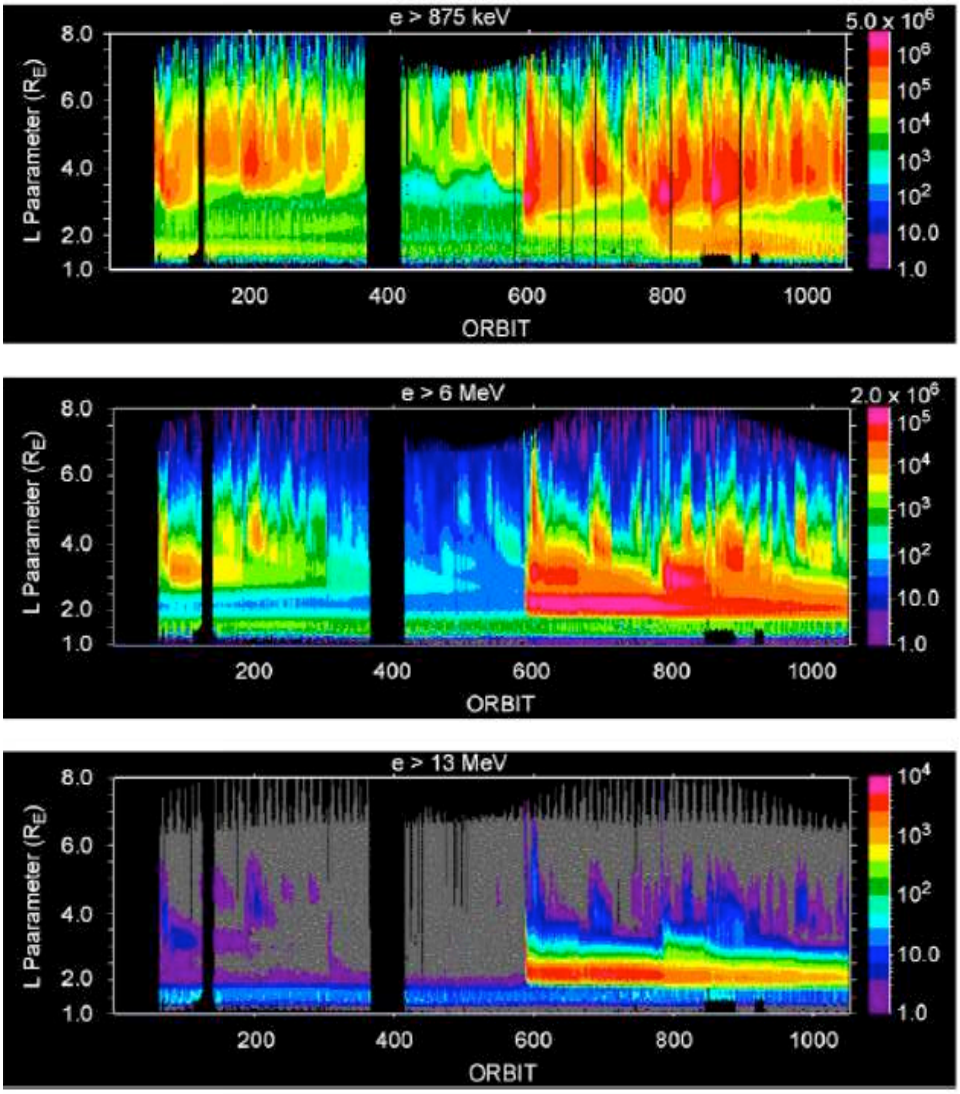

Figure 1.5: Figure of the integral electron flux from July 1990 to October 1991 as measured by CRRES (from [Hudson et al., 2008]). This figure demonstrates that the energy levels of the outer radiation belt are highly variable.

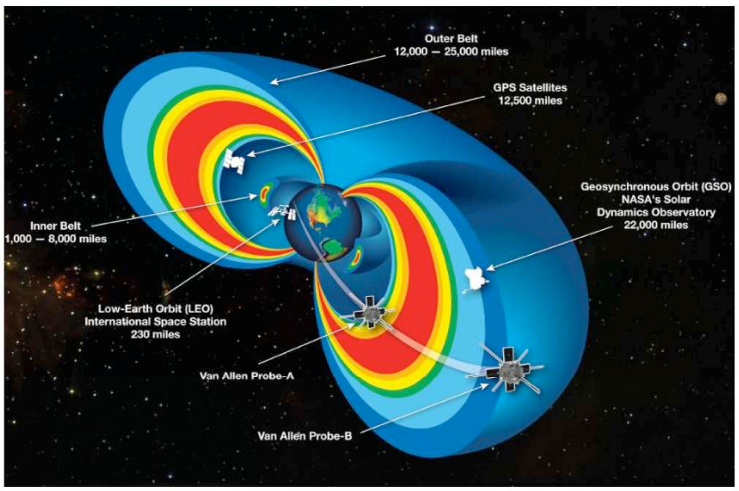

Figure 1.6: The radiation (Van Allen) belts (courtesy of NASA), showing the distinct regions (inner and outer belts, slot region). Also shown is a satellite in geosynchronous orbit and two Van Allen Probes orbiting through the radiation belts.

electrons with energies in the range of 100 keV and protons with energies in the range of hundreds of MeV can be found. The inner radiation belt population is primarily a result from decay of neutrons freed by cosmic rays impinging on the upper atmosphere.

1.2.6.2 Outer Region

The outer region of the Van Allen belts extends from about three to appoximately seven Earth radii. This region is home primarily to electrons with energies that range from 0.1 to 10 MeV. As the magnetic field is much weaker in this region, particles with much lower energy than those in the inner radiation belt will typically be found here (again, through conservation of M). The principle acceleration mechanisms in this region are radial diffusion from an external source and internal source acceleration.

1.2.6.3 Slot Region

The slot region is located between the inner and outer radiation belt regions. It is kept nearly free of particles mainly due to the resonant interactions with whistler mode waves excited by electrons in the tens to hundreds of keV energy

range that diffuse electrons by pitch angle scattering into the loss cone (Lyons et al. [1972]).

1.2.7 Ultra Low Frequency (ULF) Waves

One of the central focus points of this thesis is ULF waves in the magnetosphere. More specifically, we are interested in ULF waves in the Pc5 range, which exhibit a period between 150 to 600 seconds (in terms of frequency, on the order of a few millihertz) (Jacobs et al. [1964]).

One of the first questions to ask is, "Where do ULF waves come from?" As the solar wind comes to the magnetopause, one of two things may happen: 1. the varying dynamic pressure of the solar wind will cause the boundary to oscillate (buffeting); 2. the solar wind will travel along the flanks of the boundary. Both of these situations will generate ULF waves in the magnetosphere, so we must examine both situations.

The first method of generating waves is the motion of the magnetopause boundary. As the dynamic pressure of the solar wind is proportional to the square of the solar wind velocity, it is subject to change with time as the solar wind speed changes. The response of the magnetopause to the change in pressure is to oscillate (Baumjohann & Treumann [1997]). These oscillations of the boundary cause compressions and rarefactions in the local magnetic field, which propagate as compressional waves (MHD fast waves) across Earth's magnetic field.

The second method of generating waves is known as the Kelvin-Helmholtz (K-H) instability. The K-H instability arises from the velocity difference at the magnetopause; on one side of the boundary, the solar wind is travelling at supersonic speeds, whereas on the other side, there is a stationary plasma. This shear flow of the solar wind along the interface generates waves along the flanks of the magnetopause. A simple analogy of the K-H instability is the wind over water example. As the wind, acting as a fast flow, blows over the water, acting as a slower flow, waves begin to form along the interface; these waves continue to grow as time elapses. This is the same scenario that happens along the flanks, with the solar wind being analagous to the wind and the plasma being analgous to the water.

The study of ULF waves has been an interesting scientific pursuit for almost a half-century. Ground-based magnetometer measurements from seven radar stations in Western Canada in the summer of 1969 produced strong evidence that the Kelvin-Helmholtz instability served as an energy source for micropulsations (rapid variations in Earth's magnetic field) (Samson et al. [1971]). A study done by [Rostoker et al., 1998] visually indicated a strong correlation between energetic electron flux and ULF wave activity. This is done by making a comparison between the wave activity in the magnetosphere and comparing with electron flux greater than 2 MeV from the GOES-7 spacecraft (Elkington [2006])

The work of [Rostoker et al., 1998] was expanded upon by [O'Brien et al., 2001] and [Mathie & Mann, 2000]. A more recent study done by [Mann et al., 2004] examined the correlation between solar wind speed, ULF wave power, and MeV electron fluxes during a complete solar cycle (from 1990 to 2001). They found that the strongest correlation of the solar wind speed and ULF wave power with the electron flux was during the declining phase of the solar cycle; during this period, this was when electron fluxes were at their highest point.

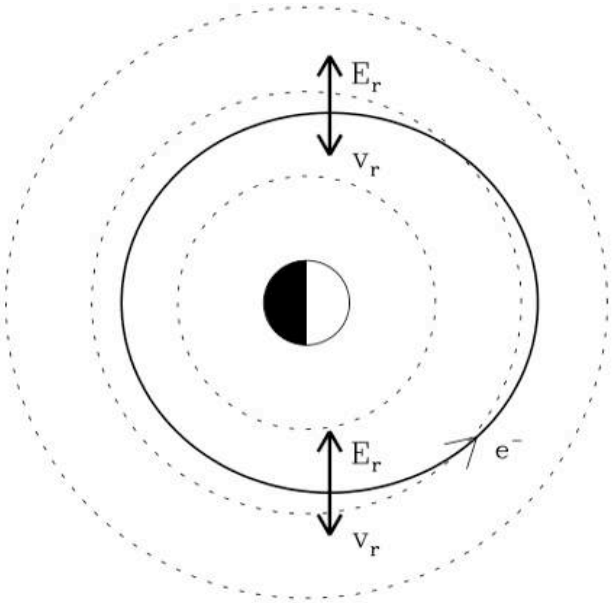

Figure 1.7: Sketch of the drift path of an electron for a toroidal oscillation in an $m_N = 2$ mode (from [Elkington et al., 2003]). The field E_r is due to the toroidal wave whereas v_r indicates the velocity of a particle in response to E_r.

Figure 1.7 demonstrates a potential mechanism for how electrons in the radiation belts can be energized by ULF waves; it is known as drift-resonance. An electron in the equatorial plane interacts with a $m_N = 2$ (i.e. two full wavelengths azimuthally around Earth in the equatorial plane) toroidal wave with frequency ω. An electron that starts at dusk, moving with drift frequency $\omega_d = \omega$, would first see a positive radial electric field while undergoing negative radial motion and half a drift period later, a negative electric field while moving radially outward. Looking at the product of $E_r dr$, it will have an overall negative sign as the electron completes a full drift path (Elkington et al. [1999]). This leads to an overall net energization of the particle, through interaction with the radial electric field (Elkington [2006]).

1.3 Thesis Outline

The main goal of this thesis is to examine the transport and energization of electrons from ULF waves in the outer radiation belt through wave-particle interactions.

Chapter 2 seeks to examine the general methodology of the project. In this chapter, we focus on the equation of motion for particles and using the guiding center approximation from [Northrup, 1963] and [Roederer, 1970], we obtain the guiding center equations for the particle trajectories. We will also discuss the three adiabatic invariants of plasma physics and their relation to particle motion as well as the various types of drift motion particles may encounter in the magnetosphere. Finally, we will discuss radial transport of particles in the outer belt.

Chapter 3 seeks to give a brief overview of the theory behind a pulse traveling in the solar wind that will come into contact with the magnetopause and generate ULF waves that will travel throughout the magnetosphere. This is also our first chance to talk about magnetohydrodynamic waves and to classify them according to factors such as their direction of propagation and velocity.

Chapter 4 will examine the ULF wave model that is being used. We will be investigating how the generation of ULF waves from a driver on the magnetopause boundary excites the Alfvén continuum in the magnetosphere, considering the cases of low, moderate, and high solar wind speeds.

Chapter 5 will serve to look at the particle aspect of the thesis by taking the outputs (electric and magnetic fields) of the wave model from Chapter 4 and using them to drive particles. From this, we can look at whether the particles are undergoing diffusive transport or convective transport.

Finally, Chapter 6 will serve to give concluding marks and a discussion of future work.

Chapter 2

Methodology

In order to study the effects of electron transport and energization in the outer radiation belt, under the influence of ULF waves, it is important to have a firm understanding of just how particles (specifically, electrons) respond to electric and magnetic fields that are present in space. In this chapter, we will examine the different types of drift motion under the influence of fields, as well as adiabatic invariants, which themselves describe a particular type of particle motion. Finally, we discuss radial transport in the outer radiation belt.

2.1 Particle Motion

2.1.1 Equation of Motion

When discussing motion of any sort, there needs to be an equation that governs said motion. In elementary physics, assuming a constant mass, one of the first equations we learn is,

$$\frac{d\mathbf{p}}{dt} = m\mathbf{a} \tag{2.1}$$

where $\mathbf{p}$ is the momentum of the body in question, m is its mass, and $\mathbf{a}$ is its acceleration. For particles under the influence of electric and/or magnetic fields, we seek to cast Equation 2.1 in a more useful form.

In electrostatics, we only focus on the case where there is no magnetic field present, as in order to have a magnetic field, a current is required, which requires non-stationary charges. In such a case, the particle motion can be described by,

$$\frac{d\mathbf{p}}{dt} = q\mathbf{E} \tag{2.2}$$

where $\mathbf{p}$ is the momentum of the particle, q is the charge of the particle, and $\mathbf{E}$ is the electric field that is guiding the motion of the particle (Griffiths [1998]).

Equation 2.2 can be used to derive the rate of energy gain of a charged particle. Taking the dot product with the velocity of the particle drift, we obtain,

$$\frac{dW}{dt} = q\mathbf{E} \cdot \mathbf{v_d} \tag{2.3}$$

where $\mathbf{v_d}$ is the drift velocity and W is the work. It is obvious that particles gain or lose energy, provided $\mathbf{E}$ and $\mathbf{v_d}$ are not perpendicular.

Now what about the case where we have a magnetic field present, but no electric field? There is also an equation of motion that covers us in this situation, given by,

$$\frac{d\mathbf{p}}{dt} = q\mathbf{v} \times \mathbf{B} \tag{2.4}$$

where $\mathbf{v}$ is the velocity of the particle and $\mathbf{B}$ is the magnetic field strength that is influencing the motion of the particle (Griffiths [1998]). By virtue of the cross product in Equation 2.4, the motion of the particle will be perpendicular to both its velocity and the magnetic field strength.

The next step of complexity would be to describe the equation of motion for particles that are under the influence of both electric and magnetic fields. By adding the right sides of Equations 2.2 and 2.4 together, we get,

$$\frac{d\mathbf{p}}{dt} = q\left(\mathbf{E} + \mathbf{v} \times \mathbf{B}\right) \tag{2.5}$$

which is the equation that governs the motion for particles under the influence of both electric and magnetic fields. Equation 2.5 serves as the starting point to derive different types of particle motion.

2.1.2 Particle Drifts

2.1.2.1 E × B Drift

The first drift to look at is $\mathbf{E} \times \mathbf{B}$ drift. In order to derive this, we look at a particle's current density, given by,

$$\mathbf{J} = \sigma\left(\mathbf{E} + \mathbf{v} \times \mathbf{B}\right) \tag{2.6}$$

where $\mathbf{J}$ is the current density and σ is the conductivity (Griffiths [1998]). In the study of plasma physics, the assumption is that a plasma is considered to be a very good conductor, so the conductivity is set to infinity (Baumjohann &

Treumann [1997]). If we divide both sides by σ, the left hand side of Equation 2.6 goes to zero, hence,

$$\mathbf{E} + \mathbf{v} \times \mathbf{B} = 0 \tag{2.7}$$

If we move the cross product to the right hand side, cross both sides with $\mathbf{B}$ and isolate for $\mathbf{v}$, we get,

$$\mathbf{v}_{\mathbf{E}\times\mathbf{B}} = \frac{\mathbf{E} \times \mathbf{B}}{B^2} \tag{2.8}$$

which is the equation for the velocity of a particle undergoing $\mathbf{E} \times \mathbf{B}$ drift. From Equation 2.8, it can be seen that the particle's velocity is perpendicular to both the electric and magnetic fields (as seen in Figure 2.1). As well, since Equation 2.8 is independent of the particle's charge, ions and electrons will drift in the same direction.

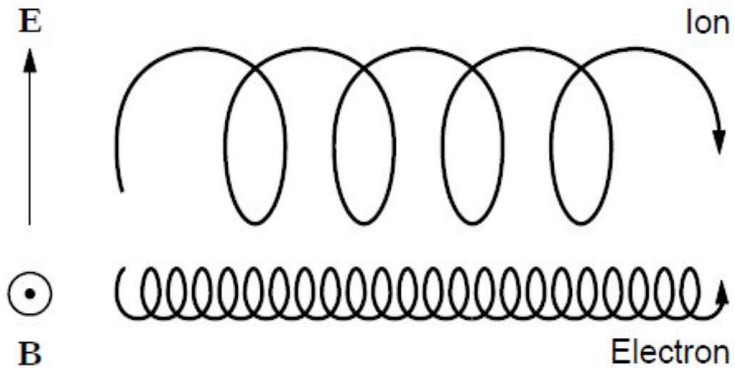

Figure 2.1: Schematic depiction of $\mathbf{E} \times \mathbf{B}$ drift (from [Baumjohann & Treumann, 1997]).

2.1.2.2 Polarization Drift

The next motion we wish to examine is polarization drift. Crossing Equation 2.5 with $\mathbf{B}/B^2$ gives us,

$$\mathbf{v} - \frac{\mathbf{B}\,(\mathbf{v} \cdot \mathbf{B})}{B^2} = \frac{\mathbf{E} \times \mathbf{B}}{B^2} - \frac{m}{q}\frac{d\mathbf{v}}{dt} \times \frac{\mathbf{B}}{B^2} \tag{2.9}$$

The left-hand side of Equation 2.9 is the perpendicular velocity vector and the first term on the right-hand side is the term for $\mathbf{E} \times \mathbf{B}$ drift (cf. Equation 2.8). If we average Equation 2.9 over the period of gyromotion, this allows us to take the left-hand side of Equation 2.9 as the perpendicular drift velocity of the particle (Baumjohann & Treumann [1997]), $\mathbf{v_d}$, which permits us to write,

$$\mathbf{v_d} = \mathbf{v_{E \times B}} - \frac{m}{qB^2} \frac{d}{dt} (\mathbf{v} \times \mathbf{B}) \tag{2.10}$$

Using Equation 2.7 in Equation 2.10 allows us to write the drift velocity as,

$$\mathbf{v_d} = \mathbf{v_{E \times B}} + \frac{m}{qB^2} \frac{d\mathbf{E}_\perp}{dt} \tag{2.11}$$

The second term on the right-hand side of Equation 2.11 is known as polarization drift,

$$\mathbf{v_P} = \frac{m}{qB^2} \frac{d\mathbf{E}_\perp}{dt} \tag{2.12}$$

Equation 2.12 is a consequence of the system having a time-varying electric field. Polarization drift is directed along the electric field. Unlike $\mathbf{E} \times \mathbf{B}$ drift, polarization drift is charge-dependent.

2.1.2.3 Gradient Drift

We must now look at the case when we do not have a homogeneous magnetic field. In space, there will be a gradient in the magnetic field. The magnetic field becomes stronger in the region of the increasing gradient. As particles will travel through regions of changing magnetic field, we must examine their motion in response to the change of the field.

When examining the gradient drift, we want to observe the case where the pitch angle, α, is 90 degrees (the pitch angle is the angle between the velocity vector of the particle and the magnetic field line) and thus, when the magnetic field gradient is perpendicular to the magnetic field line.

In order to determine the gradient drift, we need to investigate the net force encountered by the particle as it travels in an inhomogeneous magnetic field. This is given by (Roederer [1970]),

$$f_z = q v_\perp (B + \rho_c \cos\phi \nabla B) \cos\phi \tag{2.13}$$

where $v_\perp$ is the perpendicular component of the particle's velocity, ρ_c is the gyroradius of the particle's orbit, and ∇B is the gradient of the magnetic field.

As the magnetic field is changing over the course of a single orbit, we are required to take an average (cyclotron average) of Equation 2.13,

$$\bar{f} = \frac{1}{2\pi}\int_0^{2\pi} f_z d\phi = \frac{1}{2} q v_\perp \rho_c \nabla B \tag{2.14}$$

If we define the gyroradius as (Baumjohann & Treumann [1997]),

$$\rho_c = \frac{m v_\perp^2}{qB} \tag{2.15}$$

and cross Equation 2.14 with $\hat{\mathbf{B}}$, the unit vector in the direction of the magnetic field, and divide by qB, this gives us,

$$\mathbf{v}_\nabla = \frac{m v_\perp^2}{2qB^3}(\mathbf{B} \times \nabla B) \tag{2.16}$$

This is the gradient drift of a particle. For Equation 2.16 to be valid, we require that the magnetic field strength change very little along a cyclotron orbit (Roederer [1970]),

$$\rho_c \frac{\nabla B}{B} \ll 1 \tag{2.17}$$

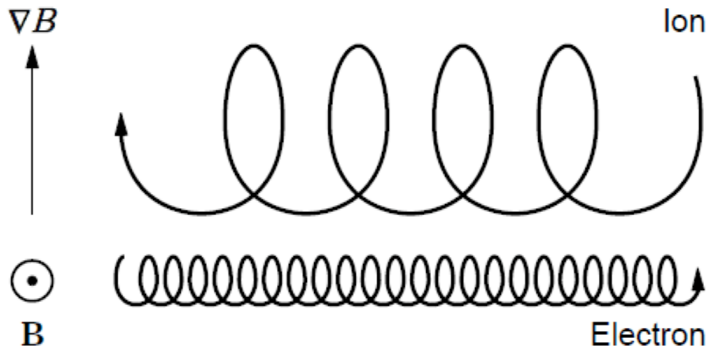

Figure 2.2: Schematic depiction of gradient drift (from [Baumjohann & Treumann, 1997]).

As can be seen from Equation 2.16 and Figure 2.2, the particles travel in a direction that is perpendicular to both the direction of the magnetic field and

its gradient. Since the motion is in the direction perpendicular to $\mathbf{B}$ and $\nabla_{\perp} B$, the particle will drift along a contour of constant magnetic field in the plane perpendicular to the magnetic field (Roederer [1970]). Furthermore, as Equation 2.16 is charge dependent, ions and electrons will drift in opposite directions, as can be seen in Figure 2.2.

2.1.2.4 Curvature Drift

For completeness of examining drift motion, we want to examine the effect on the motion of a particle due to the natural curvature of magnetic field lines. In order to do this, we impose the condition that the radius of curvature of the field line is much greater than the gyroradius of the particle ($R_c \gg \rho_c$) and that $\alpha > 0$.

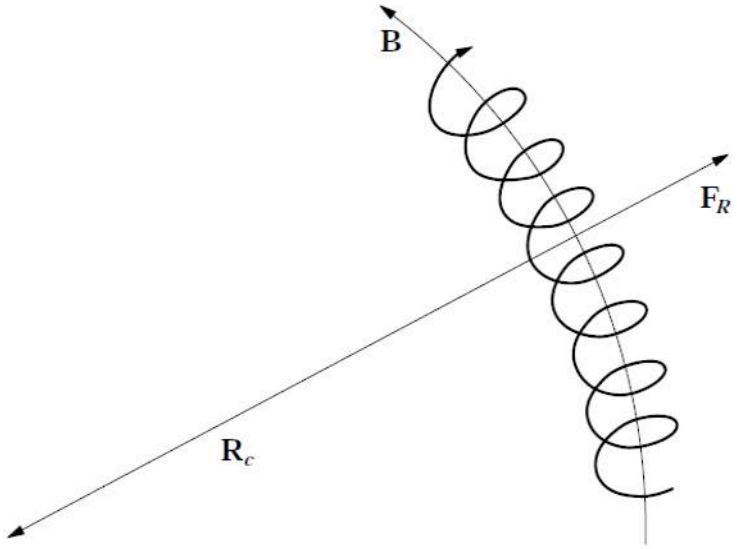

Figure 2.3: Schematic depiction of curvature drift (from [Baumjohann & Treumann, 1997]).

Any mass on a curved trajectory will experience a centrifugal force, governed by,

$$\mathbf{F_c} = \frac{m v_{\parallel}^2}{R_c} \hat{\mathbf{R}}_\mathbf{c} \tag{2.18}$$

where $v_{\parallel}$ is the parallel component of velocity (along the magnetic field line) and $\hat{\mathbf{R}}_\mathbf{c}$ is the unit vector in the direction of the radius of curvature (see Figure 2.3). Like we did with the gradient drift, if we cross $\hat{\mathbf{B}}$ and divide by qB with Equation 2.18, we get,

$$\mathbf{v_c} = \frac{mv_{\parallel}^2}{qR_c^2B^2}\left(\mathbf{R_c} \times \mathbf{B}\right) \tag{2.19}$$

which is the curvature drift for a particle (Roederer [1970]).

2.1.2.5 Gradient-Curvature Drift

Now that we have developed the formulae for the gradient and curvature drifts separately, it is time to combine them, as both of the drifts work together for the total magnetic drift, or gradient-curvature drift. The pitch angle of the particle will determine which drift has a stronger influence. By using the relationship (Baumjohann & Treumann [1997], Roederer [1970]),

$$\nabla B = -\frac{B}{R_c^2}\hat{\mathbf{R}}_\mathbf{c} \tag{2.20}$$

we can rewrite Equation 2.19 as,

$$\mathbf{v_c} = \frac{mv_{\parallel}^2}{qB^3}\left(\mathbf{B} \times \nabla B\right) \tag{2.21}$$

Adding this with Equation 2.16 gives,

$$\mathbf{v_{cg}} = \left(v_{\parallel}^2 + \frac{1}{2}v_{\perp}^2\right)\frac{\mathbf{B} \times \nabla B}{\omega_g B^2} \tag{2.22}$$

where,

$$\omega_g = \frac{qB}{m} \tag{2.23}$$

Equation 2.22 is known as the gradient-curvature drift (Baumjohann & Treumann [1997]).

2.1.3 Drift Equations

In order to get the guiding center drift equations, one would generally start with Equation 2.5 and do mathematical manipulations in order to separate it into two parts for equatorially mirroring electrons: the drift along the radial trajectory and the drift along the azimuthal trajectory. This is what is done in [Northrup, 1963], however, for the sake of reducing the cumbersome mathematics, the guiding center drift equations will be derived in a slightly different (and less mathematically intensive) manner than presented in [Northrup, 1963].

In the equatorial plane, we are only concerned with the drifts along the radial and azimuthal trajectories; motion along the field line does not concern us. Therefore, when we construct a velocity equation for the total drift, we only need to consider $\mathbf{E} \times \mathbf{B}$ and gradient drift. If we add the two drifts together to get the total drift, $\mathbf{v_T}$, we get,

$$\mathbf{v_T} = \frac{\mathbf{E} \times \mathbf{B}}{B^2} + \frac{m v_\perp^2}{2qB^3} \mathbf{B} \times \nabla B \tag{2.24}$$

This is a vector equation, which we can split into components. It is useful and convenient to use the cylindrical coordinate system - our three directions will be the radial direction, r; the azimuthal direction, ϕ; and the longitudinal direction, z. We will define the magnetic field to be in the longitudinal direction, $\mathbf{B} = B\hat{\mathbf{z}}$, and the electric field will have a component in both the radial and azimuthal directions, $\mathbf{E} = (E_r, E_\phi, 0)$. We can also break the velocity into the radial and azimuthal components (again, we are in the equatorial plane - we need not look at v_z).

At this point, we must consider relativistic factors since we are dealing with high energy electrons that travel at an appreciable fraction of the speed of light. In Equation 2.24, we can define a new factor, M_{NR},

$$M_{NR} = \frac{m_0 v_\perp^2}{2B} \tag{2.25}$$

where m_0 is the rest mass of the particle, which is defined as the non-relativistic magnetic moment (more on this in Section 2.2.1). In order to account for relativistic effects, we use the relationship between relativistic magnetic moment, M_R, and non-relativistic magnetic moment (Roederer [1970]),

$$M_R = \gamma M_{NR} \tag{2.26}$$

where γ is the Lorentz factor,

$$\gamma = \frac{1}{\sqrt{1 - \left(\frac{v}{c}\right)^2}} \tag{2.27}$$

and c is the speed of light in a vacuum. Thus, we may rewrite Equation 2.24 as,

$$\mathbf{v_T} = \frac{\mathbf{E} \times \mathbf{B}}{B^2} + \frac{M}{q\gamma B^2} \mathbf{B} \times \nabla B \tag{2.28}$$

dropping the subscript on M. Equation 2.28 takes into account relativistic effects.

Before we do the mathematics, we need to define the gradient of the magnetic field. We do not need to consider the gradient parallel to the magnetic field, as this is not considered to be in the equatorial plane. Using the definition of the

gradient in cylindrical coordinates, we can define the (perpendicular) gradient of the magnetic field as,

$$\nabla B = \left(\frac{\partial B}{\partial r}, \frac{1}{r}\frac{\partial B}{\partial \phi}, 0 \right) \tag{2.29}$$

If we further define $\mathbf{v_T}$ in component form as,

$$\mathbf{v_T} = \left(\frac{dr}{dt}, r\frac{d\phi}{dt}, 0 \right) \tag{2.30}$$

and substituting Equations 2.29 and 2.30 into Equation 2.28, we obtain a system of equations,

$$\frac{dr}{dt} = \frac{E_\phi}{B} - \frac{M}{qr\gamma B}\frac{\partial B}{\partial \phi} \tag{2.31}$$

$$\frac{d\phi}{dt} = -\frac{E_r}{rB} + \frac{M}{qr\gamma B}\frac{\partial B}{\partial r} \tag{2.32}$$

Equations 2.31 and 2.32 form the guiding center drift equations of motion for particles drifting in the equatorial plane. They are valid under the condition that the particle's gyroradius is small compared to the spatial variations in the magnetic field (Northrup [1963]).

2.2 Adiabatic Invariants

In the study of particle motion in space, it is absolutely necessary to look at the three adiabatic invariants of plasma physics. An adiabatic invariant is a property of a physical system that remains constant over time as long as the changes that occur in the system are slow compared to the periodicities of the particle motion (Baumjohann & Treumann [1997]). The three adiabatic invariants are: magnetic moment, M (first); longitudinal invariant, J (second); and magnetic flux, Φ (third).

2.2.1 First Adiabatic Invariant

The first adiabatic invariant, M, is the magnetic moment of the particle. In a non-relativistic case, the magnetic moment is defined by Equation 2.25. In a relativistic case, the magnetic moment becomes (Degeling et al. [2010]),

$$M = \frac{mc^2}{2B}\left(\gamma^2 - 1\right) \tag{2.33}$$

It can be shown that the magnetic moment of a relativistic particle stays constant, as long as the changes in the magnetic field are slow comparable to the cyclotron period, τ_c (Roederer [1970]),

$$\frac{\tau_c}{B}\frac{dB}{dt} \ll 1 \tag{2.34}$$

where,

$$\tau_c = \gamma\frac{2\pi m_0}{qB} \tag{2.35}$$

for a relativistic particle.

As a particle drifts through one cyclotron orbit around a magnetic field line, it will experience an induced electric field, goverened by Faraday's law,

$$\nabla \times \mathbf{E_{ind}} = -\frac{\partial \mathbf{B}}{\partial t} \tag{2.36}$$

If we apply Stokes' theorem to Equation 2.36, Faraday's law can be rewritten as an integral equation,

$$\oint \mathbf{E_{ind}} \cdot d\mathbf{l} = -\frac{\partial}{\partial t}\iint_S \mathbf{B} \cdot d\mathbf{S} \tag{2.37}$$

where $d\mathbf{l}$ is the line element tangential to the particle trajectory, and S represents the surface the integral is taken over. The work done on the particle by the electric field during a cyclotron orbit is then,

$$\Delta W = -q \oint \mathbf{E_{ind}} \cdot d\mathbf{l} \tag{2.38}$$

where the negative sign comes from the fact the work done on the particle is acting opposite to the direction of motion of the particle (Roederer [1970]).

Observing the right hand side of Equation 2.38, we can use our assumption that the magnetic field changes slowly compared to the cyclotron period (Equation 2.34) and can thus take it out of the integral. This just leaves us with a surface integral over the area enclosed by the particle's cyclotron orbit,

$$\frac{\partial}{\partial t}\iint_S \mathbf{B} \cdot d\mathbf{S} = \pi\rho_c^2\frac{dB}{dt} \tag{2.39}$$

If we bring our attention to the change of energy with respect to time for a particle, we have,

$$\frac{dW}{dt} = m_0c^2\frac{d\gamma}{dt} = \frac{\Delta W}{\tau_c} \tag{2.40}$$

and by inserting the relativistic momentum,

$$p = \gamma m_0 v \tag{2.41}$$

into Equation 2.27, we have our expression for the rate of change of the Lorentz factor,

$$\frac{d\gamma}{dt} = \frac{1}{2m_0^2 c^2 \gamma} \frac{d\left(p^2\right)}{dt} \tag{2.42}$$

Combining Equations 2.15, 2.37, 2.38, 2.40, and 2.41, along with the fact that since we are in the equatorial plane, $p = p_\perp$, we have,

$$\frac{dp_\perp^2}{dt} = \frac{p_\perp^2}{B} \frac{dB}{dt} \tag{2.43}$$

Since we have our assumption that the magnetic field is varying slowly, this tells us that $p_\perp^2/B$ from Equation 2.43 is constant. Hence, if we divide by the (constant) factor $2m_0$, we have that,

$$\frac{p_\perp^2}{2m_0 B} = \kappa \tag{2.44}$$

where κ is a constant. Inserting the non-relativistic definition of momentum into Equation 2.44, we have,

$$\frac{m_0 v_\perp^2}{2B} = \kappa = M \tag{2.45}$$

which is Equation 2.25. Therefore, as long as the magnetic field varies slowly compared to τ_c, the magnetic moment, or first adiabatic invariant, of a particle will be a constant of the system (Roederer [1970]).

2.2.2 Second Adiabatic Invariant

The second adiabatic invariant, J, is known as the longitudinal invariant. The longitudinal invariant is associated with the bounce motion of a particle along a particular field line, defined by,

$$J = \oint p_\parallel ds \tag{2.46}$$

where $p_\parallel$ is the parallel component of the particle's momentum (along the field line) and ds is the infinitesimal length element along the field line. Equation 2.46 is taken over a complete bounce of a particle (i.e. from one mirror point to

the opposing mirror point, then back to the original mirror point, provided the particle is not lost to the atmosphere).

During the bounce motion of a particle, through conservation of the first adiabatic invariant, we can develop a relationship between the magnetic field and the pitch angle of the particle,

$$\frac{\sin^2 \alpha\,(s)}{B\,(s)} = \frac{\sin^2 \alpha_i}{B_i} \tag{2.47}$$

where α_i and B_i are the pitch angle and magnetic field strength at the particle's initial position, and s is the coordinate along the field line (Baumjohann & Treumann [1997]).

We can, therefore, write an equation for the parallel component of the particle's velocity,

$$v_{\parallel}\,(s) = v \cos \alpha\,(s) = v \left[1 - \frac{B\,(s)}{B_i} \sin^2 \alpha_i\right]^{\frac{1}{2}} \tag{2.48}$$

Now, if we have a particular magnetic field strength,

$$B_m = B\,(s_m) = \frac{B_i}{\sin^2 \alpha_i} \tag{2.49}$$

where s_m is the location of the mirror point on the field line, and insert this into Equation 2.48, the parallel component of the velocity becomes zero. This is how the mirror point is defined: where the parallel component of the particle's velocity becomes zero and through conservation of momentum, the particle must reverse its direction. The particle will travel to the opposing mirror point on the opposite hemisphere, where the parallel velocity will become zero once again, and the particle will travel towards the first mirror point - it will keep bouncing between mirror points. If, however, the mirror point is actually located deep within Earth's atmosphere, the particle will be absorbed by the atmosphere through collisions and will no longer execute bounce motion - it will precipitate towards the surface of the Earth (Baumjohann & Treumann [1997]).

The time scale for bounce motion is given by the bounce period, τ_b, defined by (Roederer [1970]),

$$\tau_b = 2 \int_{s_m}^{s'_m} \frac{ds}{v_{\parallel}\,(s)} \tag{2.50}$$

The longitudinal invariant, J, will be conserved as long as the magnetic field changes slowly in comparison to the bounce period, τ_b. Mathematically, this is given by (Roederer [1970]),

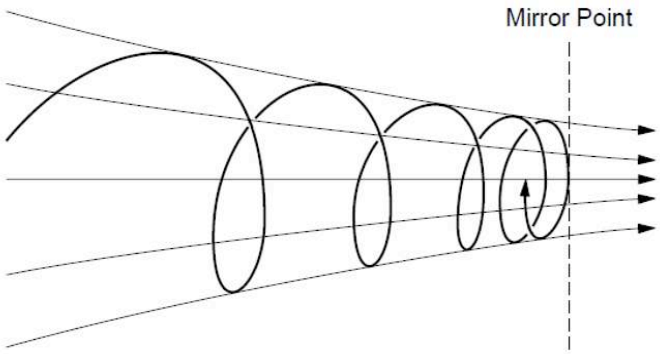

Figure 2.4: A particle undergoing both gyro and bounce motion, reaching its mirror point (from [Baumjohann & Treumann, 1997]).

$$\frac{\tau_b}{B}\frac{dB}{dt} \ll 1 \tag{2.51}$$

However, for the purpose of our work, the second adiabatic invariant will always be conserved. J deals with motion parallel to the magnetic field line and hence, off of the equatorial plane. Our work deals strictly with electrons mirroring in the equatorial plane, thus, J will always be zero.

2.2.3 Third Adiabatic Invariant

The third adiabatic invariant, Φ, is known as the magnetic flux. The magnetic flux is a surface integral of the magnetic field over a closed drift shell, defined by (Baumjohann & Treumann [1997], Griffiths [1998]),

$$\Phi = \oint_{\Sigma} \mathbf{B} \cdot \mathrm{d}\mathbf{\Sigma} \tag{2.52}$$

where Σ defines the drift shell in which we integrate over. Equation 2.52 is taken over what is known as the guiding drift shell (i.e. the drift shell the particle would follow when the magnetic field is static).

The drift period, τ_d, is defined by (Roederer [1970]),

$$\tau_d = \oint \frac{\mathrm{d}x}{\langle V_0 \rangle} \tag{2.53}$$

where V_0 is the particle drift velocity on a particular drift shell and dx defines the arc length of the intersection of the drift shell with the reference surface defined by Ω. Out of all the periodicities, the drift period is the longest. In general (Roederer [1970]),

$$\tau_c \ll \tau_b \ll \tau_d \tag{2.54}$$

In order for the third adibatic invariant to be conserved, like the first two invariants, we require that the magnetic field changes slowly compared to the drift period. Mathematically (Roederer [1970]),

$$\frac{\tau_d}{B}\frac{dB}{dt} \ll 1 \tag{2.55}$$

When particles move across different drift shells, this violates the third adiabatic invariant - this plays an important role in radial transport, which is a major focus of this thesis (Baumjohann & Treumann [1997]).

2.2.4 Particle Motion and the Adiabatic Invariants

As has been mentioned already, each adiabatic invariant is associated with a particular type of particle motion. The first adiabatic invariant is associated with a particle gyrating around a magnetic field line (gyromotion or cyclotron motion); the second adiabatic invariant is associated with bounce motion between the mirror points on a specific magnetic field line; and the third adiabatic invariant is associated with drift motion around Earth on a closed drift shell. These different motions can be see in Figure 2.6. In the real world, a particle is under the influence of all three motions at a given time; we assume $J = 0$ in this thesis and hence our calculations correspond to particle motion in the equatorial plane.

2.2.5 Violation of the Adiabatic Invariants

In this chapter, Equations 2.34, 2.51, and 2.55 are the conditions for respective adiabatic invariants to remain constant - the magnetic field must vary slowly compared to the periodicity of the specific motion associated with the adiabatic invariant. However, what happens when Equations 2.34, 2.51, and 2.55 are not satisfied? If that is the case, then we say there is a violation of the adiabatic invariant.

If Equation 2.34 does not hold, we have a violation of the first adiabatic invariant. In this case, the time variations are faster than the cyclotron period, which deals with high frequency variations in either the magnetic field or the electric field. If we do have a violation of the first adiabatic invariant, we must abandon

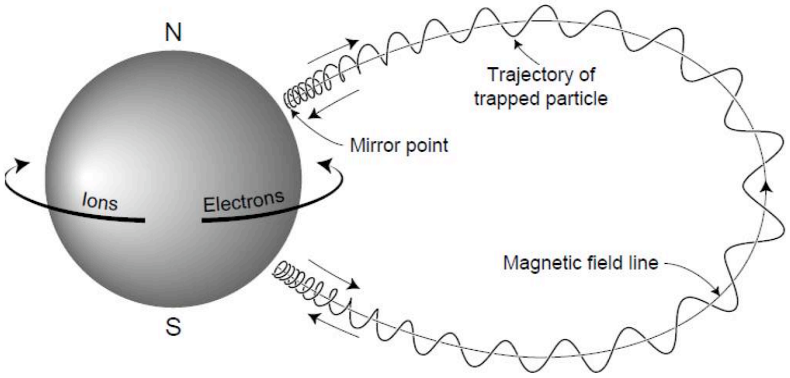

Figure 2.5: Gyro, bounce, and drift motions for ions and electrons near Earth (from [Baumjohann & Treumann, 1997]).

the guiding center approach and consider full particle motion (Baumjohann & Treumann [1997]).

If Equation 2.51 does not hold, we have a violation of the second adiabatic invariant. In this case, the time variations are faster than the bounce period, but smaller than the cyclotron period. Since J is no longer conserved, the bounce motion between the two mirror points on a given field line can no longer be considered as a simple oscillation (Baumjohann & Treumann [1997]).

If Equation 2.55 does not hold, we have a violation of the third adibatic invariant. In this case, the time variations are faster than the drift period, but smaller than the cyclotron and bounce periods. When Φ is violated, we have particles that are moving across different drift shells due to the variation in the magnetic field (i.e. it is no longer static) (Baumjohann & Treumann [1997]).

Since violation of the third adibatic invariant deals with particles moving across different drift shells, it will be our primary focus. The first adiabatic invariant will remain constant, as will the second adiabatic invariant, as it is zero at all times (for our purposes).

2.3 Radial Transport

As mentioned in the previous section, if a particle violates the third adiabatic invariant, it moves across different drift shells. In order to discuss, in depth, the major goals of this project, it is necessary to ascertain knowledge of radial transport in the radiation belts. Transport is just one of the four mechanisms that ensure the existence of the radiation belts; the other three mechanisms are injection, loss, and acceleration (part of this process is coupled to the transport process) (Roederer [1970]). Transport can be characterized as either diffusive or convective. Diffusion itself can be broken down into two categories: radial diffusion and pitch angle scattering.

2.3.1 Fokker-Planck Equation

The transport of particles in the radiation belts is governed by the Fokker-Planck equation,

$$\frac{\partial f^k}{\partial t} = \sum_{n=1}^{3} \frac{\partial}{\partial x_n^k} \left[\sum_{m=1}^{3} D_{nm} J_{0k} \frac{\partial}{\partial x_m^k} \left(\frac{f^k}{J_{0k}} \right) \right] + Q - S \tag{2.56}$$

where f^k is the distribution function in k-space, D_{nm} is the diffusion tensor, J_{0k} is the Jacobian, and Q and S represent the source and sink terms. The diffusion tensor is given by,

$$D_{nm} = \frac{\left\langle \left(\Delta x_n^k \Delta x_m^k \right) \right\rangle}{2\tau_b} \tag{2.57}$$

where τ_b is the particle bounce time, Δx_n^k and Δx_m^k represent the scattered variables, and the angled brackets represent bounce average (Roederer [1970]).

The Jacobian is defined by,

$$J_{0k} = \frac{\partial \left(\Phi, J, M \right)}{\partial \left(x_1^k, x_2^k, x_3^k \right)} \tag{2.58}$$

If we do not allow for cross-coefficients in the diffusion tensor (i.e. no hybrid violations of the adiabatic invariants), Equation 2.57 simplies to,

$$D_{nn} = \frac{\left\langle \left(\Delta x_n^k \right)^2 \right\rangle}{2\tau_b} \tag{2.59}$$

If we now restrict our attention to motion that violates the third adibatic invariant, Φ, the diffusion tensor will only have one non-zero element (i.e. $D_{33} \neq 0$). This allows us to simplify Equation 2.56 (Roederer [1970]),

$$\frac{\partial f}{\partial t} = \frac{\partial}{\partial L}\left[\frac{D_{LL}}{L^2}\frac{\partial}{\partial L}\left(L^2 f\right)\right] + Q - S \tag{2.60}$$

Re-defining variables in Equation 2.60 (i.e. $\tilde{D}_{LL} = D_{LL}/L^2$ and $\tilde{f} = L^2 f$) allows us to rewrite it as,

$$\frac{\partial f}{\partial t} = D_{LL}\frac{\partial^2 f}{\partial L^2} + \frac{\partial D_{LL}}{\partial L}\frac{\partial f}{\partial L} + Q - S \tag{2.61}$$

Comparing Equation 2.61 with the Smoluchowski (convection-diffusion) equation (assuming the diffusion coefficient, D, is constant),

$$\frac{\partial f}{\partial t} = D\nabla^2 f - \mathbf{v}\cdot\nabla f + Q - S \tag{2.62}$$

where the first term on the right-hand side represents diffusive transport and the second term on the right-hand side represents convective transport, we can see that Equation 2.61 has both terms to represent the diffusive and convective modes of transport (where in Equation 2.62, $\nabla \rightarrow \partial/\partial L$)

Equation 2.61 is a partial differential equation that describes the time evolution for the distribution function of the particles, f. The distribution function gives the number of particles per unit volume in space; it is a function of seven variables: three that govern the position of the particle (Q_i), three that govern the canonical momentum of the particle (P_i), and the time coordinate (t). We can write this as $f = f(Q_i,P_i,t)$, where i =1,2,3.

From Hamiltonian mechanics, we can write the temporal evolution of f, governed by Liouville's theorem as,

$$\frac{df}{dt} = \frac{\partial f}{\partial t} + \sum_{i=1}^{3}\left[\frac{dP_i}{dt}\frac{\partial f}{\partial P_i} + \frac{dQ_i}{dt}\frac{\partial f}{\partial Q_i}\right] = 0 \tag{2.63}$$

which states that the distribution function remains constant along its trajectory in phase space (that is, it moves through the phase space in an incompressible manner). If we know the Hamiltonian of the system, $H = H(q_i,p_i,t)$, from the study of Hamiltonian mechanics, we can obtain the canonical coordinates from,

$$\frac{dP_i}{dt} = -\frac{\partial H}{\partial Q_i} \tag{2.64}$$

$$\frac{dQ_i}{dt} = \frac{\partial H}{\partial P_i} \tag{2.65}$$

In radiation belt physics, however, it is not intuitive to use the canonical coordinates derived from the Hamiltonian of the system, as the canonical coordinates are not locally observable. Instead, we move to a non-canoncial position-momentum distribution $f = f(\mathbf{r},\mathbf{p},t)$, using the following transformation between canonical and non-canonical momentum (the canonical coordinate for position is the same as the non-canonical coordinate for position),

$$\mathbf{p} = \mathbf{P} - \frac{q}{c}\mathbf{A} \tag{2.66}$$

where $\mathbf{A}$ is the electromagnetic vector potential (Schulz & Lanzerotti [1974]).

2.3.2 Convection and Diffusion

In looking at radial transport, it can be broken down into two modes of transport: convection and diffusion. We seek to briefly examine the details of both modes of transport, which will be discussed again in Chapter 5.

2.3.2.1 Convection

Convection (also known as advection) is the bulk transport of particles. From examining both the Fokker-Planck (Equation 2.61) and Smoluchowski (Equation 2.62) equations, it can be noted that convection is linked to diffusion through the diffusion coefficient, D_{LL}. Thus, both convective and diffusive transport processes are important in the examination of radial transport in the radiation belts.

2.3.2.2 Diffusion

The other radial transport mechanism we want to examine is diffusion. Diffusion differs from convection in that particles undergoing a diffusive process spread out in the medium, with bulk transport not being required.

Although we are only looking at motion in the equatorial plane (hence, radial transport), we can briefly discuss pitch angle diffusion alongside radial diffusion for completeness.

Radial Diffusion Radial diffusion comes about from violation of the third adiabatic invariant, Φ. As particles diffuse closer to Earth across drift shells, they

encounter a stronger magnetic, that varies as r^{-3}. In order to conserve M (Equation 2.25), the first adibatic invariant, this will require that the perpendicular kinetic energy of particles must increase. Hence, there is a one-to-one relationship between radial diffusion and acceleration (Schulz & Lanzerotti [1974]). If we have a perturbation, τ_{per}, that follows,

$$\tau_d \sim \tau_{per} \gg \tau_b \gg \tau_c \tag{2.67}$$

with the perturbation being on the order of minutes, then we will have violation of the third adibatic invariant and thus, we will be effectively dealing with radial diffusion (and acceleration) in the radiation belts (Roederer [1970]).

Pitch Angle Diffusion If one moves off the equatorial plane, this requires consideration of pitch angle diffusion. Pitch angle diffusion arises from a change in the location of the mirror points along a magnetic field line. As mentioned, particles that move along a field line will bounce between their mirror points; if a mirror point is within the loss cone (that is, the region where the particles undergo frequent collisions with neutral particles in the ionosphere) (Baumjohann & Treumann [1997]), this particle will become lost to the atmosphere and precipitate towards Earth. For this reason, pitch angle scattering is considered a loss mechanism, since it removes particles from the radiation belts. This is also the reason why pitch angle scattering controls the lifetime of a particle (Roederer [1970]).

2.3.3 Diffusion Coefficient

The diffusion coefficient, D_{LL}, describes the average rate of radial transport of particles in a system (Elkington [2006]). For the case of diffusion being proportional to L shell, the further the particles are from Earth, the greater the rate of radial transport and vice-versa. Table 2.1 is a collection of calculated diffusion coefficients over the years; this table is a reproduction of the one found in [Elkington et al., 2003].

The equation used to calculate the diffusion coefficient is given by,

$$D_{LL} = \frac{\left\langle (\Delta L)^2 \right\rangle}{2\tau} \tag{2.68}$$

In the numerator, ΔL represents the change in position of the particle undergoing diffusion, in that it is the difference between the final position (after the particle has undergone diffusion) and the initial position (before the particle undergoes diffusion). The angular brackets represent an ensemble average over the azimuthal angle. In the denominator, τ represents the timescale for running the

Table 2.1: Examples of radial diffusion coefficients that were determined emperically (from [Elkington et al., 2003]).

D_{LL} (day^{-1})	L	Reference
2.0×10^{-7}	$L = 1.20$	[Newkirk & Walt, 1968a]
$10^{-8}\ L^{(10\pm1)}$	$1.76 \leq L \leq 5.0$	[Newkirk & Walt, 1968b]
4 - $8 \times 10^{-10}\ L^{10}$	$3.0 \leq L \leq 5.0$	[Lanzerotti et al., 1970]
$2.7 \times 10^{-5}\ M^{-0.5}\ L^{7.9}$	$1.7 \leq L \leq 2.6$	[Tomassian et al., 1972]
$10^{(0.75K_{FR}-10.2)}$	$L = 4$	[Lanzerotti & Morgan, 1973]
$(2.23\pm0.67)\omega_d^{-1.1\pm0.15}$	$L = 6.0$	[Holzworth & Mozer, 1979]
$\sim$0.2 - 5.0	$L = 5.3$, $L = 6.1$	[Chiu et al., 1988]
$2.1 \times 10^{-3}\ \left(\frac{L}{4}\right)^{\ 11.7\pm1.3}$	$3.0 \leq L \leq 6.0$	[Selesnick et al., 1997]

diffusion model. The condition for this timescale that we require is that $\tau \gg \tau_d$, the drift period of the particle (Elkington et al. [2003]).

We now move on to the next major sections of the thesis: talking about the wave drivers (and waves themselves), followed by a description of the ULF wave model being used and how we will examine radial transport of particles in the outer radiation belt.

Chapter 3

Magnetohydrodynamic Wave Mechanics

In the first two chapters of this thesis, we have painted the big picture of magnetospheric physics. In the first chapter, we discussed such things as the composition of the magnetosphere, the solar wind, geomagnetic storms and associated properties, the radiation belts, and ULF waves. This set up the environment in which we will examine the physics of interest in this thesis. In the second chapter, we talked about the motion of particles and adiabatic invariants, which set up the general idea for radial transport, the main focus the thesis.

Now, before we can get into the main analysis of diffusion, we have to ask ourselves one simple question: what drives ULF waves in the magnetosphere? It is in this chapter we seek to answer that very question.

3.1 Fourier Analysis

3.1.1 Fourier Transform

In Fourier analysis, any periodic function, $f(t)$, can be constructed with a combination of sine and cosine functions, with varying amplitudes and frequencies, such that,

$$f(t) = \sum_n A_n e^{-i\omega_n t} \tag{3.1}$$

where A_n represents the various amplitudes and ω_n represents the various frequencies. It is of interest in many scientific and engineering applications to determine the frequency components of an input signal, $f(t)$. This can be done through what is known as a Fourier transform.

Mathematically, the Fourier transform is defined by,

$$\mathcal{F}(\omega) = \int_{-\infty}^{+\infty} f(t)\, e^{i\omega t} dt \tag{3.2}$$

which takes a signal as a function of time, $f(t)$, and transforms it into a function of frequency, $\mathcal{F}(\omega)$. By applying the Fourier transform on Equation 3.1, this extracts the amplitudes as a function of frequency of the sine and cosine waves that make up $f(t)$.

3.1.2 Application to Magnetospheric Physics

Now, why is this important in the study of magnetospheric physics? When the solar wind is launched towards Earth, it will eventually come in contact with the magnetosphere. When the solar wind hits the magnetospheric boundary, the variances in pressure will cause compression and relaxation of this boundary, which launches waves into the magnetospheric cavity. We seek to examine the process of energy transfer from the launched waves to the magnetic field lines inside the cavity. In order for this energization process to occur, the frequency of the wave must match the eigenfrequency of the field line; if this condition is satisfied, it will drive oscillations of the field line (which is known as a field line resonance).

If we think of the pressure pulse of the solar wind as a signal in the time domain, $f(t)$, then by applying the Fourier transform to the pulse, we can extract information about the amplitudes and frequencies that make up the pulse, given by $\mathcal{F}(\omega)$.

As well, during the field line energization process, we are interested in looking at the power spectrum, as it will peak at the resonant frequency, ω_0, which gives us the eigenfrequency of the field line. The power spectrum is given by,

$$P(\omega) = |\mathcal{F}(\omega)|^2 \tag{3.3}$$

which is just the square of the modulus of the Fourier transform of the original signal.

3.1.3 Aliasing

One area of caution that needs to be emphasized in the whole process of signal analysis is the concept of aliasing. In signal processing, aliasing refers to the phenomenon of one signal becoming indistinguishable from another signal during the process of sampling the signal (i.e. a signal acts as the alias of another).

For a signal composed of a finite number of frequencies with a maximum frequency, ν_{max}, we will have a condition to satisfy that prevents signals from becoming indistinguishable during sampling, that is,

$$\nu_s > 2\nu_{max} \tag{3.4}$$

We require the sampling frequency, ν_s, to be twice as great as the maximum frequency of the signal. Another way this condition is written is,

$$\frac{\nu_s}{2} > \nu_{max} \tag{3.5}$$

where $\frac{\nu_s}{2}$ is known as the Nyquist frequency, ν_{Nyq}. If we satisfy Equation 3.4 (or 3.5), then we will not have an issue with aliasing.

3.1.4 Examples

To conclude this section on Fourier analysis, a couple of examples on how the Fourier transform works will be given, so as to explicitly demonstrate the purpose of the tranform and for overall completeness.

The first function we shall choose is a very simple trigonometric function: the sine wave. We will use a generic sine wave of the form,

$$f(t) = \sin(2\pi\nu t) \tag{3.6}$$

where ν is the frequency of the wave.

In Figure 3.1, we show the case of $\nu = 3$ mHz. The top frame shows the plot of the sine wave as a function of time. The center frame shows the Fourier transform of the sine wave with a distinct peak at 3 mHz, which is the expected result, as Equation 3.2 picks out the wave frequency. The bottom frame shows the power spectrum of the same wave, which also, as expected, has a peak at 3 mHz.

For the second example, we shall take a superposition of sine waves with two different frequencies and check to see that the Fourier transform picks out the correct frequencies. We take a wave of the form,

$$f(t) = \sin(2\pi\nu_1 t) + \sin(2\pi\nu_2 t) \tag{3.7}$$

with the condition $\nu_1 \neq \nu_2$.

From the top frame in Figure 3.2, we can see we have a periodic signal that is composed of more than a single frequency. The center and bottom panels of Figure 3.2 show that the Fourier transform has identified the frequencies that make up the signal: $\nu_1 = 2$ mHz and $\nu_2 = 7$ mHz. These were the input

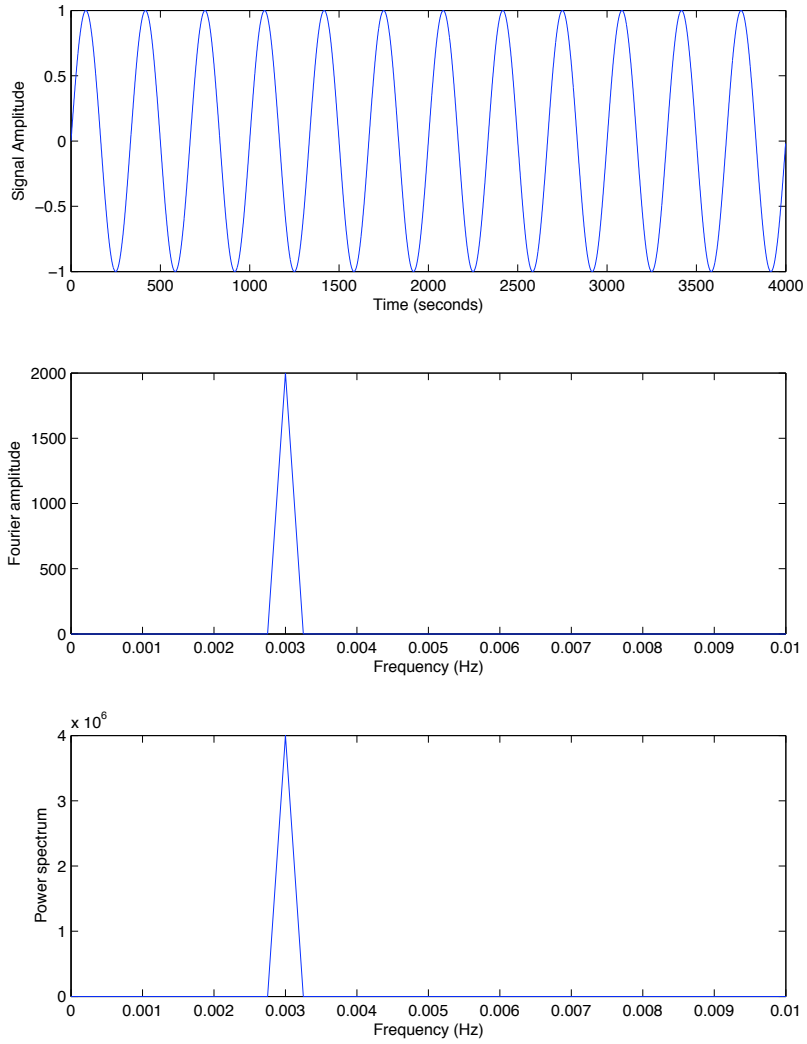

Figure 3.1: Top: A plot of the function $f(t) = \sin(2\pi\nu t)$ with frequency 3 mHz. Center: Fourier transform of $f(t)$ showing a peak at 3 mHz. Bottom: Power spectrum of $f(t)$ showing a peak at 3 mHz.

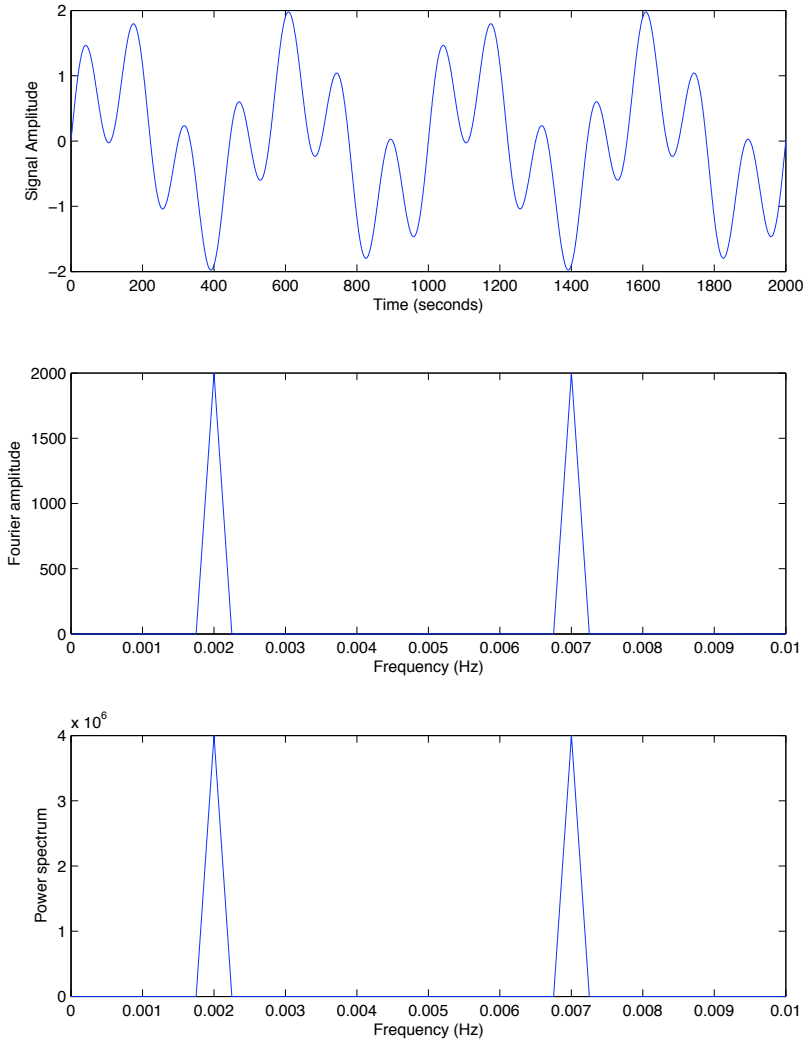

Figure 3.2: Top: A plot of the function $f(t)$ with frequencies 2 mHz and 7 mHz. Center: Fourier transform of $f(t)$ showing a peak at 2 mHz and 7 mHz. Bottom: Power spectrum of $f(t)$ showing a peak at 2 mHz and 7 mHz.

frequencies in Equation 3.7, demonstrating that the Fourier transform picks out the frequencies that are used to construct the sine (and cosine) waves that make up the original signal.

3.2 Pressure Pulse

Magnetospheric pulsations can be driven by either an internal or external driver. An internal driver, one in which the driving mechanism is inside the magnetospheric cavity, would be something like unstable plasma configurations. An external driver, one in which the driving mechanism is outside the magnetospheric cavity, would be something such as a velocity shear at the magnetopause (the Kelvin-Helmholtz stability, which was described in Chapter 1) or from fluctuations in the dynamic pressure of the solar wind (Claudepierre et al. [2010]).

3.2.1 Pulse Composition

The theory behind a pressure pulse impacting the magnetosphere is that the pulse is a representation of a linear superposition of compressional waves with different frequencies (Degeling et al. [2011]). When this pulse hits the magnetopause, the magnetosphere acts as a filter: it will allow some of the waves (and their respective frequencies) in the pressure pulse to pass through and, in the process, excite field lines in the magnetospheric cavity; the remaining waves will be deflected around the magnetosphere.

An important aspect of the pressure pulse is its duration. Our goal is to examine the response of the magnetosphere to a pulse with a very short duration. The reason for this is that discontinuities in the solar wind are thought to excite a broad spectrum of waves in the magnetospheric cavity. There can be a significant transfer of energy in this process, which is important as far as explaining how ULF waves transport and energize radiation belt electrons. This is a key aspect of the thesis.

Our interest in decomposing a pressure pulse into a sum of frequencies is that it allows us to straightforwardly analyze how energy is transferred to natural oscillations of the geomagnetic field. The complete set of field lines in the magnetosphere in which we want to examine resonant interactions is known as the Alfvén continuum.

Our hypothesis is that the Alfvén continuum is excited by a broadband spectrum (impulse) of compressional waves impacting the magnetospheric boundary. The continuum of field line oscillations is a useful diagnostic for the effect of impulses on the magnetosphere, since it is an observable that can be monitored from the ground and in-situ.

3.2.2 Pulse Travel

The solar wind travels outwards from the Sun at speeds ranging from 300 km/s to over 1,000 km/s. In the frame of the solar wind, we consider a discontinuity as a superposition of compressional waves that propagate at the Alfvén speed in the medium, which is generally much less than the solar wind speed. Transforming to the frame of the magnetosphere, the wave frequency is Doppler shifted to $\omega \sim kV$, where $2\pi/k$ is the scale of the disturbance in the solar wind, and V is the solar wind speed. The view we are taking is that spatial structure in the solar wind (such as a discontinuity in pressure) is essentially wavelike at frequency ω in the frame of the magnetosphere. Therefore, it would appear to the stationary obsever, in their reference frame, that the Alfvén wave (pressure pulse) is having its wavelength contracted via the Doppler effect.

3.2.3 Discontinuities

As mentioned in Section 1.2, as the solar wind approaches Earth, the magnetopause acts to retard the motion of the solar wind. As the solar wind cannot easily penetrate Earth's magnetic field, much of it is deflected around Earth at a reduced velocity. This creates two fluid layers: one layer is the solar wind flowing towards Earth and the other layer is the plasma that is slowed down due to the presence of Earth's magnetosphere that ends up being deflected around Earth (as can be seen in Figure 3.3). In between two fluid layers is a narrow boundary known as a discontinuity; in the case of the boundary between the fast flowing solar wind and the retarded solar wind, this is what we have defined to be the bow shock (Baumjohann & Treumann [1997]).

The magnetopause also acts as a discontinuity (Baumjohann & Treumann [1997]), as it separates two fluid layers. On one side of the magnetopause, there is the plasma that was slowed down by the presence of the magnetosphere. On the other side, there is the stationary plasma inside the magnetospheric cavity. It is the generation of waves from the compression of the magnetopause that is of interest to us.

We consider that spatial structure in the solar wind produces (through the Doppler effect) wavelike compressional disturbances propagating on the magnetopause. This is illustrated in Figure 3.3, which is taken from [Walker, 2002]. The vertical arrows labeled 1.9 mHz and 3.3 mHz indicate corresponding wavelengths in the solar wind. The Alfvén (V_A), solar wind (V), and sound (V_s) speeds are also indicated. The important point to note is that V_A and V_s are much less than V, which we have assumed.

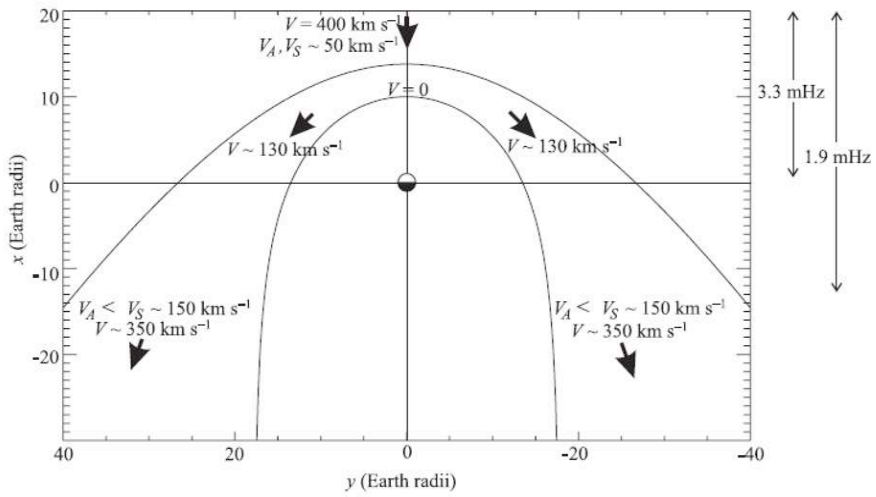

Figure 3.3: Showing the flow speed of the solar wind as it approaches the magnetosphere, then as it passes around the flanks (from [Walker, 2002]).

3.3 Magnetohydrodynamic (MHD) Waves

We have, so far, discussed how waves are generated in the magnetosphere, either by internal or external sources. The next logical question that comes up is, "Do MHD waves have some sort of classification system?" The answer to that is yes. MHD waves are separated by their direction of propagation and the speed at which they travel. In order to look at the classification system, we must first examine (briefly) how the dispersion relation is derived.

3.3.1 Dispersion Relations

To derive the dispersion relation (that is, the relation between frequency and wave number) for MHD waves, we make use of the ideal MHD equations.

3.3.1.1 Continuity Equation

The continuity equation states that the rate at which mass enters a system is balanced by the rate at which mass flows out the system (i.e. what goes in to the system goes out of the system). Mathematically, this is given by,

$$\frac{\partial \rho}{\partial t} + \nabla \cdot (\rho \mathbf{v}) = 0 \tag{3.8}$$

where ρ represents the density of the plasma and $\mathbf{v}$ is the plasma velocity.

3.3.1.2 Conservation of Momentum

The equation for conservation of momentum describes the non-relativistic momentum transport in a continuum. Mathematically, this is given by,

$$\rho \left(\frac{\partial}{\partial t} + \mathbf{v} \cdot \nabla \right) \mathbf{v} = \mathbf{J} \times \mathbf{B} - \nabla P \tag{3.9}$$

where $\mathbf{J}$ is the current density of the plasma, $\mathbf{B}$ is the magnetic field of the plasma, and P is the plasma pressure.

3.3.1.3 Ampère's Law

Ampère's Law, neglecting displacement current (as we are looking at low frequency waves), relates the magnetic field of a closed loop to the current that passes through the closed loop. Mathematically, this is given by,

$$\nabla \times \mathbf{B} = \mu_0 \mathbf{J} \tag{3.10}$$

where μ_0 is the permeability of free space.

3.3.1.4 Faraday's Law

Faraday's law is the fundamental relation between the electric and magnetic fields. Mathematically, this is given by,

$$\nabla \times \mathbf{E} = -\frac{\partial \mathbf{B}}{\partial t} \tag{3.11}$$

where $\mathbf{E}$ is the electric field of the plasma.

3.3.1.5 MHD Formalism

In order to work with these equations, we have some assumptions that we need to apply. The first two assumptions of ideal MHD theory are that the background velocity of the plasma, $\mathbf{v_0}$, and the background electric field, $\mathbf{E_0}$, are zero (we may consider that our analysis is done in the solar wind frame). For the magnetic field and plasma density, we have the background quantity with a small linear

perturbation added to it (i.e. $\mathbf{x} = \mathbf{x_0} + \delta\mathbf{x}$), under the assumption that the perturbation is much smaller than the background quantity (i.e. $\delta\mathbf{x} \ll \mathbf{x_0}$).

Under ideal MHD, for plasma velocity, plasma density, plasma electric and magnetic fields, we have,

$$\mathbf{v} = \delta\mathbf{v} \tag{3.12}$$

$$\rho = \rho_0 + \delta\rho \tag{3.13}$$

$$\mathbf{E} = \delta\mathbf{E} \tag{3.14}$$

$$\mathbf{B} = \mathbf{B_0} + \delta\mathbf{B} \tag{3.15}$$

As well, under the assumption that the pressure is nearly isotropic (i.e. no shears) and that the magnetic field is approximately homogeneous, we also have the condition that (Baumjohann & Treumann [1997]),

$$\nabla\left(P_0 + \frac{B_0}{2\mu_0}\right) = 0 \tag{3.16}$$

which allows us to get rid of any reference to pressure in Equation 3.9.

By applying Equations 3.12, 3.13, 3.14, 3.15, and 3.16, to Equations 3.8, 3.9, 3.10, and 3.11, keeping the perturbations linear in order, and having an equation only in terms of $\delta\mathbf{v}$, we get the following second-order equation,

$$\frac{\partial^2\delta\mathbf{v}}{\partial t^2} = c_{ms}^2\nabla\left(\nabla\cdot\delta\mathbf{v}\right) + v_A^2\left(\nabla_\parallel^2\delta\mathbf{v} - \nabla\nabla_\parallel\delta v_\parallel - \hat{\mathbf{e}}_\parallel\nabla_\parallel\nabla\cdot\delta\mathbf{v}\right) \tag{3.17}$$

where c_{ms}^2 is the magnetosonic speed, defined by,

$$c_{ms}^2 = c_s^2 + v_A^2 \tag{3.18}$$

where c_s is the speed of sound and v_A is the Alfvén speed, defined by,

$$v_A = \frac{B}{\sqrt{\mu_0\rho}} \tag{3.19}$$

In Equation 3.17, the parallel direction is defined as the direction along the magnetic field line.

Now, we introduce a travelling wave of the form,

$$\delta \mathbf{v} = \delta \mathbf{v_0} e^{i(\mathbf{k}\cdot\mathbf{r} - \omega t)} \tag{3.20}$$

where $\delta \mathbf{v_0}$ represents an arbitrary wave amplitude, $\mathbf{k}$ is the wave vector, $\mathbf{r}$ is the radial vector, and ω is the wave frequency. Applying Equation 3.20 to Equation 3.17, after some algebra, we get a tensor equation,

$$\left[\left(\omega^2 - k_\parallel^2 v_A^2\right)\mathbf{I} - c_{ms}^2 \mathbf{k}\mathbf{k} + \left(\mathbf{k}\hat{\mathbf{e}}_\parallel + \hat{\mathbf{e}}_\parallel \mathbf{k}\right) k_\parallel v_A^2\right] \cdot \delta \mathbf{v_0} = 0 \tag{3.21}$$

where $\mathbf{I}$ represents the identity matrix. The only useful solutions will come from the condition that $\delta \mathbf{v_0} \neq 0$. This requires the determinant of the term in square brackets to be zero. Equation 3.21 allows us to look at the dispersion relation for different waves.

3.3.2 MHD Wave Classification

3.3.2.1 Shear Alfvén Wave

From Equation 3.21, there is one dispersion relation that results from decoupling in the system. This is known as the shear Alfvén mode, which has the following dispersion relation,

$$\omega_A^2 = k_\parallel^2 v_A^2 \tag{3.22}$$

The shear Alfvén wave propagates parallel to the magnetic field line at the Alfvén speed, defined by Equation 3.19. While the wave travels along the field line, there will be a perturbation perpendicular to the magnetic field which serves to change its direction (keeping the magnitude of the field constant).

3.3.2.2 Slow Mode Wave

In Equation 3.21, there is a coupling between the parallel and perpendicular components of the velocity. When this is decoupled, we get the following dispersion relation,

$$\omega_S^2 = k_\parallel^2 c_s^2 \tag{3.23}$$

This is known as the slow mode or ion acoustic wave, which propagates parallel to the magnetic field at the speed of sound. While the wave travels along the field line, there will be a perturbation perpendicular to the magnetic field which serves to change its direction (keeping the magnitude of the field constant). When the solar wind comes into contact with the magnetosphere, this is a fast mode (compressional) shock, hence, for the purpose of this thesis, slow modes will not be considered (it is only here for completeness in the discussion of MHD waves).

3.3.2.3 Fast Mode Wave

There are two wave modes present from the decoupling of the velocity component in Equation 3.21. One is the slow mode and the other is known as the fast mode or magnetosonic wave. The fast mode has the following dispersion relation,

$$\omega_F^2 = k^2 c_{ms}^2 \tag{3.24}$$

The fast mode, unlike the Alfvén and slow modes, does not travel parallel to the magnetic field line. The fast mode propagates isotropically (i.e. it has components of the wavevector parallel and perpendicular to B), which allows for compression of the field lines. This property of the fast mode is of great interest to the research in this thesis.

3.4 Afterword

Now that we have a working knowledge of the physics involved and just how we generate waves in the magnetosphere, it is time to move on to the core part of this thesis: the specifics of the ULF wave model that we will be using (along with some of the mathematics involved) as well as looking at radial transport in the radiation belts.

Chapter 4

ULF Wave Model

So far, we have cemented our knowledge in three key areas: we have an understanding of the environment we are examining (the magnetosphere); we have an understanding of the physics we are investigating in the magnetosphere (radial transport); and we have an understanding of MHD waves and how to categorize them. We now add one more piece to the puzzle: we need to understand the computational model that will be used to describe MHD wave propagation in the magnetosphere, whose results will allow us to look at radial transport in the outer radiation belt, which is our ultimate goal.

In this chapter, we consider the excitation of ULF waves that arise from a wave driver on the magnetopause boundary. We will see that this driver can set up global oscillations in the magnetospheric cavity and that the spectra of waves that we excite at a specific location is in agreement with the theoretical predictions of the Alfvén continuum. We consider the cases of low, moderate, and high solar wind speed in order to demonstrate that the amplitude of the waves that are excited vary in proportion to the solar wind speed.

We first examine how the wave equation, which governs the model, is actually derived, along with specific aspects of the model (the magnetic field structure, the magnetopause boundary, density profile, wave driver). Then we study the electric field and examine resonance between waves and geomagnetic field lines. Lastly, we bring our attention to the Alfvén continuum to see if the model agrees with the predictions made by theory.

4.1 Wave Equation

In order to examine the physics of ULF waves, we must define the equation that governs the model to be used. The derivation of the wave equation in field aligned coordinates can be found in Appendix A, which also gives the most general form

of the equation that governs the ULF wave model (Equation A.71). For our results, we are using the model of [Degeling et al., 2011], which slightly modifies the approach taken in Appendix A by considering an exteral current acting as a driver and the use of the Cartesian coordinate system (to be elaborated on further in Section 4.1.1).

4.1.1 Model of [Degeling et al., 2011]

In Appendix A, we obtain the wave equation for the model by using Faraday's law (Equation A.27) and Equation A.28. The equations that we solve differ slightly from those defined in [Degeling et al., 2011]; we introduce a change to Equation A.28 by adding an external current, $\mathbf{J}^{\text{ext}}$, which oscillates harmonically at a frequency in the mHz range. This current acts to excite the waves we are interested in. $\mathbf{J}^{\text{ext}}$ is placed at the magnetopause boundary (to which it is also tangential), perpendicular to the magnetic field (Degeling et al. [2011]). For our purposes, Equation A.28 now reads,

$$\frac{1}{v_A^2}\frac{\partial \mathbf{E}}{\partial t} = (\nabla \times \mathbf{b})_\perp - \frac{(\mu_0 \mathbf{J} \times \mathbf{b}) \times \mathbf{B}}{B^2} + \mu_0 \mathbf{J}^{\text{ext}} \tag{4.1}$$

which is the same as Equation A.28, except with the addition of the source current term. Equation 4.1 is what is used in lieu of Equation A.28 to derive the wave equation.

4.1.2 Solving Equation 4.1

In order to solve a physical problem, we need to have an appropriate geometry. As mentioned, we are using Cartesian coordinates for this problem, with x being positive in the direction of the Sun along the Sun-Earth line, z is perpendicular to the equator (in the direction of the magnetic field), and y is chosen such that we have an orthogonal coordinate system. Defining Earth's magnetic field in the equatorial plane as,

$$\mathbf{B_0} = B_0\,(x, y)\,\hat{\mathbf{z}} \tag{4.2}$$

allows us to write Equation 4.1 as,

$$\left(\frac{\partial^2}{\partial z^2} - \frac{1}{v_A^2}\frac{\partial^2}{\partial t^2}\right)\begin{pmatrix} E_x \\ E_y \end{pmatrix} = \frac{1}{B_0}\begin{pmatrix} -\partial/\partial y \\ \partial/\partial x \end{pmatrix}\left[B_0\left(\frac{\partial E_x}{\partial y} - \frac{\partial E_y}{\partial x}\right)\right] + \mu_0 \frac{\partial}{\partial t}\begin{pmatrix} J_x^{\text{ext}} \\ J_y^{\text{ext}} \end{pmatrix} \tag{4.3}$$

Equation 4.3 is a simplification of the more general form of the wave equation given by Equation A.71. Equation 4.3 uses the Cartesian coordinate system,

whereas Equation A.71 uses the field aligned coordinate system (discussed in Appendix A, Section A.1.1). As the Cartesian coordinate system is an orthogonal coordinate system, the gradient basis vectors defined by Equations A.9 and A.21 equal one when $i = j$ and zero for $i \neq j$. This simplifies the matrix $\mathbf{G}$ (Equation A.67) in Equation A.71 to the identity matrix. Furthermore, the determinant of Equation A.23 will be unity, which means that $\sigma = B_0$ (cf. Equation A.26).

To get our Cartesian coordinates from the field aligned coordinates, we can simply define $\alpha = x$ and $\beta = y$. As well, since γ is our field aligned coordinate and in the box model assumption, the field lines are stretched in the z-direction, we may set $\gamma = z$.

As can be seen on the right hand side of Equation 4.3, there are terms for the electric field, but in Equation A.71, the right hand side only contains information about the magnetic field of the perturbation. We can convert between the two by use of Faraday's law; the specific equation we require is Equation A.65. If we put this definition in Equation A.71, then apply our change of coordinates described in the previous paragraph, we will end up with Equation 4.3 (subject to adding the driving current term, $\mathbf{J}^{\text{ext}}$, to Equation A.28).

In order to further simplify Equation 4.3, we will apply the box model assumptions of [Zhu & Kivelson, 1988]. The box model makes the assumption that all magnetic field lines are straight and terminate on flat conducting surfaces that represent the two ionospheres (north and south). This allows us to simplify the treatment of the shear Alfvén wave eigenfunctions along magnetic field lines (Degeling et al. [2011]).

The box model has the drawbacks that it differs from the actual magnetosphere (since the real magnetosphere is not in the shape of a rectangular box). Furthermore, the box model cannot explain some observational features. Barring the drawbacks, the box model does offer insight into wave coupling (between the MHD fast waves excited by the driver and the shear Alfvén waves on the field line) and is the basis for working towards a full understanding of MHD waves in the magnetosphere (Zhu & Kivelson [1988]).

All field aligned eigenfunctions are decoupled under the box model assumption, thus, there is no way to distinguish toroidal and poloidal wave modes (Degeling et al. [2011]). This permits us to write the electric field as,

$$\mathbf{E} = \mathbf{E}_n(x, y) \cos(k_n z)\, e^{-i\omega t} \tag{4.4}$$

where,

$$k_n = \frac{n\pi}{z_{\text{fl}}}\ ,\ n \in \mathbb{Z} \tag{4.5}$$

where n is an integer and z_{fl} is the length of the field line. By inserting Equation 4.4 into Equation 4.3, this reduces the equation to a coupled pair of elliptic partial

differential equations under the box model assumption,

$$-\left(\frac{1}{v_A^2}\frac{\partial^2}{\partial t^2}+k_n^2\right)\cos\left(k_n z\right)e^{-i\omega t}\begin{pmatrix}E_{nx}\\E_{ny}\end{pmatrix}= \frac{1}{B_0}\begin{pmatrix}-\partial/\partial y\\ \partial/\partial x\end{pmatrix}\left[B_0\left(\frac{\partial E_x}{\partial y}-\frac{\partial E_y}{\partial x}\right)\right]+\mu_0\frac{\partial}{\partial t}\begin{pmatrix}J_x^{\text{ext}}\\J_y^{\text{ext}}\end{pmatrix} \quad (4.6)$$

The pair of equations from Equation 4.6 are solved using the Partial Differential Equation toolbox in MATLAB, by writing Equation 4.6 in the form

$$\mathbf{M}\cdot\frac{\partial^2\mathbf{u}}{\partial t^2}+\mathbf{K}\cdot\mathbf{u}=f \quad (4.7)$$

where $\mathbf{u}$ represents the electric field, f represents the wave driver, and $\mathbf{K}$ and $\mathbf{M}$ are coefficient matrices.

The PDE toolbox creates an unstructured triangular mesh grid in the region of interest for the model (i.e. the magnetospheric boundaries imposed by [Degeling et al., 2011]). In order to solve the elliptic PDEs for the electric field, the toolbox constructs a series of tent functions which are defined on the triangular mesh in order to approximate the weak form (that is, a solution which is not everywhere differentiable (Myint-U & Debnath [2007])) of the PDE using the Galerkin method. This mesh is also automatically refined by the solver, which, as a consequence, results in a higher triangle density along field line resonance surfaces (Degeling et al. [2011]).

A detailed mathematical formalism of the Galerkin method is given in Chapter 14 of [Myint-U & Debnath, 2007].

4.1.3 Previous Work

The derivation of Equation A.71, which is a more general form than those solved in the thesis, has been explored by [Rankin et al., 2006], [Kabin et al., 2007], and [Degeling et al., 2010]. In [Rankin et al., 2006] and [Kabin et al., 2007], the fundamental assumption for the derivation of Equation A.71 was that there was no coupling amongst the field lines (i.e. each field line oscillated independently). Thus, with no fast mode coupling, the right hand side of Equation A.71 is set to zero and the shear Alfvén wave modes are decoupled from the compressional mode. In this approach, each field line oscillates independently at its natural frequency. The solutions for the eigenmodes are obtained using Newton's method, which attempts to find the roots (zeroes) of a function. The initial guess for Equation A.71 is the eigenvalue that is predicted via the WKB approximation.

In [Degeling et al., 2010], the author does not assume that the field lines oscillate independently, and thus, the term on the right hand side of Equation A.71 remains. The wave equation is solved by using the spectral method. The spectral method allows one to write the solutions of a differential equation in terms of basis functions, which are multiplied by amplitude coefficients. The goal is to find the value of the coefficients that satisfies the differential equation, while keeping the error to a minimum.

4.2 Model Profiles and Parameters

4.2.1 Magnetic Field Model

Although we are using the straight magnetic field model (the box model) from [Zhu & Kivelson, 1988], we base it on the formalism presented in [Stern, 1985]. In particular, we use the equatorial projection of the field lines defined in [Stern, 1985]. [Stern, 1985] is based on Earth's magnetic field being contained within a conducting paraboloid shell, which represents the magnetopause. Inside this shell, the condition is imposed that the magnetic field is current free, such that from Ampère's law, we have,

$$\nabla \times \mathbf{B} = 0 \tag{4.8}$$

From vector calculus, when the curl of a vector is zero, that same vector may be written as the negative gradient of a scalar potential. Thus, as in [Stern, 1985], we can write the magnetic field as,

$$\mathbf{B} = -\nabla\gamma \tag{4.9}$$

We further impose the condition, from Maxwell's equations, that the divergence of the magnetic field is zero (i.e. magnetic field lines are closed). Applying the divergence operator to Equation 4.9 leaves us with,

$$\nabla^2\gamma = 0 \tag{4.10}$$

This is just Laplace's equation, which can be solved, given appropriate boundary conditions.

Equation 4.10 is solved using a parabolic coordinate (λ, μ, ψ) system, which is based off the solar magnetospheric Cartesian coordinates, given by,

$$\begin{cases} \lambda^2 = r + (x - x_0) \\ \mu^2 = r - (x - x_0) \\ \tan\psi = z/y \end{cases} \tag{4.11}$$

where the origin of this coordinate system is given by the point $(x_0, 0, 0)$ (Stern [1985]). One of the boundary conditions is that the normal component of the total magnetic field, $\mathbf{B}$, should be cancelled by the surface currents flowing along the magnetospheric boundary, which ensures no magnetic flux crosses the magnetopause boundary (Stern [1985]). This is given by,

$$\frac{\partial \gamma_{MP}}{\partial \lambda} = -\frac{\partial \gamma_D}{\partial \lambda} \text{ at } \lambda = \lambda_0 \tag{4.12}$$

where γ_{MP} and γ_D will be defined shortly.

The derivation process is long and thus, it will only be summarized here, but all the details are available in [Stern, 1985].

The scalar potential, γ, in Equations 4.9 and 4.10, is a combination of the scalar potential derived from the magnetic field of Earth and of the scalar potential derived from the surface currents running along the magnetopause boundary, such that,

$$\gamma = \gamma_D + \gamma_{MP} \tag{4.13}$$

The dipole magnetic field of Earth is given by,

$$B_D = \frac{B_E}{L^3} \tag{4.14}$$

and thus, we can easily derive γ_D. However, the magnetic field needs to be derived due to the surface currents from γ_{MP}.

From [Stern, 1985], the scalar potential due to the magnetopause currents is given by,

$$\gamma_{MP} = \sin\phi \sum_n a_n J_1(k_n \mu) I_1(k_n \lambda) \tag{4.15}$$

where ϕ is the azimuthal angle around the x-axis, J_1 is the first order Bessel function, and I_1 is the first order modified Bessel function. The variable k_n satisfies the following relationship,

$$J_1(k_n A) = 0 \tag{4.16}$$

where A is a scaling parameter (Stern [1985]). The coefficients a_n are determined by applying the boundary condition given by Equation 4.12. This allows us to get the magnetic field given by the magnetopause currents,

$$\mathbf{B_{MP}} = -\nabla \gamma_{MP} = -\left(\frac{\partial \gamma_{MP}}{\partial \lambda} \nabla \lambda + \frac{\partial \gamma_{MP}}{\partial \mu} \nabla \mu + \frac{\partial \gamma_{MP}}{\partial \psi} \nabla \psi \right) \tag{4.17}$$

where the right-most side is just an expansion of the scalar potential gradient using the chain rule.

Equation 4.12 gives the boundary condition required inside the magnetopause. Outside the magnetopause, Equation 4.12 reads,

$$\frac{\partial \gamma_{MP}}{\partial \lambda} = -\frac{\partial \gamma_{IMF}}{\partial \lambda} \text{ at } \lambda = \lambda_0 \tag{4.18}$$

In order to get γ_{IMF}, we treat the interplanetary magnetic field as being constant and in the z direction. This allows us to write,

$$\gamma_{IMF} = z \tag{4.19}$$

or, using Equation 4.11,

$$\gamma_{IMF} = \lambda \mu \sin \phi \tag{4.20}$$

This permits us to write the total magnetic field, $\mathbf{B}$, as

$$\mathbf{B} = \sigma \nabla \gamma_D + (1 - \sigma) \nabla \gamma_{IMF} \tag{4.21}$$

where σ is a function that varies smoothly over a width set at 0.25 R_E (Degeling et al. [2011]) from zero to one, in order to match the magnetic field inside and outside the magnetopause. It should be noted that Equation 4.21 is the equatorial projection of the field lines in [Stern, 1985].

4.2.2 Model Magnetosphere

One of the main improvements of the model described in [Degeling et al., 2011] is the shape of the magnetopause boundary. In [Degeling et al., 2010], the magnetopause boundary was given by a closed oval shape in the equatorial plane. The drawback to this structure is that it only resembles the magnetopause close to local noon. In the 2011 model, the magnetopause geometry is given such that wave solutions are bounded only on the dayside and along the flanks, whereas on the nightside, they are unbounded. An artificial boundary is inserted on the nightside in order to contain the region of interest. In order to minimize reflections from this boundary, the wave solutions are damped outside the boundary.

Figure 4.1 shows the shape of the magnetopause being used in the model (the region of interest), as well as the unstructured triangular mesh grid used to calculate the fields. The magnetopause boundary is defined from [Stern, 1985] on the paraboloid $\lambda = \lambda_0$, which is subject to the boundary conditions given by

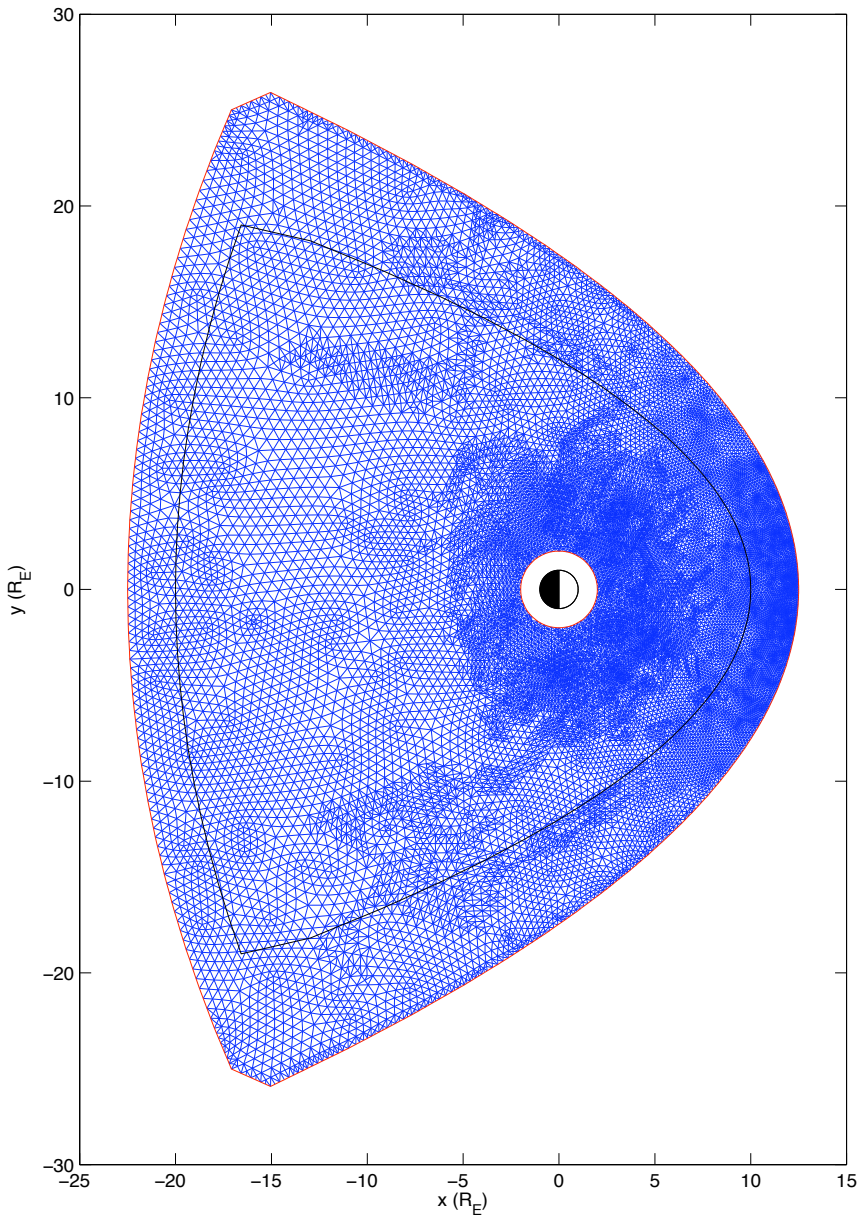

Figure 4.1: Structure of the model magnetopause with the unstructured triangular mesh grid used to calculate the solutions to the wave equation.

Equation 4.12 and 4.18. Furthermore, other parameters that define Figure 4.1 can be found in Table 4.1.

Table 4.1: Parameters that define the magnetopause boundary in Figure 4.1 (all parameters are measured from the center of Earth).

Parameter	Value
sunward distance to magnetopause, x_{MP}	10 R_E
dawn/dusk distance of magnetopause, y_{MP}	15 R_E
distance to paraboloid focus, $x_0 = x_{MP} - y_{MP}^2/(4x_{MP})$	4.375 R_E
paraboloid defining the magnetopause boundary, $\lambda_0^2 = 2(x_{MP} - x_0)$	11.25 R_E
maximum value of $\lvert x\rvert$ on the nightside	20 R_E

The solution to Laplace's equation (Equation 4.10) is given by,

$$\gamma = (A_m \sin m\phi + B_m \cos m\phi) J_m (k\mu) [a_m (k) I_m (k\lambda) + b_m (k) K_m (k\lambda)] \quad (4.22)$$

where m takes only discrete positive values, k varies continuously, J_m is the Bessel function of the first kind, I_m and K_m are the modified Bessel functions of the first and second kind, A_m, B_m, a_m, and b_m are coefficients determined through matching the solution of Equation 4.22 via the boundary conditions in Equation 4.12 and 4.18 inside and outside the magnetosphere, and μ and λ are defined in Equation 4.11. For the magnetosphere boundary defined by [Stern, 1985], the conditions required are that for interior solutions (i.e. $0 < \lambda < \lambda_0$), all values of $b_m (k)$ must be zero; for exterior solutions (i.e. $\lambda > \lambda_0$), all values of $a_m (k)$ must be zero.

The computational domain for the model also has an artificial boundary on the nightside, which confines our region of interest. Waves outside the nightside boundary end up being artificially damped; this minimizes reflections from the numerical outer boundary. The driving frequency, ω, is defined as,

$$\omega = \omega_R + i\omega_I \quad (4.23)$$

where the inclusion of the imaginary part in Equation 4.23 allows for wave damping. For strong damping (outside the region of interest), we set $\omega_I/\omega_R \gg 1$. Inside the magnetosphere, near the artificial boundary, we set $\omega_I/\omega_R = 0.1$ to mimic finite ionospheric Pedersen conductivity (Degeling et al. [2011]).

4.2.3 Density Profile

In the models described by [Rankin et al., 2006] and [Kabin et al., 2007], a simple density profile is given that scales as r^{-4}, which is multiplied by the equatorial

density (a constant). The density profile in [Degeling et al., 2011] takes the form given in [Degeling et al., 2010],

$$\rho = \rho_{eq}(R)\left(\frac{r}{R}\right)^{-\Lambda} \tag{4.24}$$

where r is defined as the standard radial distance to a field line, Λ is the plasma mass index (Menk et al. [1999]), and ρ_{eq} is the equatorial density profile, given by,

$$\rho_{eq}(R) = \rho_0\left(\frac{R}{R_0}\right)^{-\kappa} \tag{4.25}$$

where the constants ρ_0 and R_0, along with the scaling power, κ, are constrained by data. The relevant data for the density profiles inside and outside the plasmapause are given in Table 4.2.

Table 4.2: Plasmapause density profiles from [Degeling et al., 2011].

	Inside	Outside
L	3	6
κ	2	1
ρ_0 [amu/cm^3]	2000	150

In order to join the outside and inside density profiles, the equatorial density profile is written as,

$$\rho_{eq} = \rho_1^{1-\Omega}\rho_2^{\Omega} \tag{4.26}$$

where ρ_1 and ρ_2 are the densities inside and outside the plasmapause (and have the form of the profile in Equation 4.25) and Ω is a function that varies smoothly from zero to unity in the region of the plasmapause width (Degeling et al. [2010]). This allows for the smooth transition of the density profile outside the plasmapause to the density profile inside the plasmapause. Outside the plasmapause, $\Omega = 1$; inside the plasmapause, $\Omega = 0$.

Figure 4.2 shows the density profile ($\log_{10}\rho$) of the ULF wave model of [Degeling et al., 2011].

4.2.4 Wave Driver

On the rightmost side of Equation 4.3, the term $\mathbf{J}^{\text{ext}}$ represents the external current placed on the magnetopause boundary that drives ULF waves in the magnetosphere. This driving term is represented by,

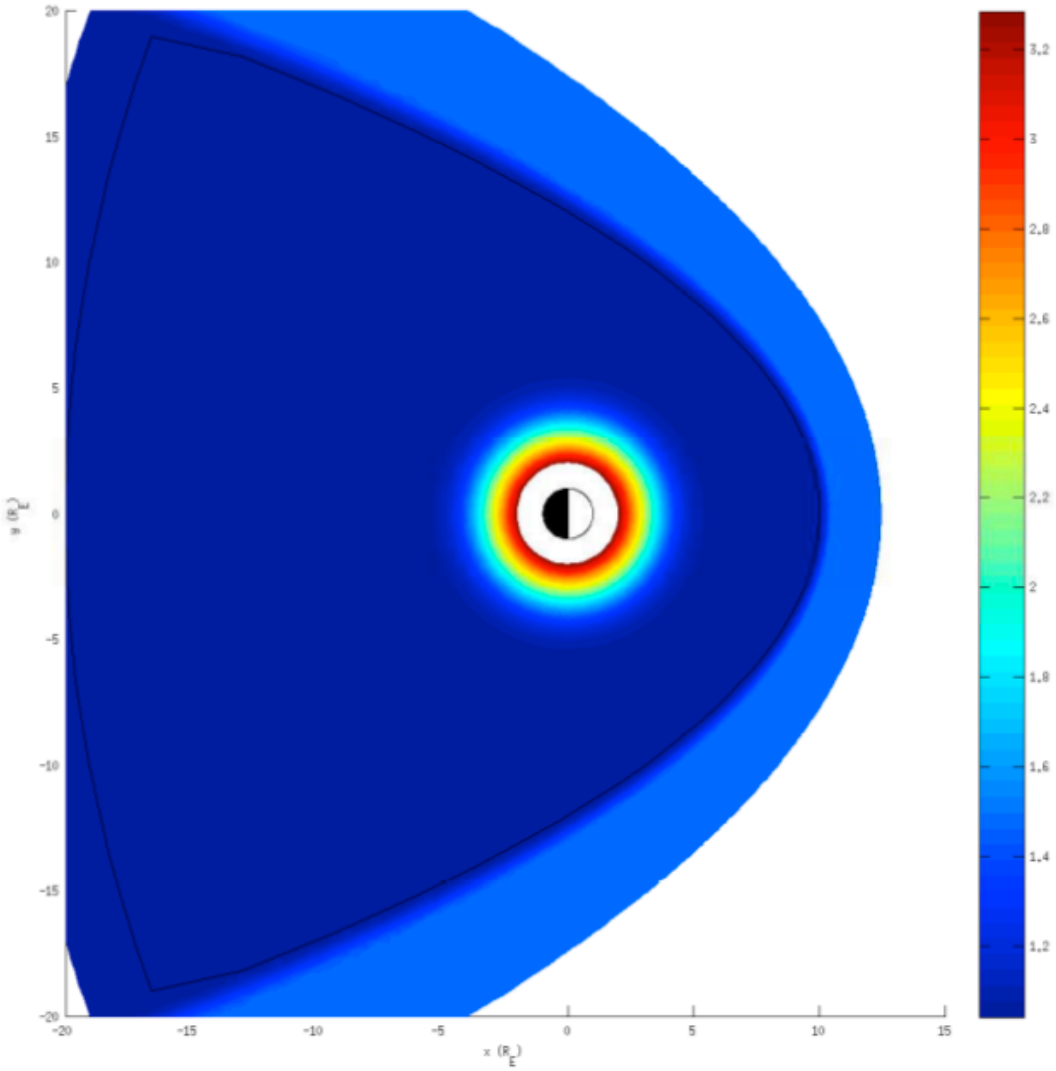

Figure 4.2: Density profile ($\log_{10} \rho$) from the ULF wave model of [Degeling et al., 2011].

$$\mu_0 \frac{\partial \mathbf{J}^{\text{ext}}}{\partial t} = \Theta_0 \frac{t}{\tau_1} e^{-t/\tau_2} e^{-i\omega t} \tag{4.27}$$

where $\tau_1 = 21.2$ ms, $\tau_2 = 25$ s, and Θ_0 is a function set to unity to give the dimensionally correct units of the driver.

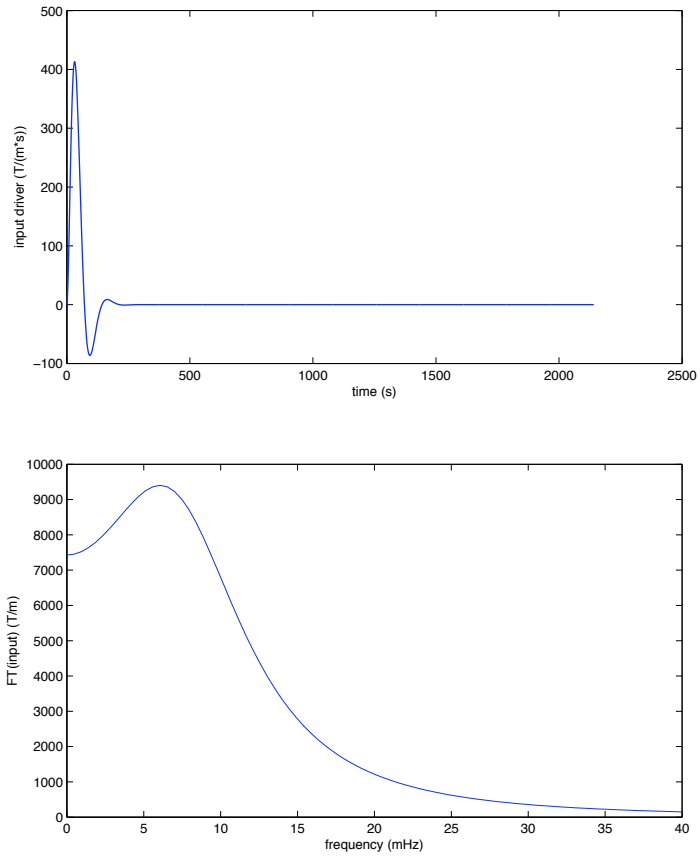

Figure 4.3: Top panel: wave driver input from the ULF wave equation. Bottom panel: Fourier transform of the wave driver input, with a peak frequency at $\nu = 7$ mHz.

Figure 4.3 shows the ULF wave driver and its Fourier transform, which peaks at $\nu = 7$ mHz. It should be noted that the shape of the ULF wave driver is independent of solar wind speed.

4.3 Results from the ULF Wave Model

The interactions that we are studying in the magnetosphere can be classified as wave-particle interactions that consist of two parts: the wave component and the particle component. In this chapter, we seek to develop a greater understanding of the wave component of the wave-particle interactions. In order to complete this, we will examine some results from the wave model by looking at the effects in the magnetosphere due to the presence of MHD waves. In Chapter 5, we will investigate the particle component of the wave-particle interactions by using the outputs from the ULF wave model to trace particles in the outer radiation belt in order to examine transport.

4.3.1 Electric Fields in the Equatorial Plane

The first set of results we present show how the radial and azimuthal electric fields respond to the pressure pulse sending waves through the magnetosphere. We can analyze this for three different solar wind speeds: v_{SW} = 300 km/s, 700 km/s, and 1,000 km/s, the rationale being that these correspond to slow, moderate, and fast solar wind speeds respectively.

Figures 4.4 and 4.5 shows the evolution of the radial and electric fields over the course of the model run when the solar wind speed is 300 km/s. Figures 4.6 and 4.7 shows the evolution of the radial and electric fields over the course of the model run when the solar wind speed is 700 km/s. Figures 4.8 and 4.9 shows the evolution of the radial and electric fields over the course of the model run when the solar wind speed is 1,000 km/s.

For the time evolution of the radial electric field in Figures 4.4, 4.6, and 4.8, we can see the same general trend occurring. At $t = 0$, we can see the beginning of wave activity at the magnetopause boundary, as this is when the driver begins ULF wave generation. As time evolves, we can see the presence of field line resonances (and hence, the heightened amplitude of E_r) where the natural frequency of the field line matches the frequency of the traveling fast mode wave. Eventually, in the vicinity of the magnetopause, the amplitude of E_r begins to decrease, as the waves have passed through and are no longer causing excitations; in fact, we can see the waves moving down the flanks of the magnetopause. Near the end of the time of the model run, we can see the field lines that were excited at the start now have decreasing amplitude, as the wave has passed and is no longer exciting the field line.

For the time evolution in the azimuthal electric fields in Figures 4.5, 4.7, and 4.9, we also see common trends. At $t = 0$, E_ϕ is zero (no excitation in the azimuthal direction), even though there is a perturbation at the magnetopause due to the wave driver, $\mathbf{J}^{\text{ext}}$. Again, as time evolves, we see a strong peak in the azimuthal

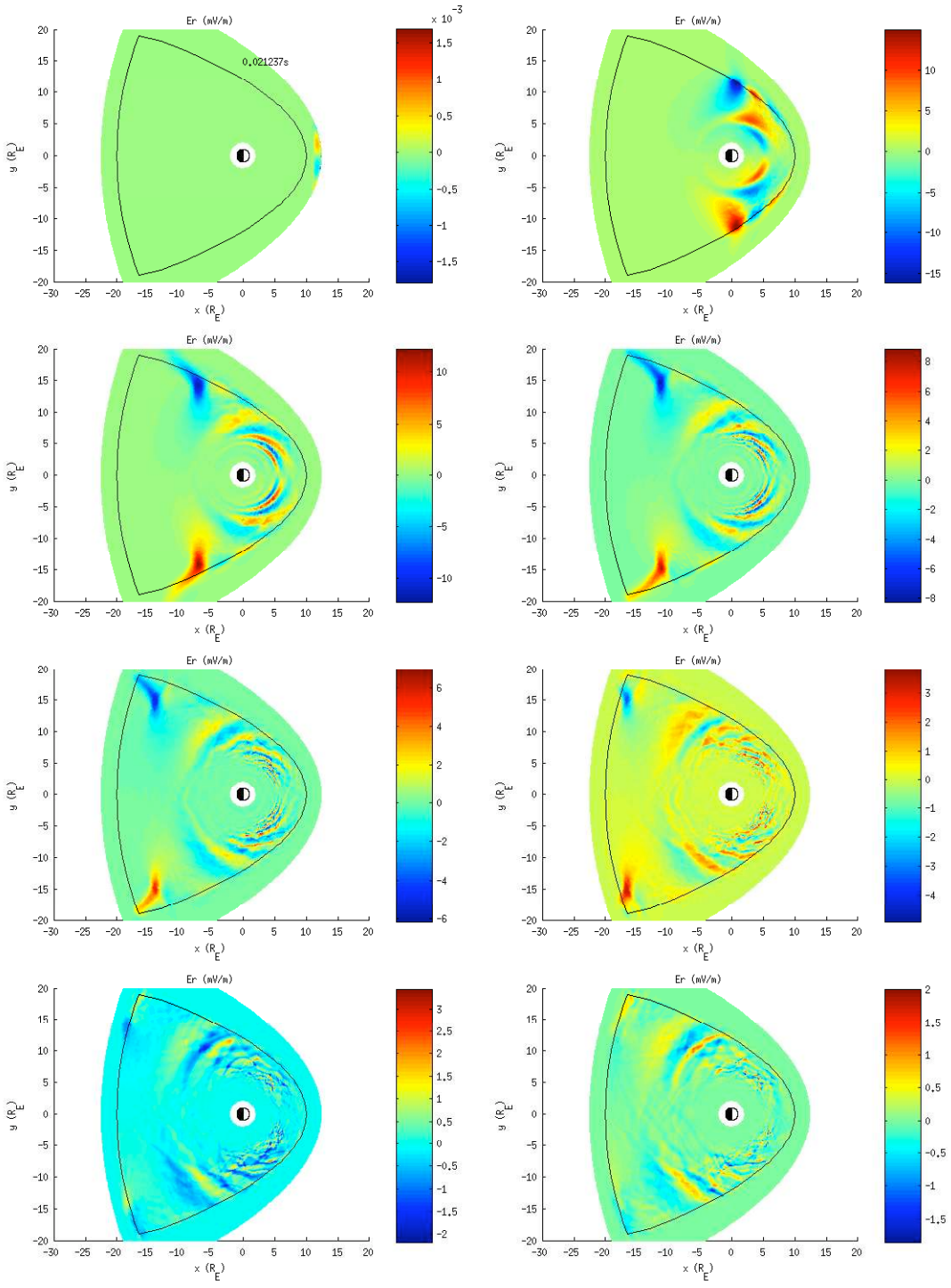

Figure 4.4: Time evolution of the radial component of the electric field for $v_{SW} = 300$ km/s.

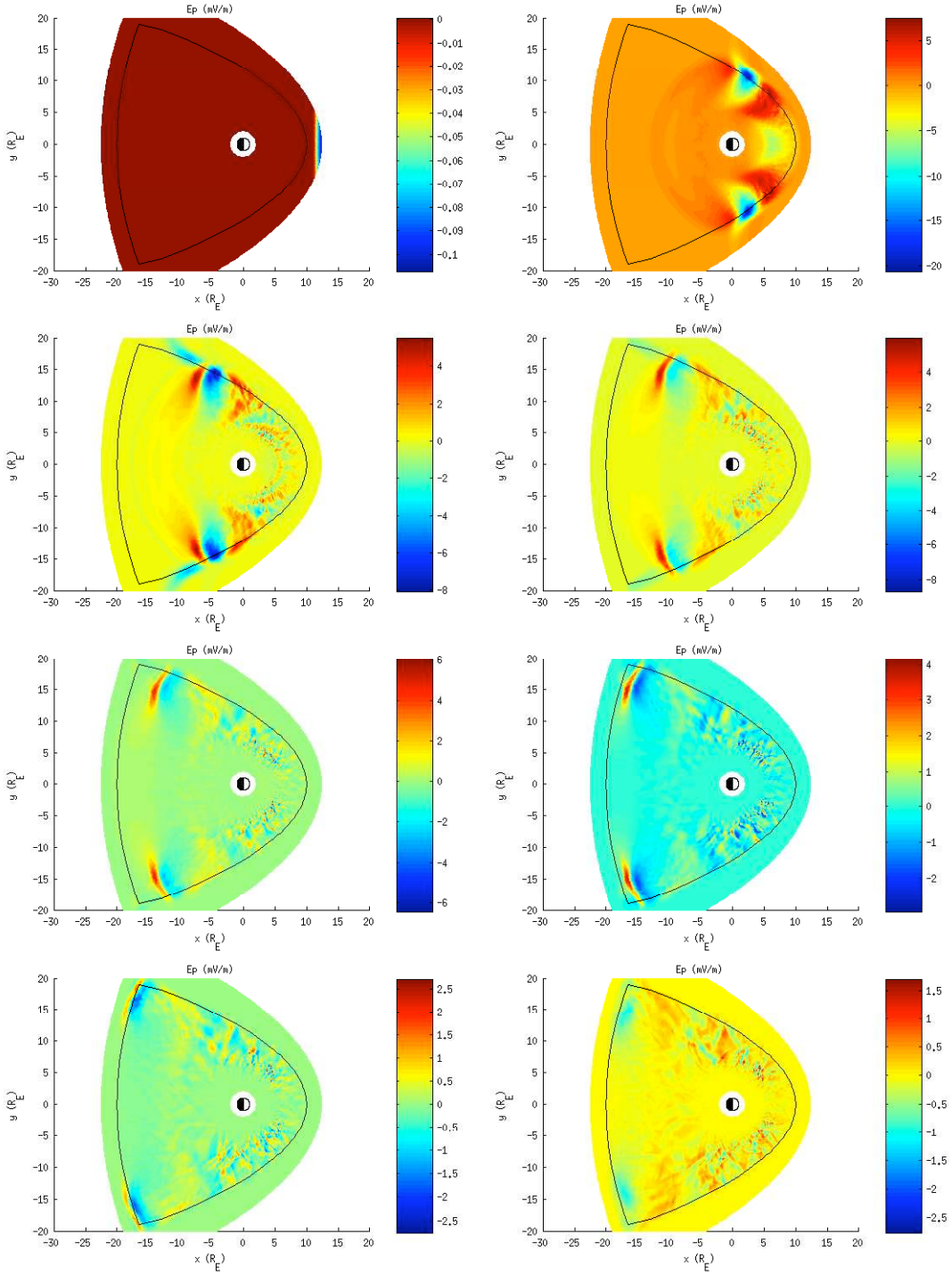

Figure 4.5: Time evolution of the azimuthal component of the electric field for $v_{SW} = 300$ km/s.

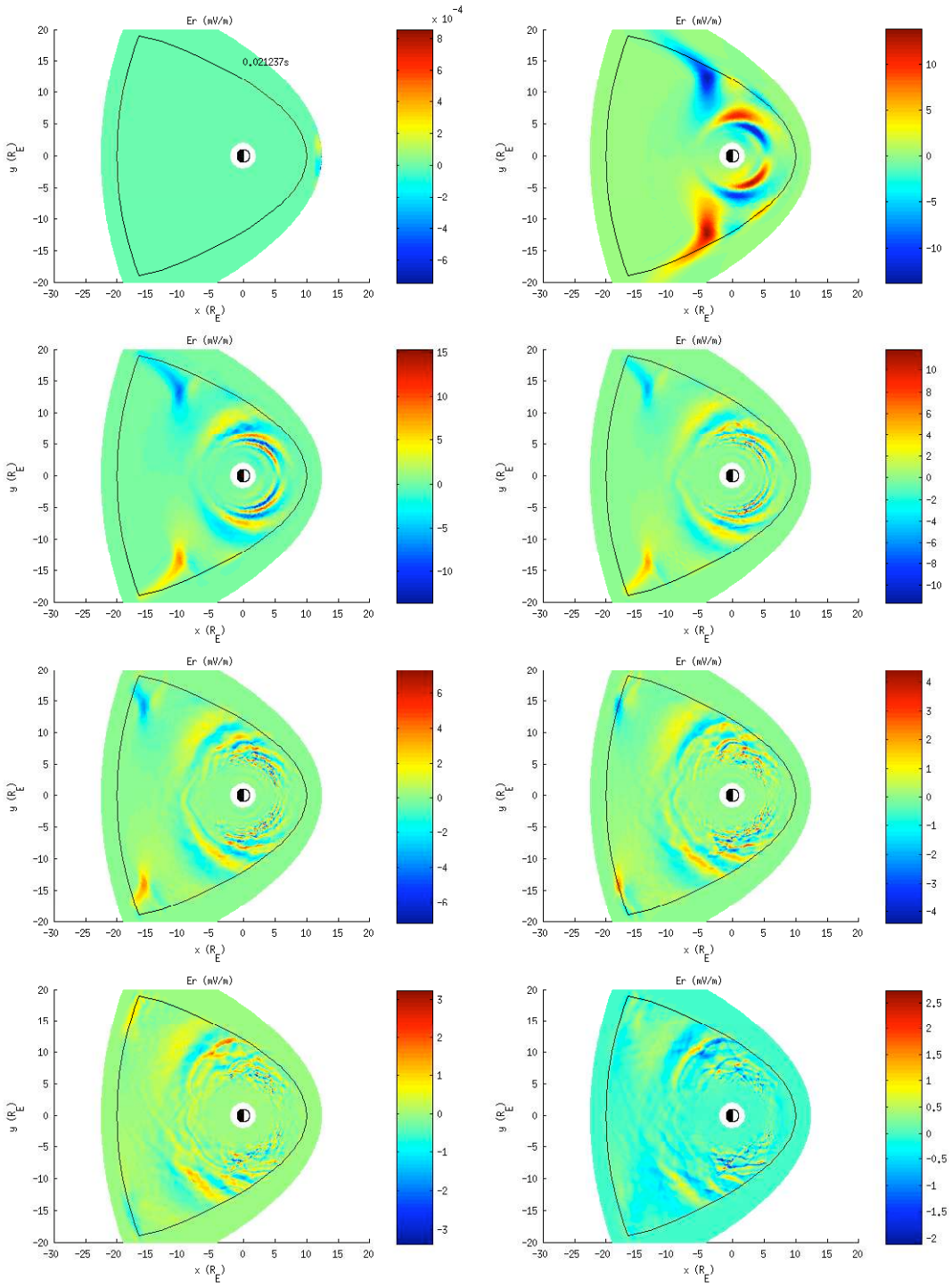

Figure 4.6: Time evolution of the radial component of the electric field for $v_{SW} = 700$ km/s.

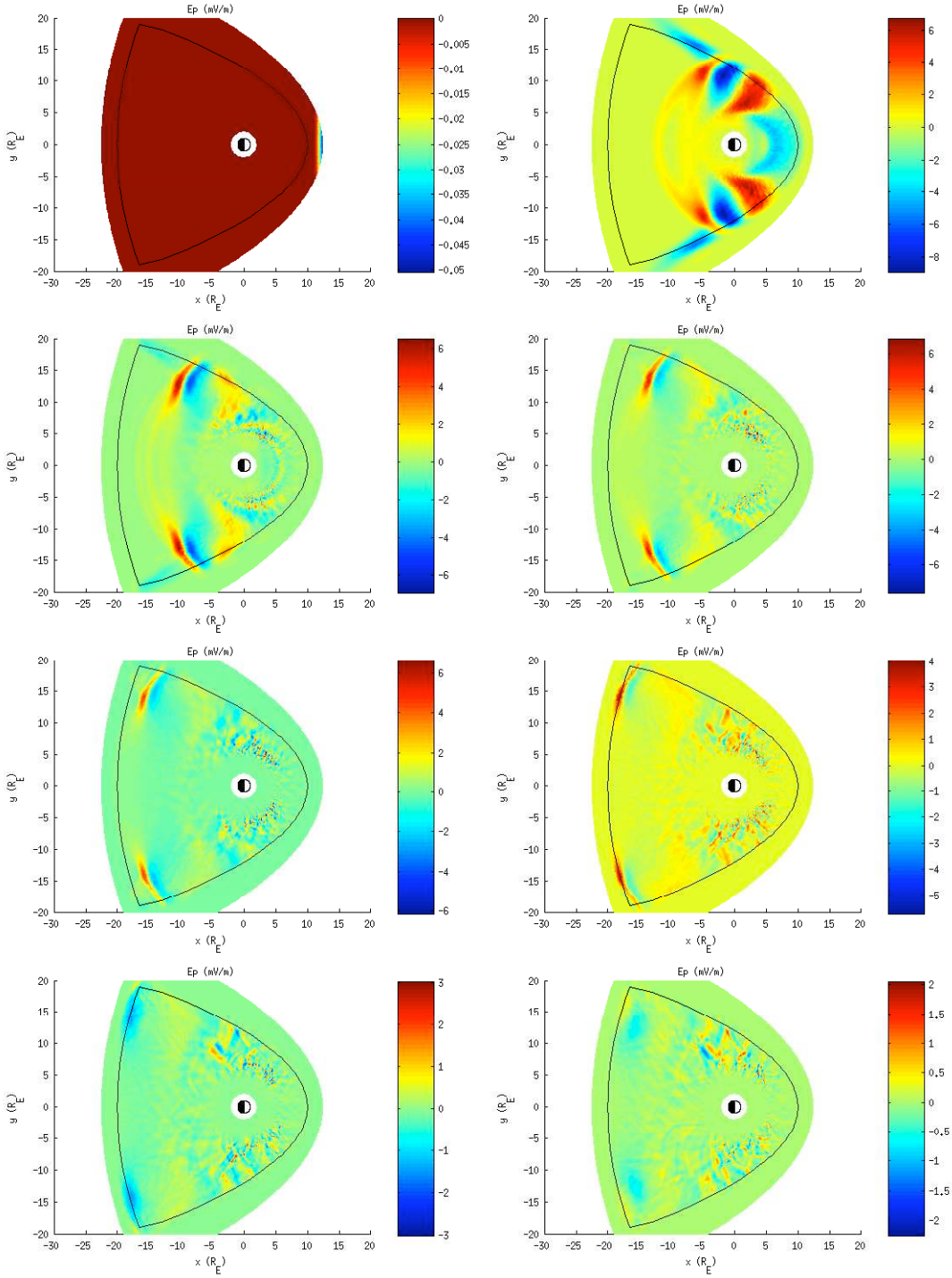

Figure 4.7: Time evolution of the azimuthal component of the electric field for $v_{SW} = 700$ km/s.

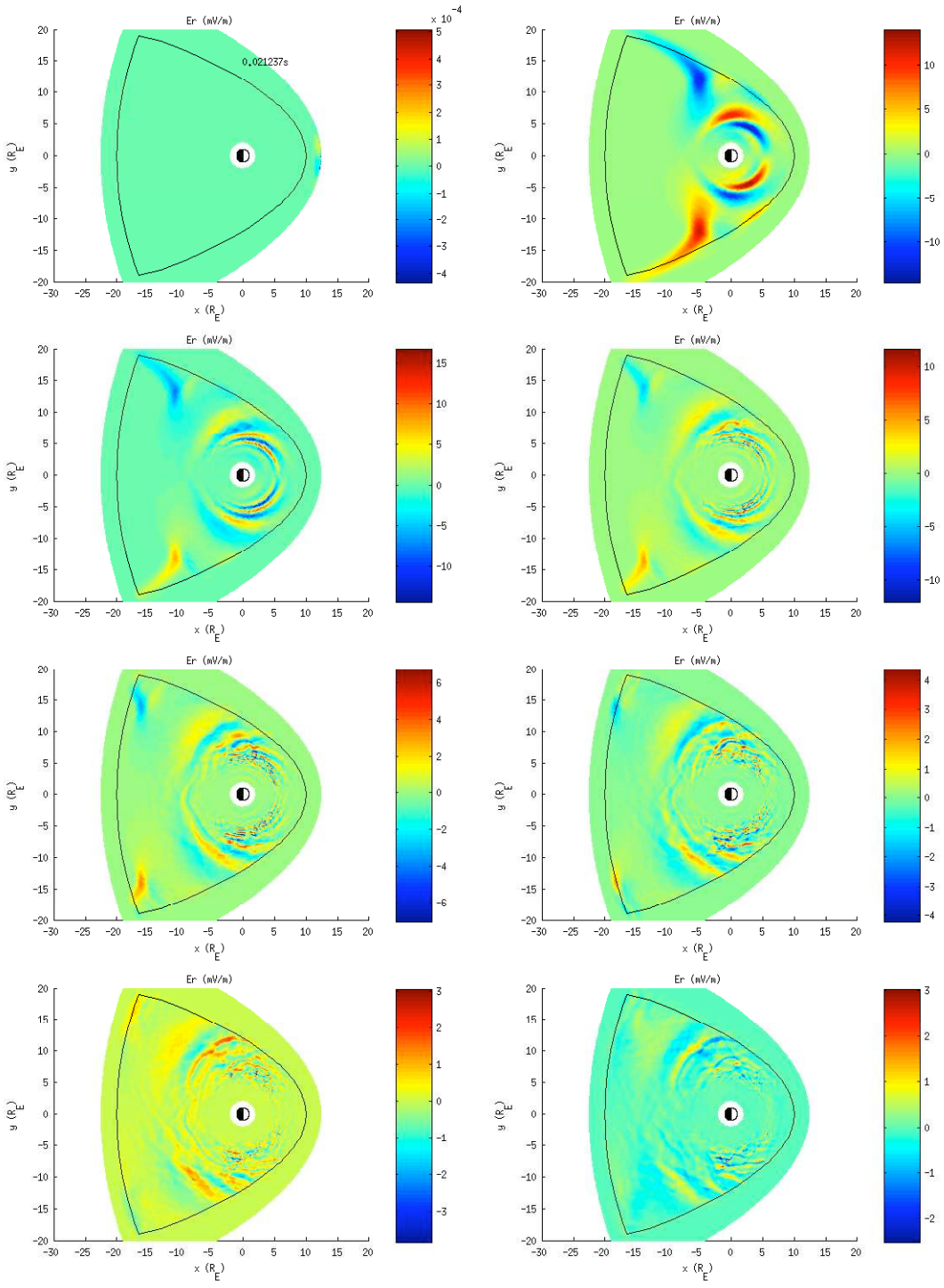

Figure 4.8: Time evolution of the radial component of the electric field for $v_{SW} =$ 1,000 km/s.

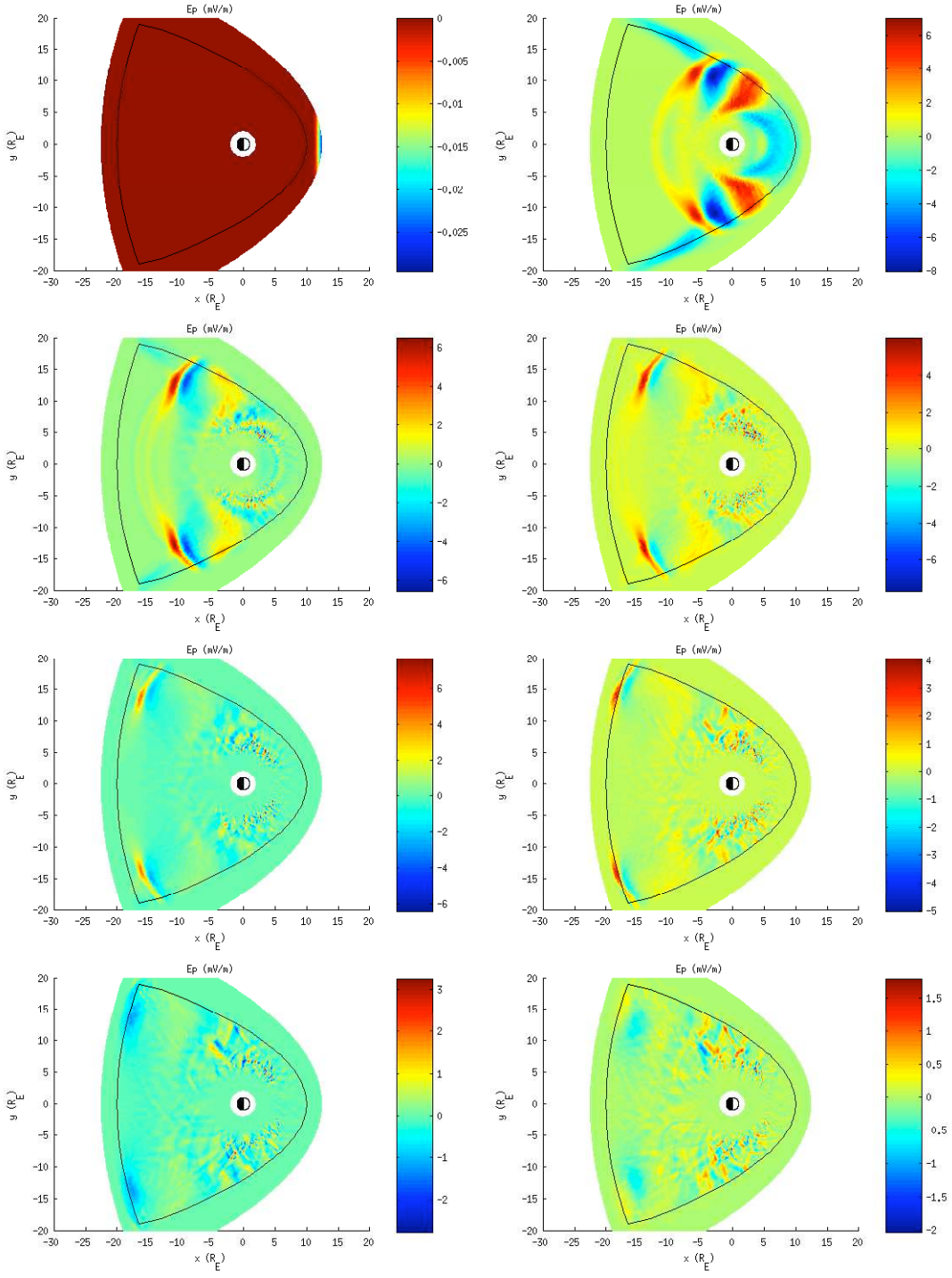

Figure 4.9: Time evolution of the azimuthal component of the electric field for v_{SW} = 1,000 km/s.

electric field, which begins to dampen away as the waves move past; like with the radial case, we can see the wave moving along the flanks, causing changes in the amplitude of E_ϕ.

It is interesting to note that the waves travelling along the flanks of the magnetopause boundary show a resemblance to the Kelvin-Helmholtz (K-H) instability. However, the model of [Degeling et al., 2011] does not contain any physics related to shear flow (which we require for the K-H instability). Instead, these waves are due to the focusing of wave power along the semi-reflective flanks of the magnetopause (Degeling et al. [2011]).

In Figures 4.4, 4.5, 4.6, 4.7, 4.8, and 4.9, the evolution of time runs from left to right and the panels represent equal spacing in time from $t = 0$ (top left panel) to $t_{\max} = 2,137.4$ seconds (bottom right panel).

4.3.2 Electric and Magnetic Field Time Series with varying MLT

From the model, we can also observe the perturbations of the radial and azimuthal electric fields (E_r and E_ϕ), as well as the perturbation in the magnetic field, b_z, as a function of time for varying solar wind speeds. The plots will examine these perturbations at $L = 4.4$ and $L = 6.6$ at varying positions of magnetic local time (MLT). For MLT, zero correponds to midnight and MLT 12 corresponds to noon (moving in the counterclockwise direction).

In Figure 4.10, we examine the perturbations which occur at midnight and noon (MLT 0 and 12, respectively). Comparing the perturbations of b_z at midnight with those at noon, we see those at noon are much stronger (as well, electric field components peak at higher amplitudes at noon than at midnight). The reason for this is that the driver is along the magnetopause boundary and hence, MLT 12 is closer to the wave source than MLT 0. This is also the same reason that the perturbations are stronger for $L = 6.6$ than for $L = 4.4$, because at 6.6, this location is closer to the driver.

In Figure 4.10, inspection of b_z reveals that after the jump in amplitude and some small perturbations, it levels off at a new state. This is a consequence of the compression of the magnetosphere due to the solar wind pressure; when the magnetosphere is compressed, it also compresses the plasma inside the cavity, which alters the magnetic field. Hence, after the pulse passes through, the magnetic field reaches a new equilibrium state, which is different from that of the pre-compression state.

In Figure 4.11, we can see the same trends as those in Figure 4.10. At points closer to the magnetopause (and hence, the location of the wave driver), the perturbation is much stronger than at those points further away from the driver.

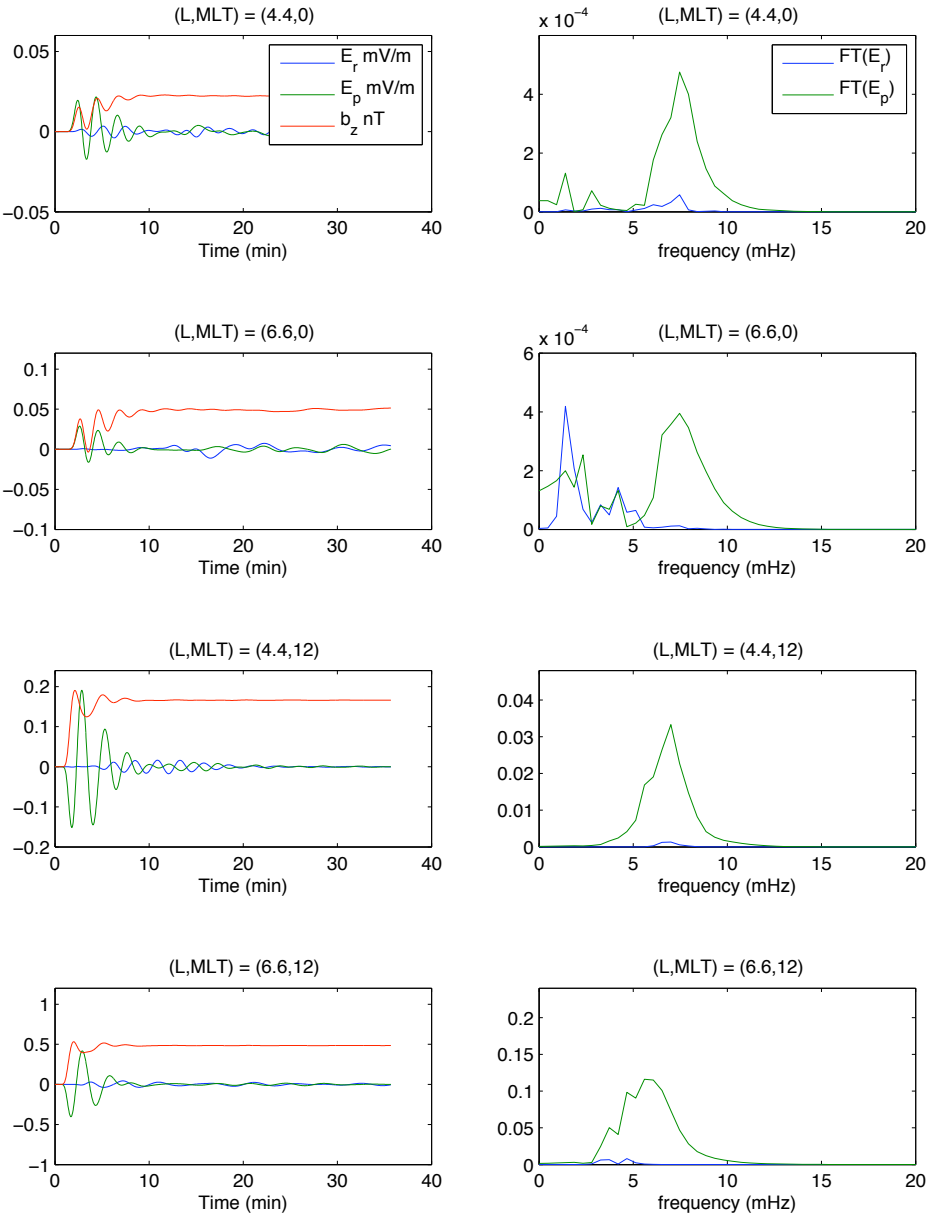

Figure 4.10: Left column: Electric and magnetic field perturbations at MLT 0 and 12. Right column: Fourier transfom of the electric field perturbations. $v_{SW} = 300$ km/s.

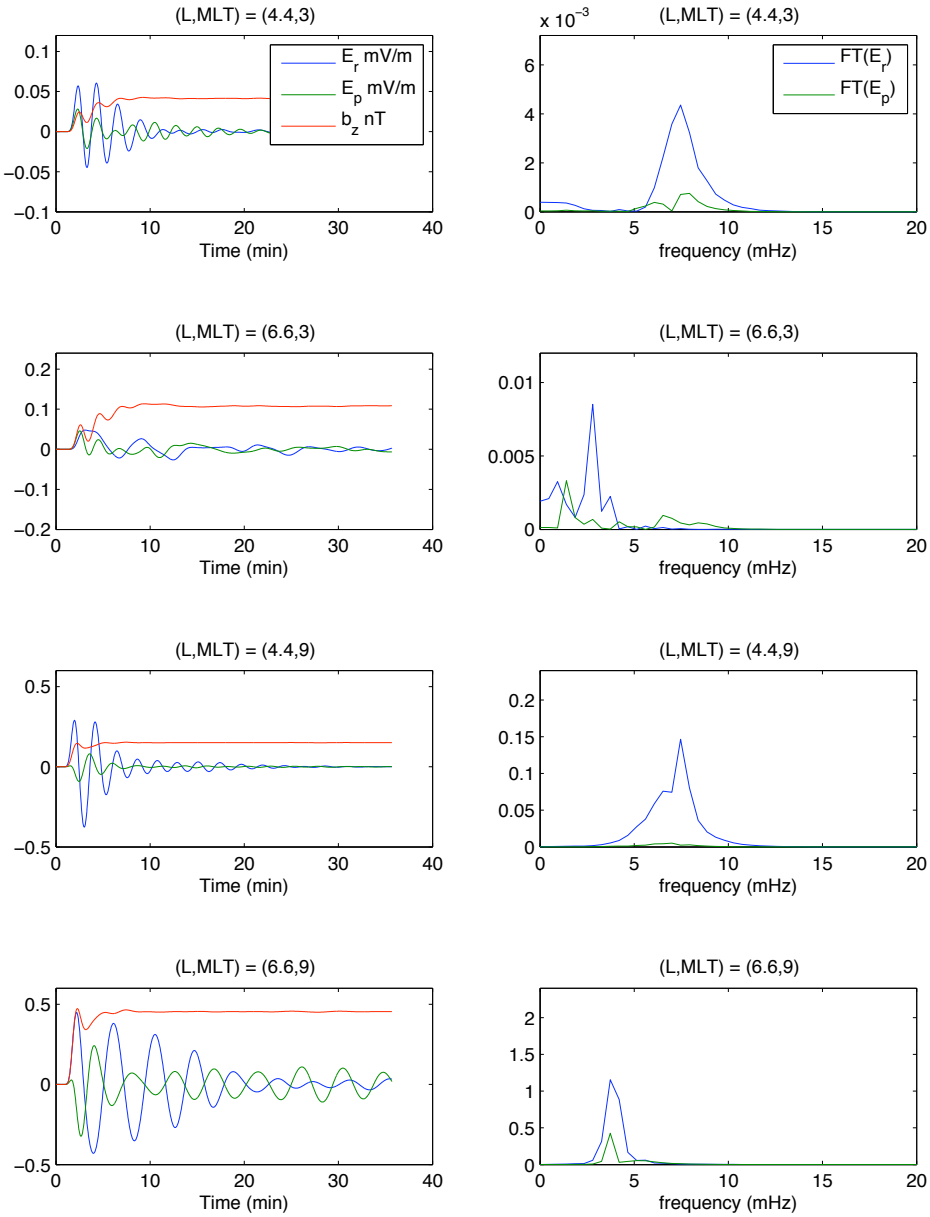

Figure 4.11: Left column: Electric and magnetic field perturbations at MLT 3 and 9. Right column: Fourier transfom of the electric field perturbations. $v_{SW} = 300$ km/s.

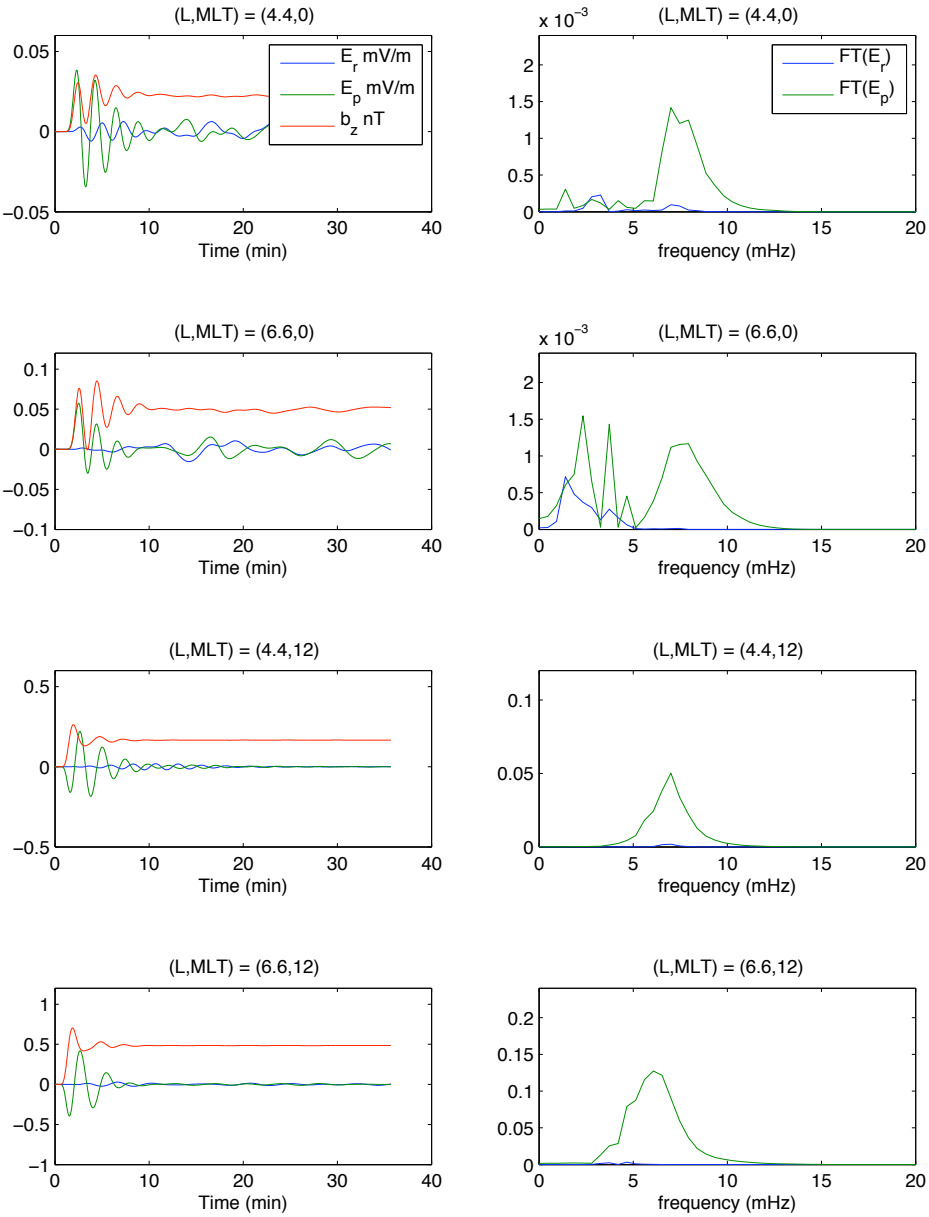

Figure 4.12: Left column: Electric and magnetic field perturbations at MLT 0 and 12. Right column: Fourier transfom of the electric field perturbations. $v_{SW} = 700$ km/s.

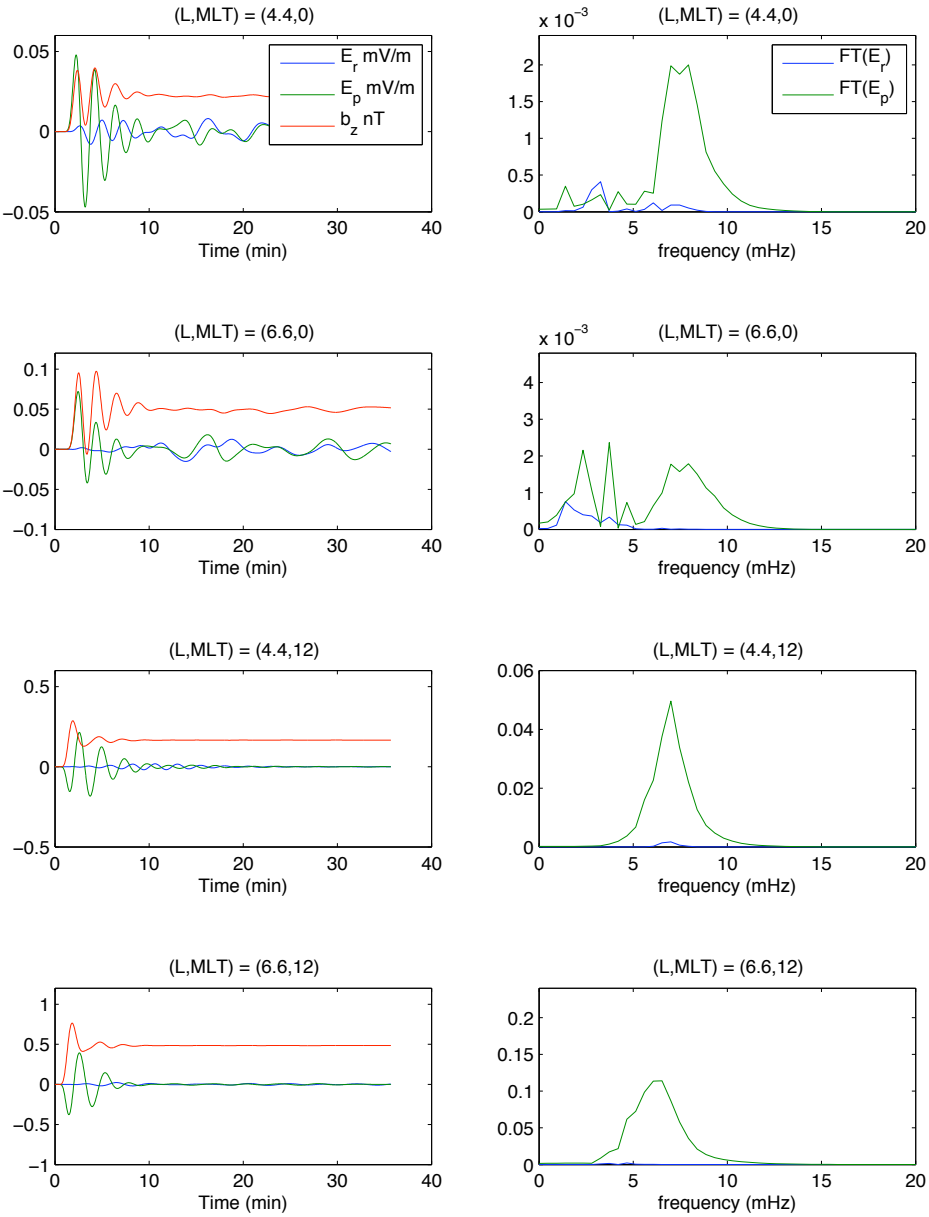

Figure 4.13: Left column: Electric and magnetic field perturbations at MLT 0 and 12. Right column: Fourier transfom of the electric field perturbations. $v_{SW} =$ 1,000 km/s.

In Figures 4.12 and 4.13, we increase the solar wind speed to 700 km/s and 1,000 km/s respectively. As with Figure 4.10, we see the trend that closer to the magnetopause, on the day side, the perturbations are much stronger than those on the night side. Furthermore, as we increase the solar wind speed, we notice that the amplitude of the perturbations also increases (since solar wind dynamic pressure is proportional to the square of its velocity).

4.3.3 Alfvén Continuum

Lastly, we can inspect the plots of the Alfvén continuum, which plots the peak in frequency from the Fourier transform of the radial component of the electric field perturbations as a function of L-shell.

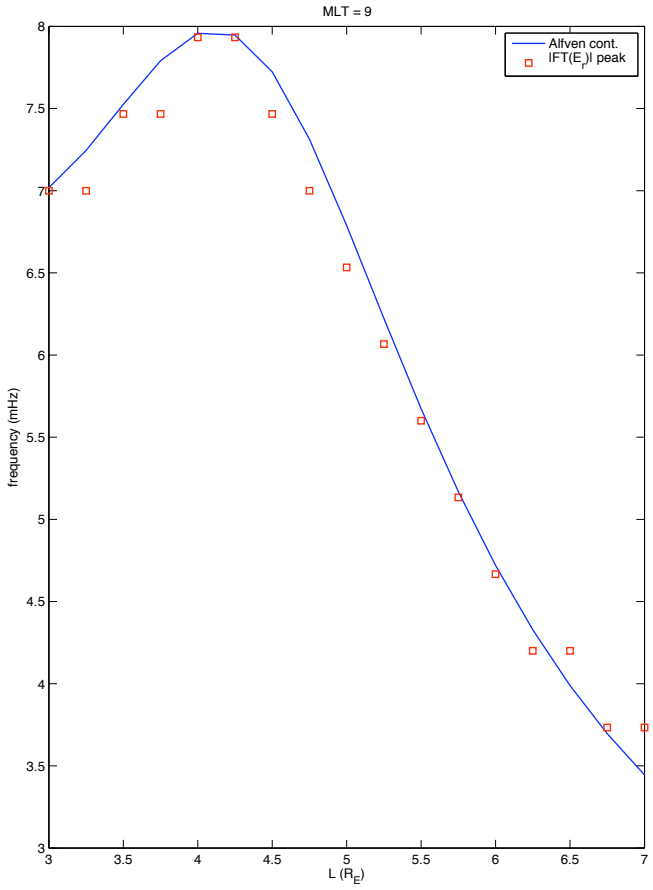

Figure 4.14: Alfvén continuum at MLT 9 for a solar wind speed of 300 km/s.

Our interest in choosing the location of MLT 9 is from observing the plots of the radial electric field in the equatorial plane. As one examines the time evolution of the electric field in the equatorial plane, a strong indication of a field line resonance in the region of MLT 9 (and MLT 15) can be seen and since this is of particular interest to us, this is where we would like to verify the agreement of the model with theory.

The model calculates the peak in frequency for the radial component of the electric field (the squares in Figures 4.14, 4.15, and 4.16), which is compared to a theoretical value (the solid curve in Figures 4.14, 4.15, and 4.16), which is given by,

$$\nu_A = \frac{1}{2\pi} k_z v_A \tag{4.28}$$

which comes from Equation 3.22 (with $k_\parallel = k_z$, as we already specificied in the box model, z is the direction of our magnetic field line).

By examining Figures 4.14, 4.15, and 4.16, which each correspond to solar wind speeds of 300 km/s, 700 km/s, and 1,000 km/s respectively, we can see that there is agreement between the model and theory. This gives us confidence in using the model of [Degeling et al., 2011] to do further investigations of radiation belt physics.

As a note, there are some points in Figures 4.14, 4.15, and 4.16 where two successive squares have the same value of frequency. This is not an error in the model, but rather, it has to do with the resolution of the frequency (cf. Section 3.1.3). If we increase the number of time points in the model, this will increase the resolution in frequency. However, this also increases the time the model runs, and thus, we require a balance to be struck between acceptable frequency resolution and the time the model takes to run.

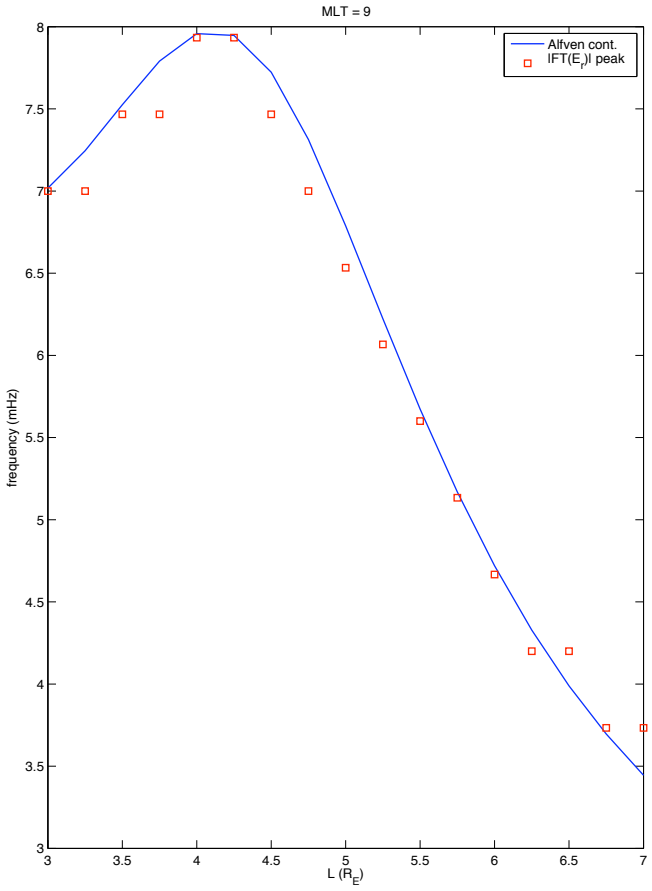

Figure 4.15: Alfvén continuum at MLT 9 for a solar wind speed of 700 km/s.

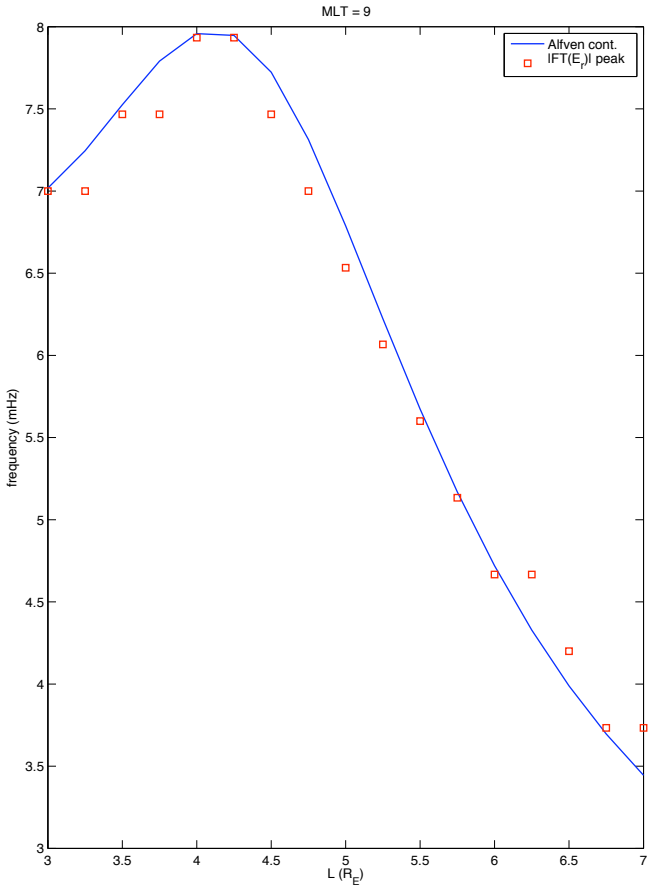

Figure 4.16: Alfvén continuum at MLT 9 for a solar wind speed of 1,000 km/s.

4.4 Afterword

We have managed to cover the fundamental aspects of the ULF wave model being used in this project. We have a good understanding of how the equation that governs the model was derived, as well as how many of the model profiles and parameters were obtained. We were also able to investigate the effect of the waves generated by an external current driver along the magnetopause boundary, examining the resonant interaction between the magnetic field lines and the waves themselves. Lastly, looking at the agreement (which is quite good) between the theoretical prediction of the Alfvén continuum (Equation 4.28) and that given by the model gives us confidence in our model, such that we can proceed with the particle aspect of this project.

It is now time to take the outputs from the ULF wave model and look at radial transport in the outer radiation belt in response to the MHD waves we have generated.

Chapter 5

Particle Transport

The remaining part of the project involves analyzing the effect of ULF waves on electron transport in the outer radiation belt in the equatorial plane. In order to do this, we will use a test particle model that solves the guiding center drift equations (Equations 2.31 and 2.32) using the outputs (electric and magnetic fields) from the ULF wave model described in the previous chapter. Once we have the solutions to the guiding center drift equations, we can trace the motion of all the particles to see how they behave in the presence of the MHD waves and from here, we can examine radial transport.

5.1 Test Particle Model

5.1.1 Choice of Magnetic Moment, M

In order to run the test particle model, one of the first things that needs to be done is the selection of a magnetic moment that is appropriate for the particle at its starting location. For radial transport, we require violation of the third adiabatic invariant, while holding the first and second invariants constant. For example, at geosynchronous orbit, the magnetic field strength is rougly 100 nT and a typical electron may have an energy of around 1 MeV. Therefore, as a rough guess, one could use $M = 0.01$ MeV/nT as the choice of magnetic moment for the test particle code.

To obtain a value of M in a more concrete manner, we will use the equation that governs drift resonances. In order to do this, we want to examine when the zeroth-order angular drift speed matches the phase speed of the wave (Degeling et al. [2007]). The phase of the wave is given by,

$$\psi(t) = m_N \phi - \omega t \tag{5.1}$$

where m_N is the wave mode number. If we take the derivative with respect to time of Equation 5.1, this gives us,

$$\frac{d\psi}{dt} = m_N \frac{d\phi}{dt} - \omega \tag{5.2}$$

where we may set $d\psi/dt = 0$ in Equation 5.2 in order to satisfy the resonance condition.

If we use Equation 2.32 in Equation 5.2, and use a dipole magnetic field (Equation 4.14) to calculate $\partial B/\partial r$, this gives us a condition for ω,

$$\omega = \frac{3 m_N M}{q \gamma r^2} \tag{5.3}$$

where r is the radius at which the electrons with magnetic moment M are resonant with waves of frequency ω (Degeling et al. [2007]). If we use Equation 2.33 (and rearrange for γ) in Equation 5.3, we get the following equation,

$$\left(\frac{r}{R_E}\right)^4 + \frac{2 r M B_E}{m_e c^2 R_E} - \left(\frac{3 m_N M}{q \omega R_E^2}\right)^2 = 0 \tag{5.4}$$

If we write Equation 5.4 in the following form,

$$AM^2 + BM + C = 0 \tag{5.5}$$

where,

$$\begin{cases} A = -\left[3 m_N / \left(q \omega R_E^2\right)\right]^2 \\ B = \left[2 r B_E / \left(m_e c^2 R_E\right)\right] \\ C = \left(r / R_E\right)^4 \end{cases} \tag{5.6}$$

then we can solve Equation 5.5 as a quadratic equation, given that the coefficients in Equation 5.6 are constant. This allows us to select an appropriate value for M to run the test particle model. The parameters chosen for Equation 5.6 are found in Table 5.1.

Table 5.1: Parameters chosen to determine the best value for the magnetic moment, M.

Parameter	Value
mode number, m_N	2
frequency, ν	7 mHz
Earth magnetic field at surface, B_E	31.1 μT
radial coordinate to resonance, r	5 R_E

5.1.2 Solving the Drift Equations

Now that we have settled the question on how to define the magnetic moment for the test particle run, we need to figure out how it is we will examine the radial transport aspect of the particles drifting in the radiation belts. We need to solve the guiding center drift equations, which are given by Equations 2.31 and 2.32. Solving these equations will allow us to look at the time evolution of the particle's motion in the presence of the electric and magnetic fields it encounters in the magnetosphere.

When solving a differential equation, we require either initial conditions or boundary conditions in order to restrict the number of solutions (e.g. Equation 4.10, without any conditions, has a multitude of solutions - it is only through the application of conditions to this equation that we get solutions of a specific form). As solving Equations 2.31 and 2.32 give us r_{gc} and ϕ_{gc}, we can use the initial position of the particle in r and ϕ as the initial conditions.

For a collection of particles, we create an array of initial conditions of the form $[r_{0i},\phi_{0i}]$, where i runs from 1 to N, the number of particles in the simulation, such that each individual particle has its own pair of initial conditions in r and ϕ.

In order to actually solve Equations 2.31 and 2.32, we provide the array of initial conditions to an explicit, adaptive Runge-Kutta (4,5) integration scheme in MATLAB, better known as the Dormand-Prince (DOPRI) method. The DOPRI method uses six function evaluations in order to calculate the fourth and fifth order solutions to a given differential equation. The main difference between the DOPRI method and other explicit Runge-Kutta (4,5) solvers is that DOPRI chooses its coefficients so as to minimize the error of the fifth order solution (Dormand & Prince [1980]).

5.1.3 Verification

One of the big questions when writing computational models is, "How is one sure the model is doing what it is supposed to do?" In order to answer that question, one must run the model in scenarios in which the outcome is already known. If the expected result is produced from the model, we can be pretty sure the model is doing what it is supposed to be doing. Conversely, if the result obtained from the model is not what we expect, it requires us to give a second look at the model and look for possible errors.

In the previous chapter, the plot of the Alfvén continuum was one of the ways to check the ULF wave model to see if the model predictions agreed with theory, which they did (cf. Section 4.3.3). For the test particle model, we shall examine how the particles behave without any perturbation from the waves. From Section

2.1.2.2, without any magnetic perturbation, a particle will travel perpendicular to both the magnetic field and its gradient and thus, the particle will drift on a contour of constant magnetic field (a constant drift shell, consistent with the third adiabatic invariant). This gives us a method of verify whether our test particle model is doing what we expect it to do. If we turn off the perturbations in the magnetic and electric fields (i.e. no waves), we should expect to trace the particles on a contour of constant magnetic field.

5.1.4 Statistical Analysis

5.1.4.1 Mean and Variance

During the model run, particles will orbit around Earth and move across drift shells (violating the third adiabatic invariant). At the final time, we want to check on which contour of constant magnetic field (L^*), defined by,

$$L^* = \left(\frac{B_E}{B}\right)^{\frac{1}{3}} \tag{5.7}$$

the particles are located and look at how this varies from the initial position of L^*. We are also interested to see how the particles spread out from the initial value of L^*.

In order to gather useful information from statistics, the electrons can be binned in a histogram according to L^* value with distribution function $f(L^*)$. The mean of the distribution is given by,

$$\langle L^* \rangle = \frac{\int_{-\infty}^{\infty} L^* f\left(L^*\right) dL}{\int_{-\infty}^{\infty} f\left(L^*\right) dL} \tag{5.8}$$

and its variance (spread) is given by,

$$\left\langle \left(\Delta L^*\right)^2 \right\rangle = \frac{\int_{-\infty}^{\infty} \left(L^* - \langle L^* \rangle\right)^2 f\left(L^*\right) dL}{\int_{-\infty}^{\infty} f\left(L^*\right) dL} \tag{5.9}$$

Equations 5.8 are 5.9 are best estimates and have associated error. For the mean, the error is given by,

$$\delta \langle L^* \rangle = \frac{\sigma_{L^*}}{\sqrt{N}} \tag{5.10}$$

where N is the number of measurements (electrons) and σ_{L^*} is the standard deviation in the distribution of L^*. For the variance, the error is given by (Taylor [1997]),

$$\delta\left\langle(\Delta L^*)^2\right\rangle = \sigma_{L^*}\sqrt{\frac{2}{N-1}} \tag{5.11}$$

Equations 5.10 and 5.11 allow us to place upper and lower bounds on our best estimates from Equations 5.8 and 5.9.

5.1.4.2 Connection to Electron Transport

The question to ask is, "How are Equations 5.8 and 5.9 connected to the transport of electrons?" The connection comes from examining the time evolution of Equations 5.8 and 5.9 as the wave driver along the magnetopause launches waves into the magnetosphere.

Equation 5.8 (also known as the first moment) characterizes the convective (bulk) transport of electrons. If the time evolution of $\langle L^* \rangle$ is linear (or quasi-linear), a trend line can be fit to the data. This would give rise to a convection coefficient.

Equation 5.9 (also known as the second moment) characterizes the diffusive transport of electrons. If the time evolution of $\left\langle(\Delta L^*)^2\right\rangle$ is linear (or quasi-linear), a trend line can be fit to the data. This would given rise to a diffusion coefficient (cf. Equation 2.68).

Using statistics and the time evolution of the first and second moments gives us a way of being able to characterize electron transport as either convective or diffusive. Furthermore, it also allows us to see which one dominates at a particular value of L^* in the radiation belts.

5.2 Particle Tracing Results

We will now consider results from the particle tracing model for the cases of low (300 km/s - Figures 4.4 and 4.5), moderate (700 km/s - Figures 4.6 and 4.7), and high (1,000 km/s - Figures 4.8 and 4.9) solar wind speeds.

As can be seen in Figures 4.10, 4.11, 4.12, and 4.13, as the solar wind speed is increased, the amplitude of the perturbations in the electric and magnetic fields also increases. When the magnetic field perturbations die out, the electric field perturbations do likewise (i.e. consistent with Faraday's law). This is important, as we are examining the transport of the particles under the influence of perturbed fields. If the perturbations are getting stronger with increased solar wind speed, there is an expectation this will change the trajectory the electrons follow in the outer radiation belt. This is something we will examine in our results.

The first set of results will start the ring of particles at the same value of L^* (in this case, $L^* = 6$) and examine how varying the solar wind speed has an effect on

the radial transport of the electrons. We can then examine the first and second moments to characterize the type of transport and if possible, fit trend lines to look at transport coefficients.

5.2.1 Starting at $L^* = 6$

In the test particle simulation, 300 particles are spaced in the equatorial plane at $L^* = 6$ with $M = 0.0550$ MeV/nT.

Figures 5.1, 5.3, and 5.5 show the position of the electrons in the equatorial plane as time evolves and the ULF waves pass through the magnetosphere with E_ϕ in the background for the cases of low, moderate, and high solar wind speeds. Figures 5.2, 5.4, and 5.6 show the distribution of particles by binning them in L^* for the cases of low, moderate, and high solar wind speeds.

As can be observed in Figures 5.1, 5.3, and 5.5, the particles are initially on the contour of $L^* = 6$. As time passes, the particles are perturbed from the initial contour as the ULF waves pass through the magnetosphere. In the final time frame, it can be seen that particles have spread out over the equatorial plane. In fact, as the solar wind speed is increased, the particles are transported further away from Earth and running along the magnetopause boundary. This is evident from the histograms in Figures 5.2, 5.4, and 5.6; for higher solar wind speeds, electrons are able to be transported to further drift shells in L^*, requiring them to lose energy as they move further away to keep the first adiabatic invariant, M, constant.

In Figures 5.3 and 5.5, it can be seen that some of the electrons, as they drift away from Earth, end up traveling along the magnetopause boundary. These electrons, instead of drifting further to higher L^* values, end up staying on the contour which skirts the magnetopause boundary. This is not entirely physical and is a limitation of the ULF wave model being used.

From Figures 5.2, 5.4, and 5.6, it should be noted that the particles tend to be transported to the right of the mean value of L^* (i.e. particles are transported radially outwards). This would indicate that the transport process is dependent on L^*, in that, particles are more inclined to move to a higher value of L^*. Some of the diffusion coefficients listed in Table 2.1 show transport (specifically, diffusion) can be dependent on the scaling of L.

In Figures 5.1, 5.2, 5.3, 5.4, 5.5, and 5.6, the evolution of time runs from top to bottom and the panels are represented by equal spacings in time from $t = 0$ (top panel) to $t_{\max} = 2,137.4$ seconds (bottom panel).

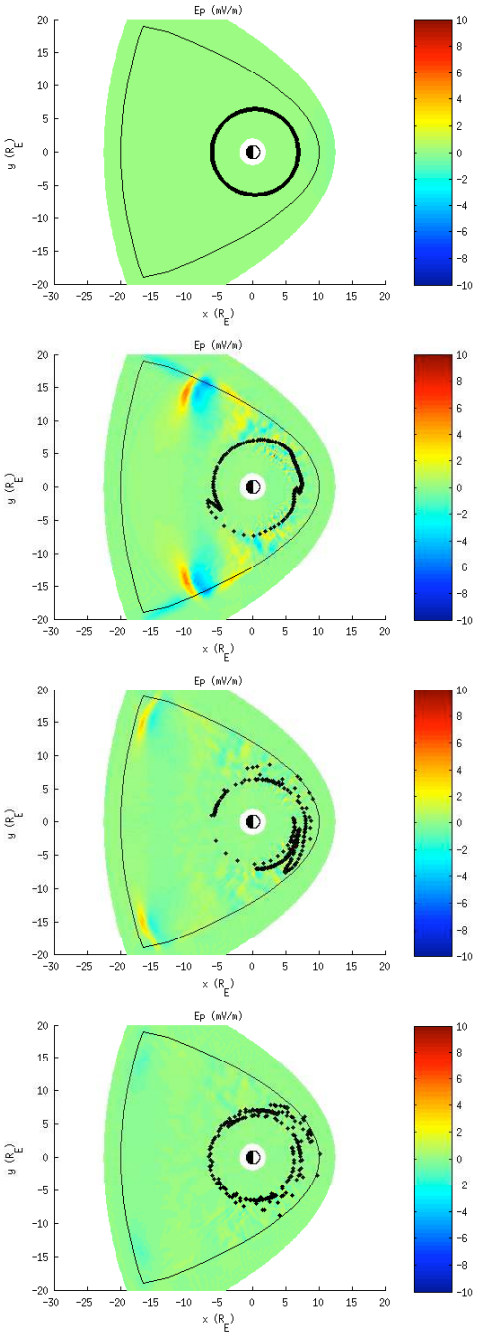

Figure 5.1: Electrons undergoing radial transport with $v_{SW} = 300$ km/s with E_ϕ in the background.

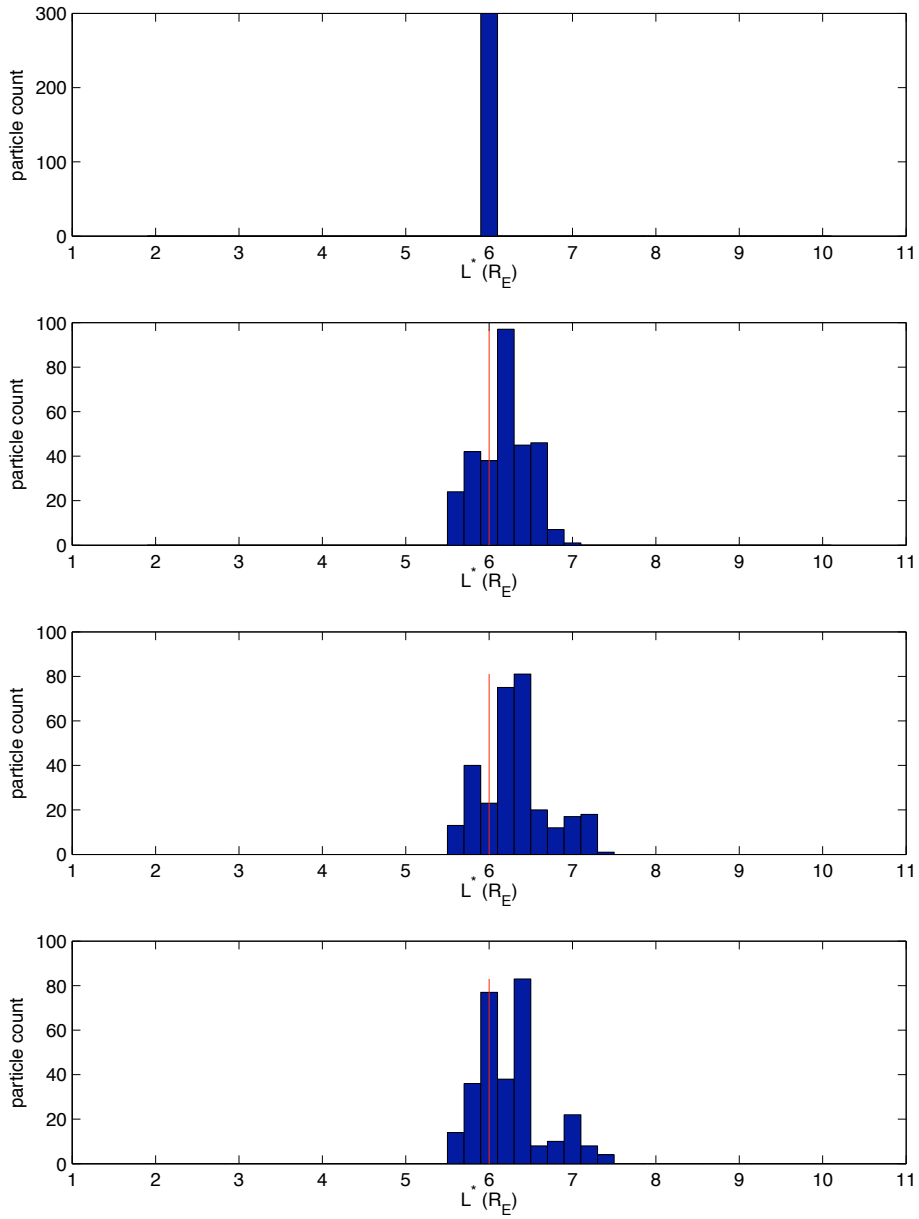

Figure 5.2: Distribution of electron position in L^* for $v_{SW} = 300$ km/s (vertical red line is initial position).

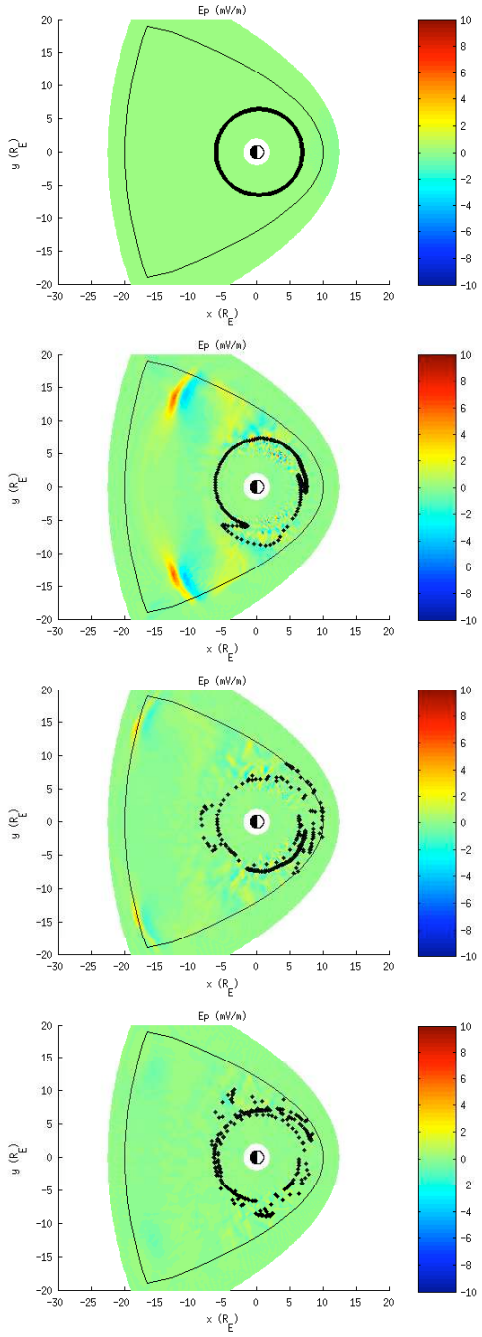

Figure 5.3: Electrons undergoing radial transport with $v_{SW} = 700$ km/s with E_ϕ in the background.

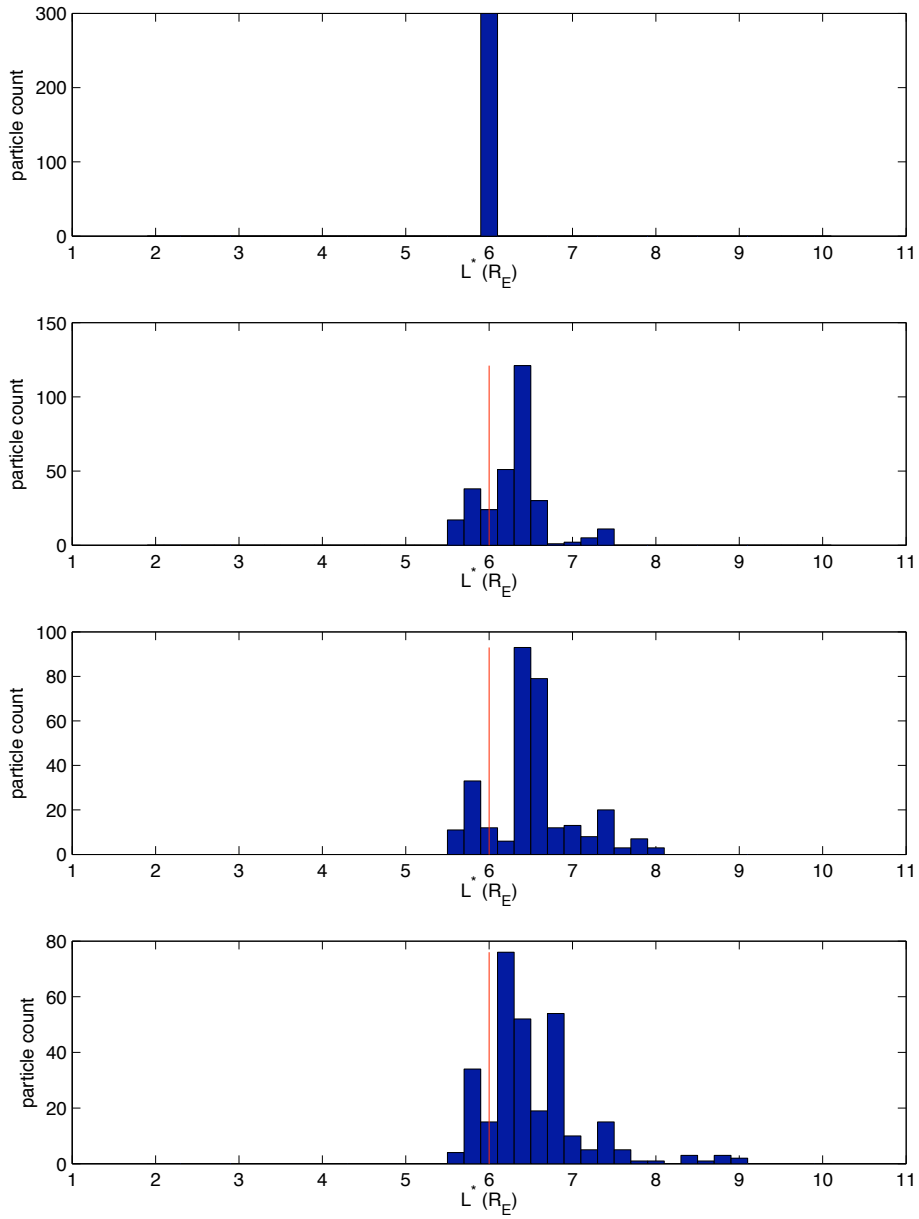

Figure 5.4: Distribution of electron position in L^* for $v_{SW} = 700$ km/s (vertical red line is initial position).

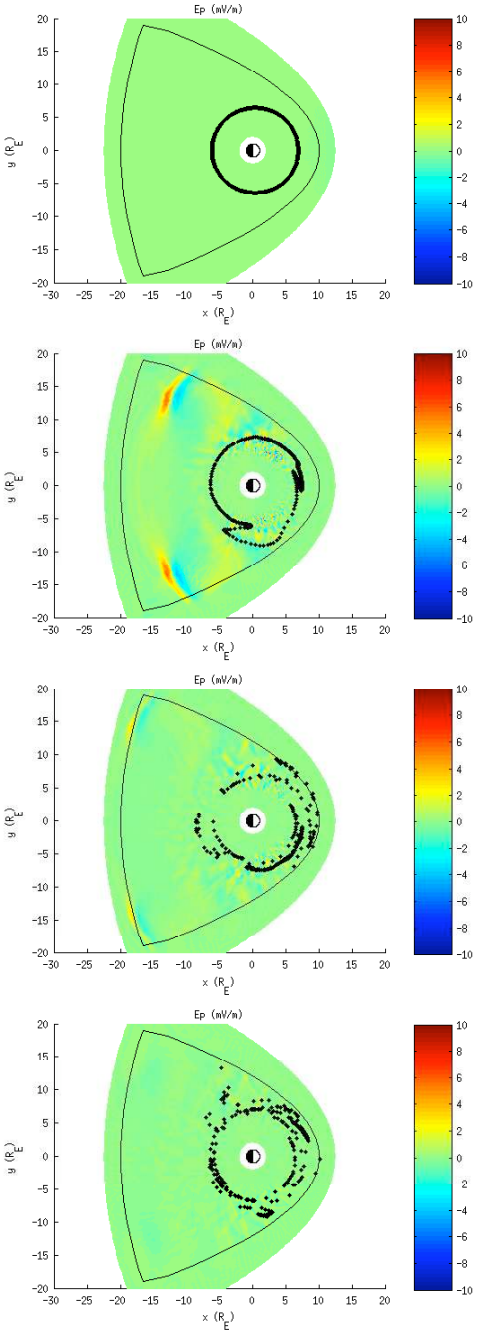

Figure 5.5: Electrons undergoing radial transport with $v_{SW} = 1,000$ km/s with E_ϕ in the background.

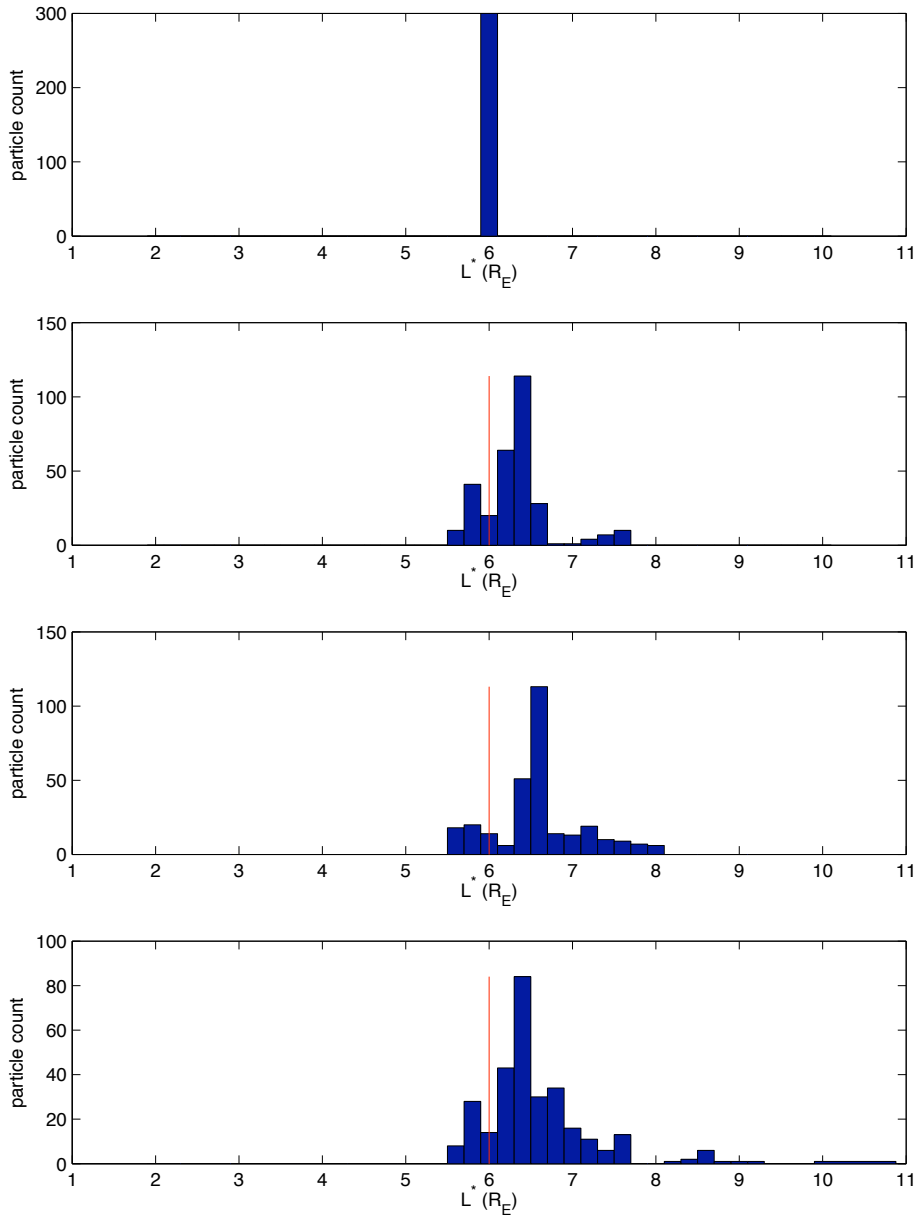

Figure 5.6: Distribution of electron position in L^* for $v_{SW} = 1,000$ km/s (vertical red line is initial position).

5.2.2 Convective of Diffusive Transport?

Figures 5.7, 5.8, and 5.9 show the time evolution of the first and second moments for the low, moderate, and high solar wind speed cases.

In order to look at transport coefficients, the data is fit with a trend line using linear least-squares fitting (cf. Chapter 8, [Taylor, 1997]). From this, the data can be assessed to see if it is following a linear or near-linear trend by examining how the trend line fits within the error bars of the data. If, for the duration of the model run, the data follows a trend that can be described as linear (or near-linear), the slope of the linear least-squares trend line can be taken to calculate a transport coefficient for the electrons.

In the case of the first moment (the mean value of L^*), it follows a quasi-linear trend until it begins to level off. Where it begins to level off changes with the solar wind speed; increasing the solar wind speed delays the point where the mean levels off. Furthermore, increasing the solar wind speed increases the overall value of the mean, indicating a greater exchange of energy between the electrons and waves to conserve M. Note that the energy flow is from particles to waves and not vice-versa. This is because the particles (or test particles) in our model are not self-consistently coupled back to the waves.

The second moment (variance in the distribution) follows a quasi-linear trend for the duration of the model run. As the energy exchange between electrons and waves increases for greater solar wind speeds (because the amplitude of the wave increases with solar wind speed), there is also an increase in the variance, as the particles are much more spread out in the equatorial plane.

Now, as the title of this subsection suggests, "Is this convective or diffusive transport?" The short answer is that, from examination of Figures 5.7, 5.8, 5.9, the electrons are undergoing both convective and diffusive transport. Neither mode of transportation particularly dominates during the run of the simulation.

As mentioned, the first moment begins to level off during the simulation, while at the same time, the second moment continues to follow a quasi-linear trend. In this region, diffusion would begin to take precedence as the variance is still increasing (i.e. the particles are still spreading out), while the mean of the distribution is roughly constant. It should be noted, however, that in terms of absolute numbers of the deviation from the mean and the variance, they are roughly equivalent and hence, both modes of transport are equally important. Furthermore, it can be seen in Equation 2.61 that the transport coefficients are linked through D_{LL}.

In the region where the first moment is following a quasi-linear trend, one could calculate a convection coefficient, however, this is beyond the scope of this thesis as convection coefficients are not being considered.

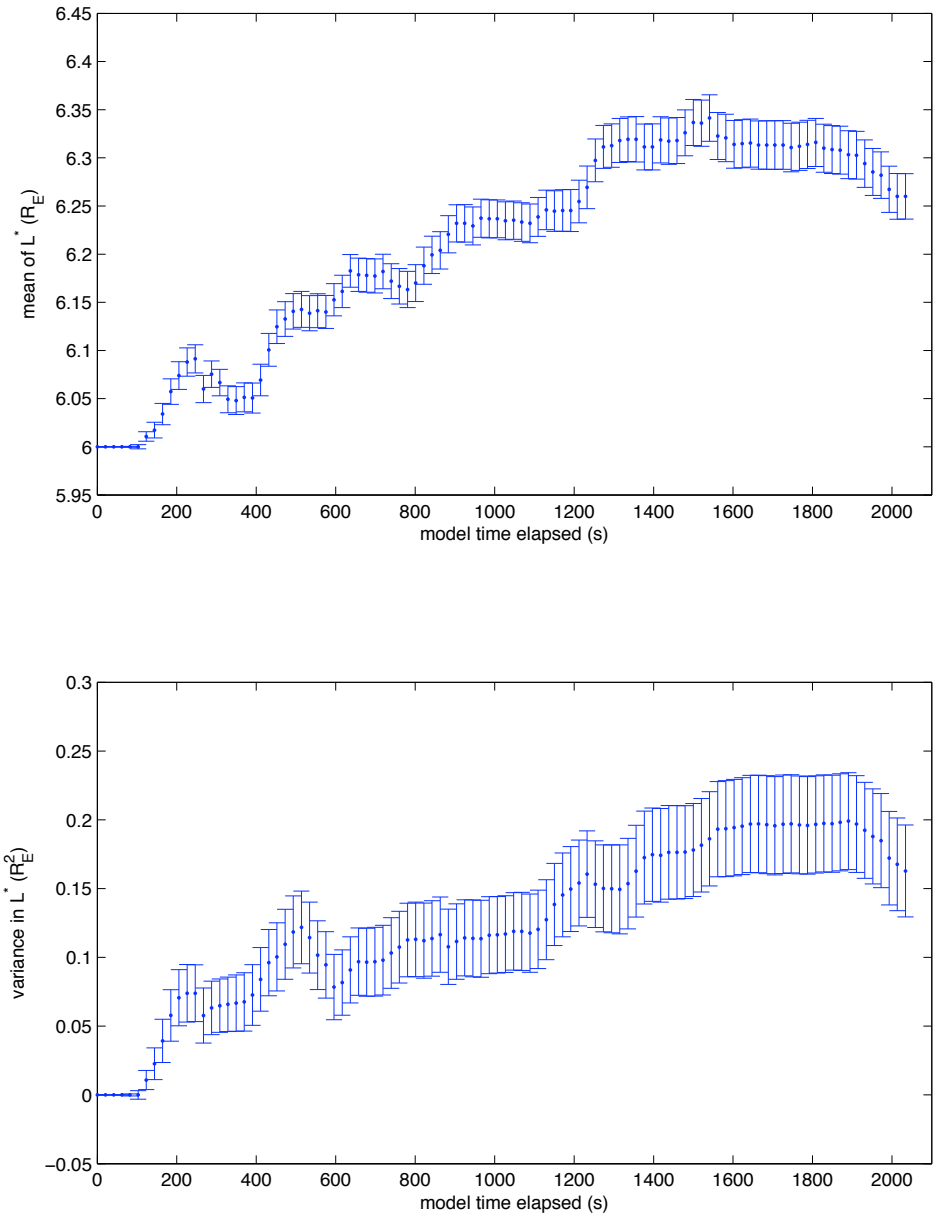

Figure 5.7: Time evolution of the first and second moments for electrons starting at $L^* = 6$ with $v_{SW} = 300$ km/s.

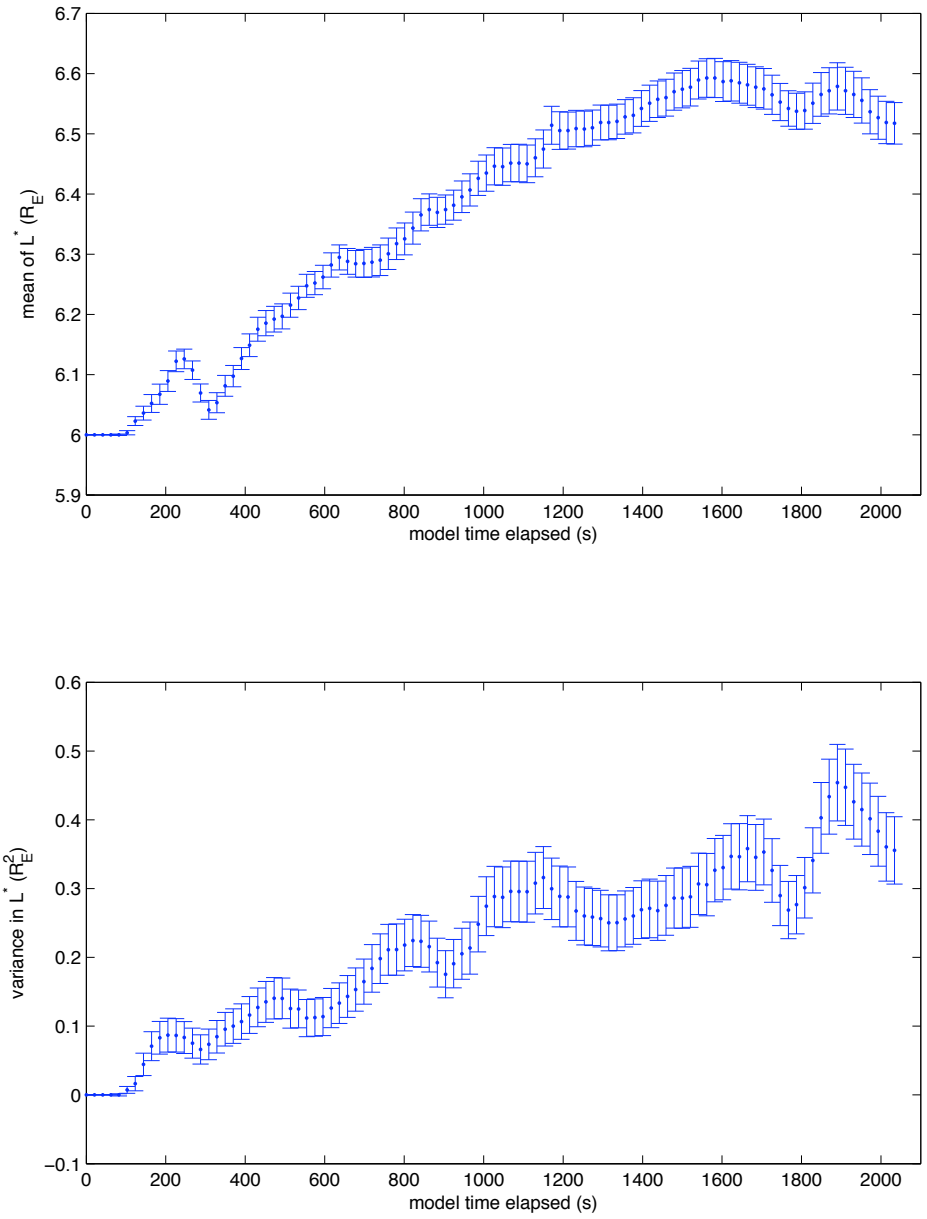

Figure 5.8: Time evolution of the first and second moments for electrons starting at $L^* = 6$ with $v_{SW} = 700$ km/s.

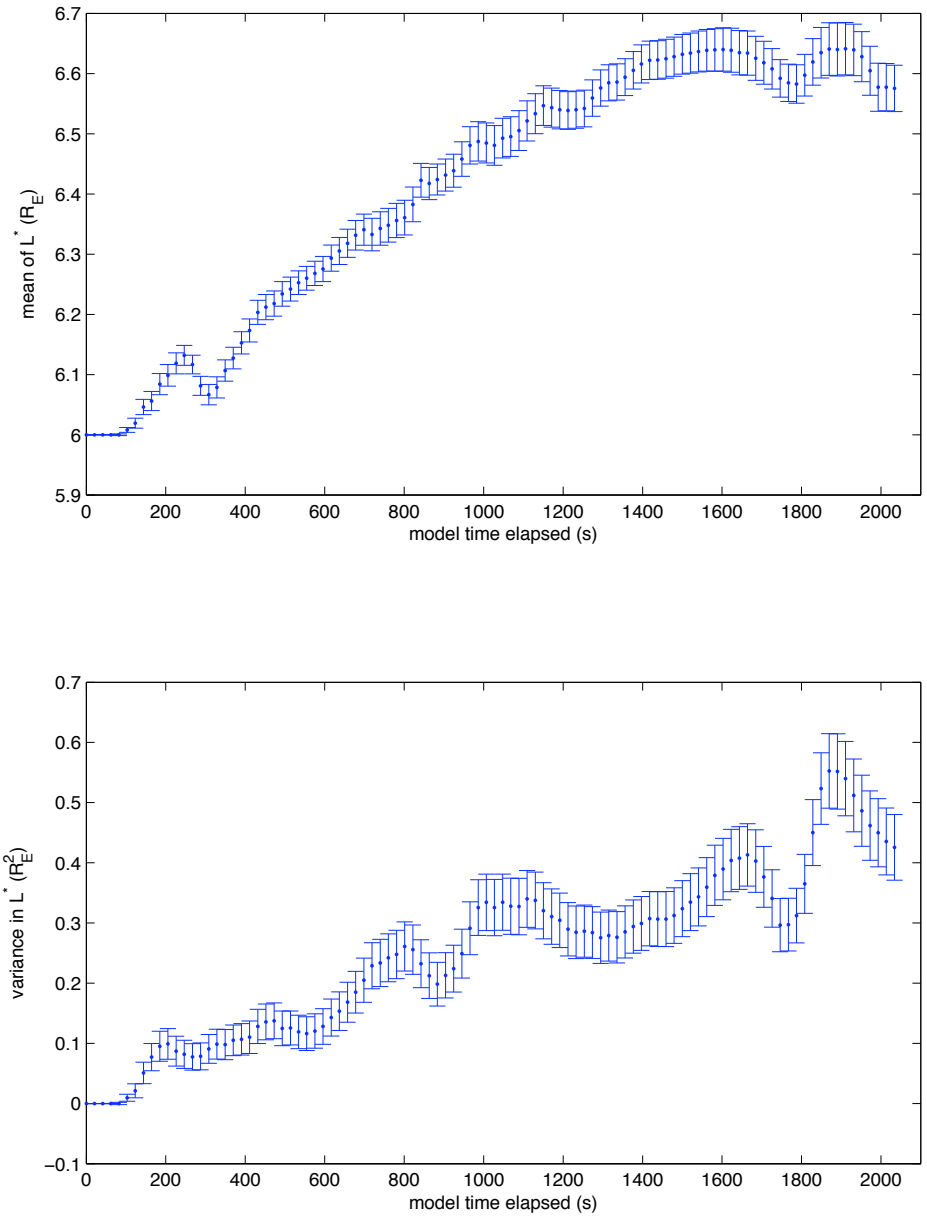

Figure 5.9: Time evolution of the first and second moments for electrons starting at $L^* = 6$ with $v_{SW} = 1,000$ km/s.

5.2.3 Calculating D_{LL}

Although we are not considering convection coefficients for electron transport in the equatorial plane, we are considering the diffusion coefficient. If Equation 2.68 is rearranged in the form,

$$\left\langle (\Delta L^*)^2 \right\rangle = (2D_{LL})\tau \tag{5.12}$$

then we can calculate D_{LL} from the slope of the graph showing the time evolution of the variance of the distribution of particles in L^*.

In Figures 5.10, 5.11, 5.12, a linear trend line is fit to the data. Note that the first five data points from the second moments plots in Figures 5.7, 5.8, and 5.9 are removed before the trend line is fitted to the data. The justification for this is that as the wave driver begins to generate ULF waves, it takes time for the waves to reach the electrons and begin to transport them. These points, when the waves are coming to them, only serve to skew the trend line.

Table 5.2: Diffusion coefficient, D_{LL}, calculated for electrons in the outer radiation belt with initial position at $L^* = 6$ for low, moderate, and high solar wind speeds.

v_{SW} (km/s)	D_{LL} (day^{-1})
300	3.673
700	7.750
1,000	9.329

Table 5.1 shows the values obtained for the diffusion coefficient from the data gives in Figures 5.10, 5.11, 5.12, with the unit of D_{LL} converted from s^{-1} to hr^{-1} to be consistent with Table 2.1.

Increasing the solar wind speed increases the rate of diffusion. As the solar wind speed is increased, the exchange of energy between the electrons and waves also increases such that the electrons lose energy to move to higher L^*, consistent with conservation of the first adiabatic invariant.

Lastly, one could scan over several values of L^* to observe just how D_{LL} scales with L^*,

$$D_{LL} = \alpha L^{*\beta} \tag{5.13}$$

by calculating D_{LL} at each L^* value, then plotting D_{LL} versus L^* on a log-log plot, which would give the scaling coefficient β from the slope (assuming the trend is linear on the log-log plot). The scaling of the diffusion coefficient with L^*, however, has not been analyzed in this thesis (i.e. determining β in Equation 5.13). This is left to future work.

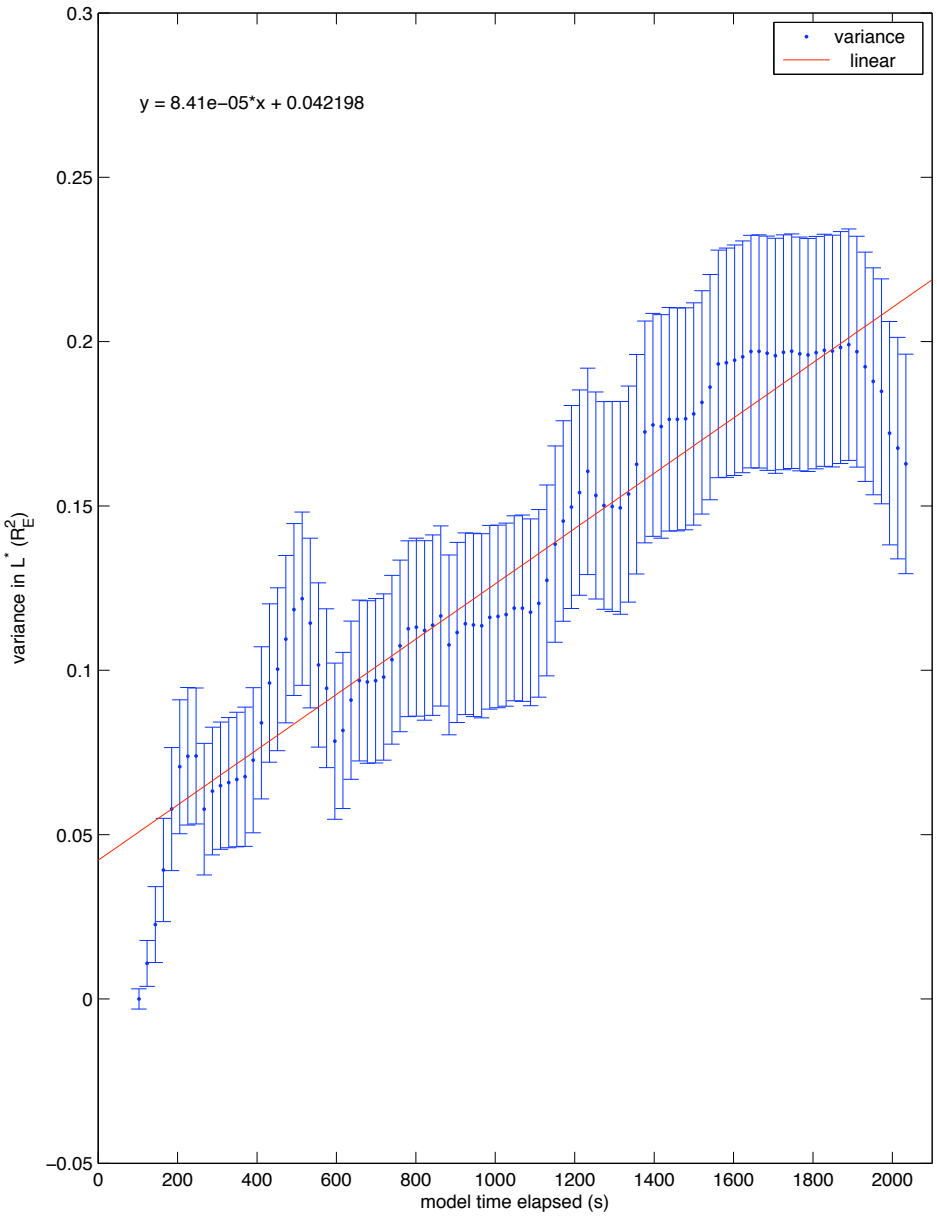

Figure 5.10: Application of a linear trend to the second moment from Figure 5.7 to determine D_{LL}.

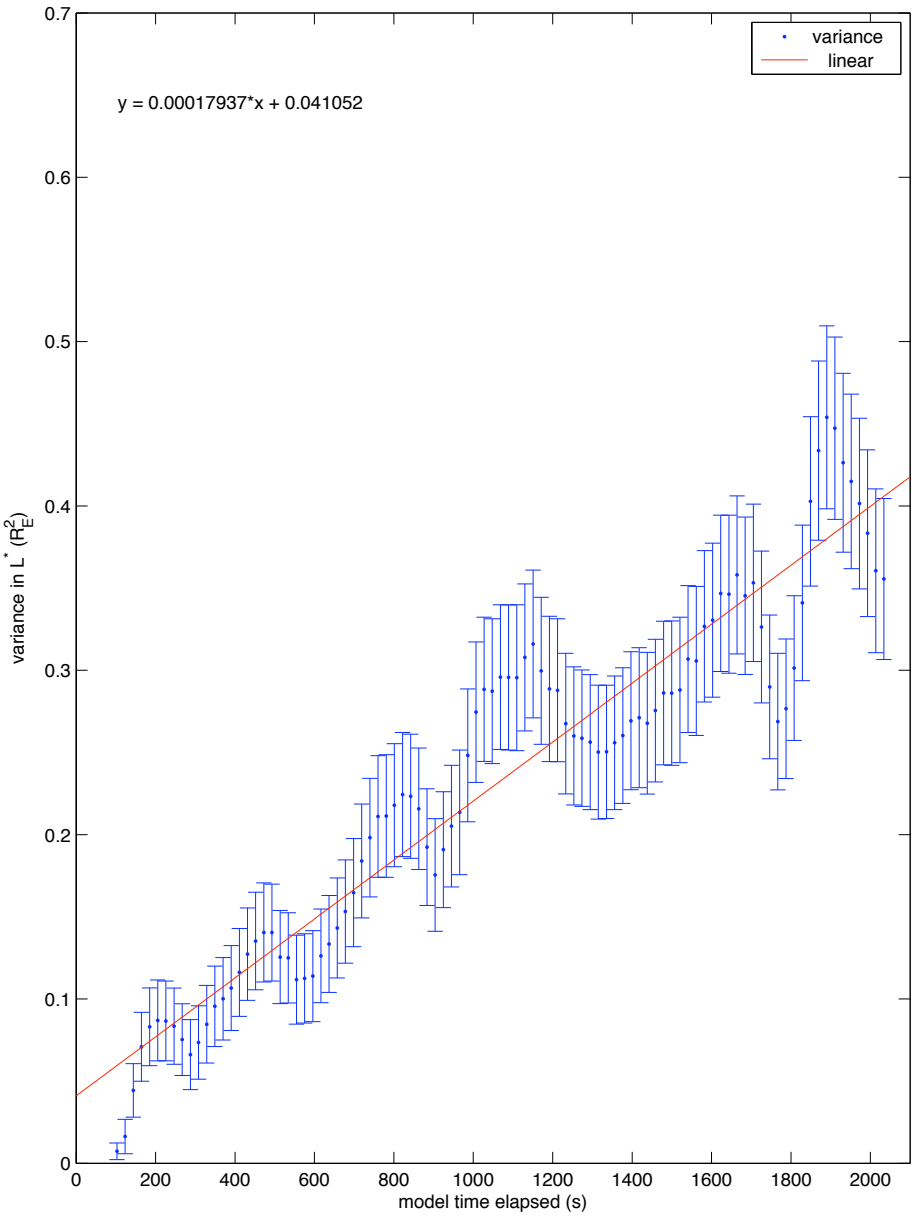

Figure 5.11: Application of a linear trend to the second moment from Figure 5.8 to determine D_{LL}.

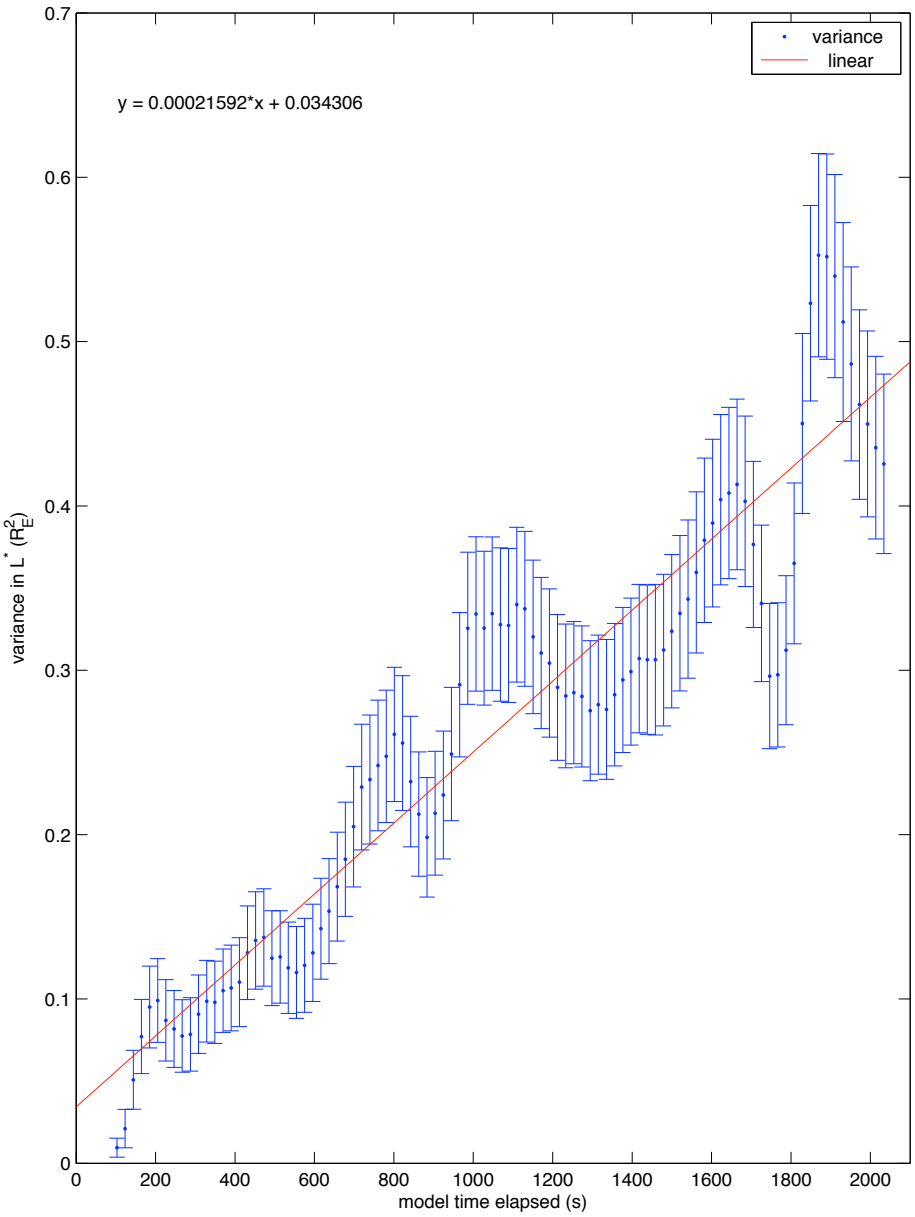

Figure 5.12: Application of a linear trend to the second moment from Figure 5.9 to determine D_{LL}.

Chapter 6

Conclusion

6.1 Summary

Over the last five chapters, we have presented the basis for how to understand radial transport of electrons in the outer radiation belt. The journey first started with laying the foundation for the environment in which we wished to examine electron transport. We followed this with an examination of particle dynamics and how they are influenced by the electric and magnetic fields.

Once we had an understanding of our environment and the particles, we moved onto talking about how ULF waves are generated in the magnetosphere by an external current driver located on the magnetopause boundary and how to classify the waves based on the dispersion relations from MHD theory.

We then brought our attention to the specifics of the ULF wave model of [Degeling et al., 2011] and examined the effects on the radial and azimuthal electric fields due to the perturbations in the magnetic field brought on by the wave driver. Using the outputs from the model, this allowed us to trace electrons in the equatorial plane and discuss whether they were undergoing convective or diffusive transport and then calculate the diffusion coefficient, D_{LL}, based on the time evolution of the variance of the distribution of particles in L^* (we had not considered the convection coefficient for electron transport).

As the solar wind speed was increased, from the distribution of particles in Figures 5.2, 5.4, and 5.6, two things can be observed. First, particles have a tendency to move towards higher L^* values, indicating transport is proportional to $L^{*\beta}$ (where β is a scaling power). Second, as the solar wind speed is increased, particles are able to be transported to higher L^* values (in Figure 5.2, the highest L^* value is found between 7 and 8 R_E, whereas in Figure 5.6, the highest L^* value is found around 11 R_E). This would indicate that as the solar wind speed is increased, there is a greater energy exchange between the electrons and waves such that the electrons are losing more energy as solar wind speed is increased in order to

conserve M.

Through examination of the plots of the first and second moments over the course of the model run, it was found that both convective and diffusive transport played an important role, although in the region the first moment began to level off (hence, the mean was roughly constant) while the second moment continued to grow in a quasi-linear fashion, diffusion started to take a more prominent role (although in terms of numbers, the deviation of the mean and the variance were on the same order of magnitude). This allowed us to calculate diffusion coefficients for electron transport (see Table 5.2), which increased as the solar wind speed increased.

The key point to take from this is the solar wind speed has a direct effect on radial transport of electrons in the radiation belt. As the speed is increased, the electrons are able to be transported further out in the radiation belts (to higher L^*), which, through conservation of the first adiabatic invariant, requires the electrons to lose more energy to waves as the solar wind speed is increased.

6.2 Future Work

Given that radiation belt physics is not the most well understood area in space physics, there is great potential for future work, even for electrons in the equatorial plane.

As mentioned in Section 5.1.1, the choice of magnetic moment for the particles is a key part of the test particle code. For this thesis, M was kept constant for all the runs at $L^* = 6$. It would be of interest to note how D_{LL} scales with M in order to examine the effect (and to what degree) the magnetic moment has on electron dynamics in the outer radiation belt.

Also, in terms of scaling, it would be of interest to see how D_{LL} scales as a function of L for the various solar wind speeds. This is something that has been done by other authors (cf. Table 2.1), however, this was not considered in the scope of this thesis.

Another area of interest would be to study convective transport in depth. Although it was mentioned briefly in Chapters 2 and 5, it was not explored in depth, as it was not part of the scope of this thesis. Figures of the first moment versus time for low, moderate, and high solar wind speeds show that for a significant portion of the model run, the trend is quasi-linear and that a convection coefficient could be derived. This would be something to consider in future work when dealing with electrons in the equatorial plane.

We have been confined to the equatorial plane and kept the second adiabatic invariant constant at $J = 0$. It would be of interest to move off the equatorial

plane and begin to consider effects such as the curvature of field lines and the magnetic field becoming a function of latitude.

There is much potential for future work, both for equatorially mirroring electrons and for those being transported in 3D models.

Bibliography

Baumjohann, W. & Treumann, R. A. (1997). *Basic Space Plasma Physics* (4th ed.). Imperial College Press.

Borovsky, J. E. & Denton, M. H. (2006). Differences between CME-driven storms and CIR-driven storms. *Journal of Geophysical Research*, *111*.

Chiu, Y. T., Nightingale, R., & Rinaldi, M. (1988). Simultaneous radial and pitch angle diffusion in the outer electron radiation belt. *Journal of Geophysical Research*, *93*, 2619.

Claudepierre, S. G., Hudson, M. K., Lotko, W., Lyon, J. G., & Denton, R. E. (2010). Solar wind driving of magnetospheric ULF waves: Field line resonances driven by dynamic pressure fluctuations. *Journal of Geophysical Research*, *115*.

Degeling, A. W., Rankin, R., & Elkington, S. R. (2011). Convective and diffusive ULF wave driven radiation belt electron transport. *Journal of Geophysical Research*, *116*.

Degeling, A. W., Rankin, R., Kabin, K., Marchand, R., & Mann, I. R. (2007). The effect of ULF compressional modes and field line resonances on relativistic electron dynamics. *Planetary and Space Science*, *55*, 731–742.

Degeling, A. W., Rankin, R., Kabin, K., Rae, I. J., & Fenrich, F. R. (2010). Modeling ULF waves in a compressed dipole magnetic field. *Journal of Geophysical Research*, *115*.

Denton, M. H., Borovsky, J. E., Skoug, R. M., Thomsen, M. F., Lavraud, B., Henderson, M. G., McPherron, R. L., Zhang, J. C., & Liemohn, M. W. (2006). Geomagnetic storms driven by ICME- and CIR-dominated solar wind. *Journal of Geophysical Research*, *111*.

D'haeseleer, W. D., Hitchon, W. N. G., Callen, J. D., & Shohet, J. L. (1991). *Flux Coordinates and Magnetic Field Structure* (1st ed.). Springer-Verlag.

Dormand, J. R. & Prince, P. J. (1980). A family of embedded Runge-Kutta formulae. *Journal of Computational and Applied Mathematics*, *6(1)*, 19–26.

Elkington, S. R. (2006). A Review of ULF Interactions with Radiation Belt Electrons. *AGU Monograph*, *169*, 177–193.

Elkington, S. R., Hudson, M. K., & Chan, A. A. (1999). Acceleration of relativistic electrons via drift-resonant interaction with toroidal-mode Pc-5 ULF oscillations. *Geophysics Research Letters*, *26(21)*, 3273.

Elkington, S. R., Hudson, M. K., & Chan, A. A. (2003). Resonant acceleration and diffusion of outer zone electrons in an asymmetric geomagnetic field. *Journal of Geophysical Reseach*, *108*.

Green, J. C. & Kivelson, M. G. (2004). Relativistic electrons in the outer radiation belt: Differentiating between acceleration mechanisms. *Journal of Geophysical Research*, *109*.

Griffiths, D. J. (1998). *Introduction to Electrodynamics* (3rd ed.). Addison-Wesley.

Holzworth, R. H. & Mozer, F. S. (1979). Direct evaluation of the radial diffusion coefficient near $L = 6$ due to electric field fluctuations. *Journal of Geophysical Research*, *84*, 2559.

Hudson, M. K., Kress, B. T., Mueller, H.-R., Zastrow, J. A., & Blake, J. B. (2008). Relationship of the Van Allen radiation belts to solar wind drivers. *Journal of Atmospheric and Solar-Terrestrial Physics*, *70*, 708–729.

Jacobs, J. A., Kato, Y., Matsushita, S., & Troitskaya, V. A. (1964). Classification of geomagnetic micropulsations. *Journal of Geophysical Reseach*, *69*, 180.

Kabin, K., Rankin, R., Mann, I. R., Degeling, A. W., & Marchand, R. (2007). Polarization properties of standing shear Alfvén waves in non-axisymmetric background magnetic fields. *Annales Geophysicae*, *25*, 815–822.

Kivelson, M. G. & Russell, C. T. (1995). *Introduction to Space Physics* (1st ed.). Cambridge University Press.

Lanzerotti, L. J., MacLennan, C. G., & Schulz, M. (1970). Radial diffusion of outer-zone electrons: An empirical approach to third-invariant violation. *Journal of Geophysical Research*, *75*, 5351.

Lanzerotti, L. J. & Morgan, C. G. (1973). ULF geomagnetic power near $L = 4$ - 2. Temporal variation of the radial diffusion coefficient for relativistic electrons. *Journal of Geophysical Research*, *78*, 4600.

Lyons, L. R., Thorne, R. M., & Kennel, C. F. (1972). Pitch-angle diffusion of radiation belt electrons within the plasmasphere. *Journal of Geophysical Research*, *77*, 3455.

Mann, I. R., O'Brien, T. P., & Milling, D. K. (2004). Correlations between ULF wave power, solar wind speed, and relativistic electron flux in the magnetosphere. *Journal of Atmospheric and Solar-Terrestrial Physics*, *66*, 187.

Mathie, R. A. & Mann, I. R. (2000). A correlation between extended intervals of ULF wave power and storm-time geosynchronous relativistic electron flux enhancements. *Geophysics Research Letters*, *27*, 10,713.

Menk, F., Orr, D., Clilverd, M., Smith, A., Waters, C., Milling, D., & Fraser, B. (1999). Monitoring spatial and temporal variations in the dayside plasmasphere using geomagnetic field line resonances. *Journal of Geophysical Research*, *104*, 19,955–19,969.

Myint-U, T. & Debnath, L. (2007). *Linear Partial Differential Equations* (4th ed.). Birkhaüser.

Newkirk, L. L. & Walt, M. (1968a). Radial diffusion coefficient for electrons at $1.76 < L < 5$. *Journal of Geophysical Research*, *73*, 7231.

Newkirk, L. L. & Walt, M. (1968b). Radial diffusion coefficient for electrons at low L values. *Journal of Geophysical Research*, *73*, 1013.

Northrup, T. G. (1963). *The Adiabatic Motion of Charged Particles* (1st ed.). Interscience Publishers.

O'Brien, T. P., McPherron, R. L., Sornette, D., Reeves, G. D., Friedel, R., & Singer, H. J. (2001). Which magnetic storms produce relativistic electrons at geosynchronous orbit? *Journal of Geophysical Research*, *106(A8)*, 15,533.

Rankin, R., Kabin, K., & Marchand, R. (2006). Alfvénic field line resonances in arbitrary magnetic field topology. *Advances in Space Research*, *38*, 1720–1729.

Ray, E. C. (1963). On the Motion of Charged Particles in the Geomagnetic Field. *Annals of Physics*, *24*, 1–18.

Roederer, J. G. (1970). *Dynamics of Geomagnetically Trapped Radiation* (1st ed.). Springer-Verlag.

Rostoker, G., Skone, S., & Baker, D. N. (1998). On the origin of relativistic electrons in the magnetosphere associated with some geomagnetic storms. *Geophysics Research Letters*, *25*, 3701.

Samson, J. C., Jacobs, J. A., & Rostoker, G. (1971). Latitude-Dependent Characteristics of Long-Period Geomagnetic Micropulsations. *Journal of Geophysical Research*, *76(16)*, 3675–3683.

Schulz, M. & Lanzerotti, L. (1974). *Particule Diffusion in Radiation Belts* (1st ed.). Springer-Verlag.

Selesnick, R. S., Blake, J. B., Kolasinski, W. A., & Fritz, T. A. (1997). A quiescent state of 3 to 8 MeV radiation belt electrons. *Geophysics Research Letters*, *24*, 1343.

Stern, D. P. (1985). Parabolic Harmonics in Magnetospheric Modeling: The Main Dipole and the Ring Current. *Journal of Geophysical Research*, *90*, 10,851–10,863.

Taylor, J. R. (1997). *An Introduction to Error Analysis* (2nd ed.). University Science Books.

Tomassian, A. D., Farley, T. A., & Vampola, A. L. (1972). Inner-zone energetic electron repopulation by radial diffusion. *Journal of Geophysical Research*, *77*, 3441.

Walker, A. D. M. (2002). Excitation of field line resonances by MHD waves originating in the solar wind. *Journal of Geophysical Research*, *107*, 1481.

Zhu, X. & Kivelson, M. G. (1988). Analytic Formulation and Quantitative Solutions of the Coupled ULF Wave Problem. *Journal of Geophysical Research*, *93*, 8,602–8,612.

Appendix A

Derivation of the ULF Wave Model Equation

The derivation of the equation that governs the ULF wave model is of utmost importance to us. We require an equation to govern our system and without it, we can know virtually nothing about it. While the derivation is important, it is also quite cumbersome and detracts from the main points being made in Chapter 4, so we will present it in this appendix.

The approach taken in the appendix is based on work done previously by [Rankin et al., 2006], [Kabin et al., 2007], and [Degeling et al., 2010].

A.1 Mathematical Interlude

A.1.1 Field Aligned Coordinate System

Given a physical problem, an appropriate choice of coordinate system is needed and in certain cases, a specific choice of coordinate system will make the task of solving the problem much easier. This also serves true when looking at waves in the near-Earth environment. In deriving the equations for the wave model, we will use what is known as the field aligned coordinate system taken from [Rankin et al., 2006].

In the field aligned coordinate system, the three coodinates are α, β, and γ. The coordinate α is the distance from the center of Earth to the field line being examined. The coordinate β is the azimuthal angle, ϕ, that is swept in the equatorial plane. Finally, the coordinate γ is the distance along a particular field line. The coordinate system (α,β,γ) is non-orthogonal with the lone exception being if the magnetic field is a pure dipole field (Rankin et al. [2006]).

We can define the magnetic field, $\mathbf{B}$, using the field aligned coordinate system (Rankin et al. [2006], Degeling et al. [2010]),

$$\mathbf{B} = B_0\left(\alpha, \beta\right) \nabla\alpha \times \nabla\beta \tag{A.1}$$

where $B_0\left(\alpha, \beta\right)$ is the magnetic field in the equatorial plane as a function of the coordinates α and β.

A.1.2 Flux Coordinates

In order to derive the wave equation, we need to establish a covariant-contravariant formalism using our field aligned coordinate system. In order to do this, we need to look at some of the specific mathematics involved. The formalism that follows is taken from [D'haeseleer et al., 1991].

A.1.2.1 Reciprocal-Basis Vectors

If we have a transformation, $\mathbf{R}$, we can write it in terms of the coordinate basis (u^1, u^2, u^3). This allows us to establish tangent-basis vectors,

$$\begin{cases} \mathbf{e_1} = \partial\mathbf{R}/\partial u^1 \\ \mathbf{e_2} = \partial\mathbf{R}/\partial u^2 \\ \mathbf{e_3} = \partial\mathbf{R}/\partial u^3 \end{cases} \tag{A.2}$$

If we have a function, λ, and its gradient, $\nabla\lambda$, we know from vector calculus that we can write the differential of λ as,

$$d\lambda = \nabla\lambda \cdot d\mathbf{R} \tag{A.3}$$

with $\mathbf{R}$ acting as a position vector. If we define λ as being our coordinate basis vector, u^i (where i is an index), such that $\lambda \equiv u^i$, this allows us to rewrite the relationship in Equation A.3 as,

$$du^i = \nabla u^i \cdot d\mathbf{R} \tag{A.4}$$

From Equation A.4, we can expand $d\mathbf{R}$ by using the chain rule, since we know $\mathbf{R}$ is a function of the coordinate basis u^i. This expansion, using the Einstein summation convention, is,

$$d\mathbf{R} = \frac{\partial\mathbf{R}}{\partial u^j} du^j \tag{A.5}$$

If we look at the first term on the right hand side of Equation A.5, we see that this is the same form as the tangent-basis vector in Equation A.2. This allows us to rewrite Equation A.5 as,

$$d\mathbf{R} = \mathbf{e}_j u^i \tag{A.6}$$

If we insert Equation A.6 into A.4, we get,

$$du^i = \nabla u^i \cdot \mathbf{e}_j du^j \tag{A.7}$$

This imposes the condition that Equation A.7 can only hold if and only if,

$$\nabla u^i \cdot \mathbf{e}_j = \delta_i^j \tag{A.8}$$

where δ_i^j is the Knoecker delta function. Equation A.8 defines the reciprocal-basis vectors:

$$\mathbf{e}^i \equiv \nabla u^i \tag{A.9}$$

From the definition in Equation A.9, we can construct reciprocal-basis vectors for our field line coordinate system,

$$\begin{cases} \mathbf{e}^\alpha = \nabla\alpha \\ \mathbf{e}^\beta = \nabla\beta \\ \mathbf{e}^\gamma = \nabla\gamma \end{cases} \tag{A.10}$$

These basis vectors can be seen in the definition of the magnetic field in Equation A.1.

A.1.2.2 Vector Decomposition

If we have a vector, $\mathbf{V}$, we can decompose it into its covariant and contravariant components. We may write $\mathbf{V}$ in covariant form as,

$$\mathbf{V} = \left(\mathbf{V} \cdot \frac{\partial \mathbf{R}}{\partial u^i}\right) \nabla u^i = (\mathbf{V} \cdot \mathbf{e}_i)\, \mathbf{e}^i \tag{A.11}$$

Equation A.11 allows us to write the vector in component form,

$$\mathbf{V} = V_i \mathbf{e}^i \tag{A.12}$$

We can also write Equations A.11 and A.12 in contravariant form (for completeness),

$$\mathbf{V} = \left(\mathbf{V} \cdot \nabla u^i\right) \frac{\partial \mathbf{R}}{\partial u^i} = \left(\mathbf{V} \cdot \mathbf{e}^i\right) \mathbf{e}_i \tag{A.13}$$

Equation A.13 allows us to write the vector in component form,

$$\mathbf{V} = V^i \mathbf{e}_i \tag{A.14}$$

Both the covariant and the contravariant decompositions of a vector have equal standing (i.e. they are both equally valid).

A.1.2.3 Metric Coefficients and Tensor

If we impose a condition such that there are no field-aligned currents in the system (i.e. $\mathbf{B} \cdot \mathbf{J} = 0$), this allows Equation A.1 to be written as,

$$\mathbf{B} = \sigma \nabla \gamma \tag{A.15}$$

where σ is a scalar function of space (Ray [1963]). This allows us, from looking at Equations A.1 and A.15, to write,

$$\sigma \nabla \gamma = B_0 \left(\alpha, \beta\right) \nabla \alpha \times \nabla \beta \tag{A.16}$$

If we dot Equation A.16 with itself, we have,

$$\sigma^2 \nabla \gamma \cdot \nabla \gamma = \left[B_0 \left(\alpha, \beta\right)\right]^2 \left(\nabla \alpha \times \nabla \beta\right) \cdot \left(\nabla \alpha \times \nabla \beta\right) \tag{A.17}$$

From [D'haeseleer et al., 1991], we have a useful vector relationship to cast Equation A.17 in a more useful form. The vector relationship we seek is,

$$\left(\mathbf{A} \times \mathbf{B}\right) \cdot \left(\mathbf{C} \times \mathbf{D}\right) = \left(\mathbf{A} \cdot \mathbf{C}\right) \left(\mathbf{B} \cdot \mathbf{D}\right) - \left(\mathbf{A} \cdot \mathbf{D}\right) \left(\mathbf{B} \cdot \mathbf{C}\right) \tag{A.18}$$

Equation A.18 allows us to modify the right hand side of Equation A.17, such that we have,

$$\sigma^2 \nabla \gamma \cdot \nabla \gamma = \left[B_0 \left(\alpha, \beta\right)\right]^2 \left(\nabla \alpha \cdot \nabla \alpha\right) \left(\nabla \beta \cdot \nabla \beta\right) - \left(\nabla \alpha \cdot \nabla \beta\right) \left(\nabla \alpha \cdot \nabla \beta\right) \tag{A.19}$$

A logical question arises when working with covariant-contravariant formalism: "Is there a way to go between the two different formalisms?" The answer to this question is yes and it is accomplished through the usage of metric coefficients, g_{ij} and g^{ij}.

We define the metric coefficients as a dot product of the tangent-basis vectors. For the covariant formalism,

$$g_{ij} = \mathbf{e}_i \cdot \mathbf{e}_j \tag{A.20}$$

and the contravariant formalism,

$$g^{ij} = \mathbf{e}^i \cdot \mathbf{e}^j \tag{A.21}$$

From the above, it is implied that the metric coefficients are symmetric (i.e. $g^{ij} = g^{ji}$ and $g_{ij} = g_{ji}$). Furthermore, this allows us to rewrite Equation A.19 in terms of these coefficients,

$$\sigma^2 g^{\gamma\gamma} = g^{\alpha\alpha} g^{\beta\beta} - \left(g^{\alpha\beta}\right)^2 \tag{A.22}$$

If we look at g^{ij} is matrix form, we have,

$$g^{ij} = \begin{pmatrix} g^{\alpha\alpha} & g^{\alpha\beta} & 0 \\ g^{\alpha\beta} & g^{\beta\beta} & 0 \\ 0 & 0 & g^{\gamma\gamma} \end{pmatrix} \tag{A.23}$$

where the elements in $g^{\alpha\gamma}$ and $g^{\beta\gamma}$ are zero, as α and β are both orthogonal to γ. From [D'haeseleer et al., 1991], we have the relationship that,

$$g^{-1} = \det\left(g^{ij}\right) \tag{A.24}$$

Taking the determinant of Equation A.23, we have,

$$\det\left(g^{ij}\right) = g^{\gamma\gamma}\left[g^{\alpha\alpha} g^{\beta\beta} - \left(g^{\alpha\beta}\right)^2\right] \tag{A.25}$$

Plugging Equation A.25 into Equation A.22 and rearranging for σ, we have,

$$\sigma = \frac{B_0\left(\alpha, \beta\right)}{g^{\gamma\gamma}\sqrt{g}} \tag{A.26}$$

We will come back to Equation A.26 in the next section.

A.2 Deriving the Wave Equation

For a cold ($T = 0$) plasma, the wave equations for linear, low frequency waves, assuming ideal MHD conditions, are,

$$\frac{\partial \mathbf{b}}{\partial t} = -\nabla \times \mathbf{E} \tag{A.27}$$

$$\frac{1}{v_A^2}\frac{\partial \mathbf{E}}{\partial t} = (\nabla \times \mathbf{b})_\perp - \frac{(\mu_0 \mathbf{J} \times \mathbf{b}) \times \mathbf{B}}{B^2} \tag{A.28}$$

A.2.1 Faraday's Law

First, we seek to rewrite Faraday's law, Equation A.27, in terms of the field aligned coordinates. In order to do that, we must decompose **E** into basis vectors,

$$\mathbf{E} = E_\alpha \nabla\alpha + E_\beta \nabla\beta \tag{A.29}$$

using Equations A.12, along with $E_\gamma \nabla\gamma = 0$ for MHD waves (Degeling et al. [2010]). If we plug Equation A.29 into A.27 and use the vector identity from [D'haeseleer et al., 1991],

$$\nabla \times (f\mathbf{A}) = f\nabla \times \mathbf{A} + \nabla f \times \mathbf{A} \tag{A.30}$$

then Equation A.27 becomes,

$$\frac{\partial \mathbf{b}}{\partial t} = -\left(\nabla E_\alpha \times \nabla\alpha + \nabla E_\beta \times \nabla\beta\right) \tag{A.31}$$

where the terms involving the curl of a gradient have been omitted, as the curl of a gradient is always zero.

Using the chain rule, we can expand the components of the electric field basis vectors,

$$\nabla E_\alpha = \frac{\partial E_\alpha}{\partial \alpha}\nabla\alpha + \frac{\partial E_\alpha}{\partial \beta}\nabla\beta + \frac{\partial E_\alpha}{\partial \gamma}\nabla\gamma \tag{A.32}$$

$$\nabla E_\beta = \frac{\partial E_\beta}{\partial \alpha}\nabla\alpha + \frac{\partial E_\beta}{\partial \beta}\nabla\beta + \frac{\partial E_\beta}{\partial \gamma}\nabla\gamma \tag{A.33}$$

Inserting Equations A.32 and A.33 into A.31, we get,

$$\frac{\partial \mathbf{b}}{\partial t} = -\left[\left(\frac{\partial E_\beta}{\partial \alpha} - \frac{\partial E_\alpha}{\partial \beta}\right)(\nabla\alpha \times \nabla\beta) + \frac{\partial E_\alpha}{\partial \gamma}(\nabla\gamma \times \nabla\alpha) + \frac{\partial E_\beta}{\partial \gamma}(\nabla\gamma \times \nabla\beta)\right] \tag{A.34}$$

If we use the follow relationship from [D'haeseleer et al., 1991],

$$(\nabla\lambda)^i = \nabla\lambda \cdot \mathbf{e}^i \tag{A.35}$$

we can decompose $\partial\mathbf{b}/\partial t$ into individual components. Looking at the α component of the time derivative of the wave perturbation of the magnetic field,

$$\left(\frac{\partial\mathbf{b}}{\partial t}\right)^{\alpha} = -\frac{\partial E_\beta}{\partial\gamma}\left(\nabla\gamma \times \nabla\beta\right) \cdot \nabla\alpha \tag{A.36}$$

Now, if we use the Equation A.16, we can rewrite $\nabla\gamma$ in terms of $\nabla\alpha$ and $\nabla\beta$,

$$\left(\frac{\partial\mathbf{b}}{\partial t}\right)^{\alpha} = -\frac{\partial E_\beta}{\partial\gamma}\left[\frac{1}{\sigma}\left(\nabla\alpha \times \nabla\beta\right) \times \nabla\beta\right] \cdot \nabla\alpha \tag{A.37}$$

Trudging through the mathematical manipulations, we get,

$$\left(\frac{\partial\mathbf{b}}{\partial t}\right)^{\alpha} = \frac{1}{\sqrt{g}}\frac{\partial E_\beta}{\partial\gamma} \tag{A.38}$$

Of course, there are still the β and γ components to look at, however, the methodology is exactly the same. Thus, for brevity, the final results of the mathematical endeavor will be quoted:

$$\left(\frac{\partial\mathbf{b}}{\partial t}\right)^{\beta} = -\frac{1}{\sqrt{g}}\frac{\partial E_\alpha}{\partial\gamma} \tag{A.39}$$

$$\left(\frac{\partial\mathbf{b}}{\partial t}\right)^{\gamma} = -\frac{1}{\sqrt{g}}\left(\frac{\partial E_\beta}{\partial\alpha} - \frac{\partial E_\alpha}{\partial\beta}\right) \tag{A.40}$$

A.2.2 Equation A.28

Just like for Faraday's law, when we broke down the wave electric field into its components, we must do the same for the perturbation in the magnetic field,

$$\mathbf{b} = b_\alpha\nabla\alpha + b_\beta\nabla\beta + b_\gamma\nabla\gamma \tag{A.41}$$

If we take the curl of Equation A.41 and only consider the perpedicular component, then apply Equation A.30, we have,

$$\left(\nabla \times \mathbf{b}\right)_\perp = \left(\nabla b_\alpha \times \nabla\alpha + \nabla b_\beta \times \nabla\beta + \nabla b_\gamma \times \nabla\gamma\right)_\perp \tag{A.42}$$

Now, just as we did with Faraday's law, we must find the components of the perpendicular component of the curl of the wave magnetic field. Again, the procedure for doing this is just like what was done for Faraday's law, so for brevity, we will just list the components without the full derivation:

$$(\nabla \times \mathbf{b})^{\alpha}_{\perp} = -\frac{1}{\sqrt{g}}\left(\frac{\partial b_{\beta}}{\partial \gamma} - \frac{\partial b_{\gamma}}{\partial \beta}\right) \tag{A.43}$$

$$(\nabla \times \mathbf{b})^{\beta}_{\perp} = \frac{1}{\sqrt{g}}\left(\frac{\partial b_{\alpha}}{\partial \gamma} - \frac{\partial b_{\gamma}}{\partial \alpha}\right) \tag{A.44}$$

Now, if we define another variable, $\mathbf{Z}$, such that,

$$\mathbf{Z} = \mu_0 \frac{(\mathbf{J} \times \mathbf{b}) \times \mathbf{B}}{B^2} = -\frac{\mu_0}{B^2}(\mathbf{B} \cdot \mathbf{b})\,\mathbf{J} \tag{A.45}$$

and using the following definitions,

$$\mathbf{B} \cdot \mathbf{b} = \sigma \nabla\gamma \cdot \mathbf{b} \tag{A.46}$$

$$B^2 = \sigma^2 \nabla\gamma \cdot \nabla\gamma = \sigma^2 g^{\gamma\gamma} \tag{A.47}$$

this allows us to rewrite Equation A.45 as,

$$\mathbf{Z} = -\frac{\mu_0 b^{\gamma} \mathbf{J}}{\sigma g^{\gamma\gamma}} \tag{A.48}$$

Another relationship we can invoke from [D'haeseleer et al., 1991] is related to the metric coefficients,

$$g_{ij} g^{jk} = \delta^k_i \tag{A.49}$$

which allows us to write $(g^{\gamma\gamma})^{-1}$ as $g_{\gamma\gamma}$. The metric coefficient $g_{\gamma\gamma}$ acts as a lowering operator on b^{γ}, such that Equation A.48 can be written as,

$$\mathbf{Z} = -\frac{\mu_0 b_{\gamma} \mathbf{J}}{\sigma} \tag{A.50}$$

Now, we can use Ampère's law to write,

$$\mu_0 \mathbf{J} = \nabla \times \mathbf{B} = \nabla \times (\sigma \nabla\gamma) \tag{A.51}$$

which can be written as,

$$\mu_0 \mathbf{J} = \nabla\sigma \times \nabla\gamma \tag{A.52}$$

Now, using the chain rule, we can write,

$$\nabla\sigma = \frac{\partial\sigma}{\partial\alpha}\nabla\alpha + \frac{\partial\sigma}{\partial\beta}\nabla\beta + \frac{\partial\sigma}{\partial\gamma}\nabla\gamma \tag{A.53}$$

If we follow the same methodology as the previous derivations, we can find the perpendicular components of $\mu_0\mathbf{J}$ in the exact same fashion. For brevity, the results are,

$$(\mu_0\mathbf{J})^{\alpha} = \frac{1}{\sqrt{g}}\frac{\partial\sigma}{\partial\beta} \tag{A.54}$$

$$(\mu_0\mathbf{J})^{\beta} = -\frac{1}{\sqrt{g}}\frac{\partial\sigma}{\partial\alpha} \tag{A.55}$$

Given Equations A.54 and A.55, we can rewrite Equation A.50 in terms of its components,

$$\mathbf{Z}^{\alpha} = -\frac{b_\gamma}{\sigma\sqrt{g}}\frac{\partial\sigma}{\partial\beta} \tag{A.56}$$

$$\mathbf{Z}^{\beta} = \frac{b_\gamma}{\sigma\sqrt{g}}\frac{\partial\sigma}{\partial\alpha} \tag{A.57}$$

The fruits of our labour allow us to write Equation A.28 in component form,

$$\frac{1}{v_A^2}\left(\frac{\partial\mathbf{E}}{\partial t}\right)^{\alpha} = \frac{1}{\sqrt{g}}\left[-\frac{\partial b_\beta}{\partial\gamma} + \frac{1}{\sigma}\frac{\partial}{\partial\beta}\left(\sigma b_\gamma\right)\right] \tag{A.58}$$

$$\frac{1}{v_A^2}\left(\frac{\partial\mathbf{E}}{\partial t}\right)^{\beta} = \frac{1}{\sqrt{g}}\left[\frac{\partial b_\alpha}{\partial\gamma} - \frac{1}{\sigma}\frac{\partial}{\partial\alpha}\left(\sigma b_\gamma\right)\right] \tag{A.59}$$

From [D'haeseleer et al., 1991], we have the following relationship,

$$(\nabla\lambda)^i = \frac{\partial\lambda}{\partial u^j}\nabla u^j \cdot \nabla u^i \tag{A.60}$$

This allows us to rewrite the components of the wave electric and magnetic field derivatives:

$$\left(\frac{\partial\mathbf{E}}{\partial t}\right)^{\alpha} = g^{\alpha\alpha}\frac{\partial E_\alpha}{\partial t} + g^{\alpha\beta}\frac{\partial E_\beta}{\partial t} = \frac{v_A^2}{\sqrt{g}}\left[-\frac{\partial b_\beta}{\partial\gamma} + \frac{1}{\sigma}\frac{\partial}{\partial\beta}\left(\sigma b_\gamma\right)\right] \tag{A.61}$$

$$\left(\frac{\partial\mathbf{E}}{\partial t}\right)^{\beta} = g^{\alpha\beta}\frac{\partial E_\alpha}{\partial t} + g^{\beta\beta}\frac{\partial E_\beta}{\partial t} = \frac{v_A^2}{\sqrt{g}}\left[\frac{\partial b_\alpha}{\partial\gamma} - \frac{1}{\sigma}\frac{\partial}{\partial\alpha}\left(\sigma b_\gamma\right)\right] \tag{A.62}$$

$$\left(\frac{\partial\mathbf{b}}{\partial t}\right)^{\alpha} = g^{\alpha\alpha}\frac{\partial b_\alpha}{\partial t} + g^{\alpha\beta}\frac{\partial b_\beta}{\partial t} = \frac{1}{\sqrt{g}}\frac{\partial E_\beta}{\partial\gamma} \tag{A.63}$$

$$\left(\frac{\partial \mathbf{b}}{\partial t}\right)^{\beta} = g^{\alpha\beta}\frac{\partial b_\alpha}{\partial t} + g^{\beta\beta}\frac{\partial b_\beta}{\partial t} = -\frac{1}{\sqrt{g}}\frac{\partial E_\alpha}{\partial \gamma} \tag{A.64}$$

$$\left(\frac{\partial \mathbf{b}}{\partial t}\right)^{\gamma} = g^{\gamma\gamma}\frac{\partial b_\gamma}{\partial t} = -\frac{1}{\sqrt{g}}\left(\frac{\partial E_\beta}{\partial \alpha} - \frac{\partial E_\alpha}{\partial \beta}\right) \tag{A.65}$$

Now, we can write Equations A.61 and A.62 in matrix form,

$$\frac{1}{\sqrt{g}}\frac{\partial}{\partial \gamma}\begin{pmatrix} E_\alpha \\ E_\beta \end{pmatrix} = \begin{pmatrix} g^{\beta\beta} & -g^{\alpha\beta} \\ -g^{\alpha\beta} & g^{\alpha\alpha} \end{pmatrix}\begin{pmatrix} -\partial b_\beta/\partial t \\ \partial b_\alpha/\partial t \end{pmatrix} \tag{A.66}$$

If we define the matrix $\mathbf{G}$, such that,

$$\mathbf{G} = \begin{pmatrix} g^{\alpha\alpha} & g^{\alpha\beta} \\ g^{\beta\alpha} & g^{\beta\beta} \end{pmatrix} \tag{A.67}$$

its inverse can be used in Equation A.66, such that it can be written as,

$$\frac{1}{\sqrt{g}}\frac{\partial}{\partial \gamma}\begin{pmatrix} E_\alpha \\ E_\beta \end{pmatrix} = \frac{1}{g g^{\gamma\gamma}}\mathbf{G}^{-1}\begin{pmatrix} -\partial b_\beta/\partial t \\ \partial b_\alpha/\partial t \end{pmatrix} \tag{A.68}$$

After some rearranging and multiplying both sides of Equation A.68 by $\partial/\partial\gamma$, and using the definition of σ from Equation A.26, we get,

$$\frac{\partial}{\partial \gamma}\left[\frac{B_0\,(\alpha,\beta)}{\sigma}\mathbf{G}\frac{\partial}{\partial \gamma}\begin{pmatrix} E_\alpha \\ E_\beta \end{pmatrix}\right] = \begin{pmatrix} -\frac{\partial}{\partial\gamma}\frac{\partial b_\beta}{\partial t} \\ \frac{\partial}{\partial\gamma}\frac{\partial b_\alpha}{\partial t} \end{pmatrix} \tag{A.69}$$

Now, through clever manipulation of Equations A.66 and A.69, we can write,

$$\begin{pmatrix} -\frac{\partial}{\partial\gamma}\frac{\partial b_\beta}{\partial t} \\ \frac{\partial}{\partial\gamma}\frac{\partial b_\alpha}{\partial t} \end{pmatrix} = \frac{1}{\sigma}\begin{pmatrix} -\frac{\partial}{\partial\beta} \\ \frac{\partial}{\partial\alpha} \end{pmatrix}\left(\sigma\frac{\partial b_\gamma}{\partial t}\right) + \frac{\sqrt{g}}{v_A^2}\mathbf{G}\begin{pmatrix} \frac{\partial^2 E_\alpha}{\partial t^2} \\ \frac{\partial^2 E_\beta}{\partial t^2} \end{pmatrix} \tag{A.70}$$

Combining Equations A.69 and A.70, we get,

$$\frac{\partial}{\partial \gamma}\left[\frac{B_0\,(\alpha,\beta)}{\sigma}\mathbf{G}\frac{\partial}{\partial \gamma}\begin{pmatrix} E_\alpha \\ E_\beta \end{pmatrix}\right] - \frac{\sqrt{g}}{v_A^2}\mathbf{G}\frac{\partial^2}{\partial t^2}\begin{pmatrix} E_\alpha \\ E_\beta \end{pmatrix} = \frac{1}{\sigma}\begin{pmatrix} -\frac{\partial}{\partial\beta} \\ \frac{\partial}{\partial\alpha} \end{pmatrix}\left(\sigma\frac{\partial b_\gamma}{\partial t}\right) \tag{A.71}$$

Equation A.71 is the general equation that governs the ULF wave model. The left-hand side of Equation A.71 represents the shear Alfvén mode, while the right-hand side represents the compressional mode. If one is only considering field lines oscillating independently (i.e. no field line coupling), the right-hand side of Equation A.71 becomes zero.